Hierarchical Assembly of Polymeric Nanofibers for Advanced Material Applications

Ji Wang

Dissertation submitted to the faculty of the Virginia Polytechnic Institute and State University in partial fulfillment of the requirements for the degree of

Doctor of Philosophy

In

Engineering Mechanics

Amrinder S. Nain, Chair

Raffaella De Vita

Rakesh K. Kapania

Robert B. Moore

Judy S. Riffle

February 27th, 2015

Blacksburg, Virginia

Keywords: STEP, isodiametric design space, porous tubes, single nanofiber mechanical properties, hierarchical nanofiber assemblies, cell force measurement

Hierarchical Assembly of Polymeric Nanofibers for Advanced Material Applications

Ji Wang

Abstract

Polymer nanofibers are gaining importance due to their wide applicability in diverse fields, such as tissue engineering, fuel cells, photonics and sensors. For these applications, manufacturing aligned polymer nanofibers with precisely controlled morphology and well characterized mechanical properties in a bottom up configuration is essential. In this work, we developed an isodiametric design space for fabrication of aligned polystyrene nanofibers (diameter 60-800nm) using non-electrospinning Spinneret based Tunable Engineered Parameter (STEP) technique. By adjusting the processing parameters such as relative humidity, solvent volatility and polarity, porous polymer tubes are demonstrated having large specific surface areas. Combining STEP with sol-gel process, aligned inorganic nanofibers, such as Titanium Oxide (TiO_2) with varied morphologies can be conveniently obtained. Mechanical properties of aligned polymer nanofibers (diameter from 50nm to several hundred nanometers) with fixed-fixed boundary conditions were estimated using a lateral force microscope (LFM). We find that the tension in the fiber caused during fabrication process scales with fiber diameter and it dominates fiber stiffness. Our studies demonstrate isotropic arrangement of polymer chains in the fibers and anisotropic arrangement in the necking region for fibers undergone deformation. Finally, this study demonstrates development of force sensors capable of measuring single cell forces, which scale with the fiber structural stiffness. The ability to measure cell forces during cell division, migration and apoptosis provides new insights in cell mechanobiology.

Acknowledgement

I’d like to express my gratitude to the people that made this work possible and provided guidance over my time at Virginia Tech. My advisor, Professor Amrinder Nain for welcoming me as the first student into his team, providing guidance and encouragement throughout the whole process, and for allowing the freedom to explore interesting topics as they came up, regardless of the outcome. Additionally, I’d like to thank the rest of my committee, Professor Raffaella De Vita, Professor Robert B. Moore, Professor Rakesh K. Kapania and Professor Judy S. Riffle for their guidance and encouragement both in class and in the context of my research. I’d like to thank Virginia tech and the Engineering Science and Mechanics Department for providing funding and support, and ICTAS and the NCFL as well for facilities and equipment. I would also like to thank other members in the STEP lab for their suggestions and collaboration, my work would not have been possible without the support of Kevin Sheets, Puja Sharma, Colin Ng, Brian Koons , Amritpal Gil and the rest of the STEP lab. Additionally, I’d like to thank Dr. Behkam for her sincere and generous help. I wish all of you good luck in your work in the future, wherever it leads you. I would like to acknowledge the Engineering Mechanics Department and Macromolecules and Interfaces Institute in Virginia Tech for the financial support during the study.

Attribution

Several colleagues added in this research. A brief description of their contributions is included here.

Chapter 2 Isodiametric Design Space for Depositing Aligned Polymeric Nanofibers

Part work of **Chapter 2** was published in Polymer Journal, 2013.

Dr Amrinder S.Nain is currently a professor at mechanical engineering department of Virginia Tech. He is a co-author of this paper and contributed editorial comments.

Chapter 3 Aligned Polystyrene Tubes with Controlled Morphologies

Chapter 3 was published in Polymer, 2014

Junbo Hou Ph.D is currently a researcher at SAFCELL. Dr Junbo Hou was a co-author on this paper and conducted Brunauere Emmette Teller (BET) experiments.

Eduardo Marquez is currently a graduate student at Virginia Tech. Eduardo Marquez was a co-author on this paper and helped with sample preparation and data analysis for pore formation on fibers.

Dr Robert B.Moore is currently a professor at chemistry department of Virginia Tech. He is a co-author of this paper and contributed editorial comments.

Dr Amrinder S.Nain is currently a professor at mechanical engineering department of Virginia Tech, he is a co-author of this paper and contributed editorial comments.

Chapter 5 Biological Applications of Hierarchical Nanofiber Assemblies

Part work of Chapter 5 was published in Langmuir, 2015.

Kevin Sheets Ph.D is currently a post-doctoral associate at University of North Carolina. Dr Sheets did the cell culture and staining.

Ms. Puja Sharma is currently a Ph.D candidate at Virginia Tech. Ms. Sharma did the cell culture and staining work.

Chapter 6 Organized Long Titanium Dioxide Nanofibers/Nanotubes

Chapter 6 was published in New Journal of Chemistry, 2013.

Junbo Hou Ph.D is currently a researcher at SAFCELL. Dr Junbo Hou was a co-author on this paper and helped with precursor fiber calcination process.

Dr Michael W. Ellis is currently a professor at mechanical engineering department of Virginia Tech. He is a co-author of this paper and contributed editorial comments.

Dr Amrinder S.Nain is currently a professor at mechanical engineering department of Virginia Tech. He is a co-author of this paper and contributed editorial comments.

Table of Contents

List of Figures

List of Tables

List of Abbreviations

STEP	Spinneret based Tunable Engineered Parameter
ECM	Extracellular matrix
MSC	Mesenchymal Stem Cell
nm	Nano meter
nN	Nano Newton
μm	Micro meter
mm	Millimeter
AFM	Atomic Force Microscope
PS	Polystyrene
PMMA	Poly methyl methacrylate
PU	Poly Urethane
DC	Direct Current
RPS	Rotation Per Second
ml	Milliliter
μl	Microliter
μg	Microgram
SEM	Scanning Electron Microscope
TEM	Transmitting Electron Microscope

Chapter 1 : Introduction

Nanofibers are one of the most intriguing 1D building blocks playing a pivotal role in nanotechnology. Their unique mechanical and electronic properties coupled with the ability to functionalize large available surface area promises to revolutionize new devices, circuits, man-made materials and sensors. These applications require manufacturing of three dimensional nanofiber assemblies with precise control on individual fiber dimension and spatial deposition. Current state-of-the-art efforts in building these structures are hampered by the spinnability of these fibers at the nanoscale, which often result in production of discontinuous fibers or fibers with a mix of diameters spun at irregular spacing and orientation. Here using the non-electrospinning Spinneret based Tunable Engineered Parameters (STEP) fiber manufacturing platform,[1–3] we demonstrate the feasibility of depositing nano-micron scale polymeric fibers with precise control on diameter, spacing and orientation in single and multiple layers on planar and 2D curved surfaces for a wide range of applications in physical and biological domains.

1.1 Motivation

A platform for fabricating and depositing polymeric nanofibers with high degree of alignment and precise configuration control on planar and curved substrates may offer new opportunities to improve existing technologies or develop new ones as outlined below.

1.1.1 Bio-Scaffolds for Tissue Engineering

One aspect of tissue engineering has been the design of polymeric scaffolds with specific mechanical and biological properties similar to native extracellular matrix (ECM) in order to modulate cellular behaviors, such as migration, proliferation, differentiation, gene expression and secretion of various hormones and growth factors.[4,5] Polymer nanofiber networks are ideal for tissue engineering scaffolds because the high surface area allows for a high percentage of cellular

attachment, as well as multiple focal adhesion points on different fibers due to nano-sized fiber diameters. Additionally, fibers in the nanometer range more closely resemble the size of extracellular components such as collagen and fibrinogen.

Today, bio-scaffolds made of electrospun aligned polymer nanofibers are finding applications in diverse fields of tissue engineering. Ramakrishna *et al.* collected aligned polymer nanofibers on a rotating drum collector for vascular tissue engineering and they found that human coronary artery muscle cells express a spindle-like shape and the cytoskeleton inside these cells was parallel to the direction of the nanofibers.[6,7] Prabhakaran *et al* seeded cardiomyocytes onto aligned electrospun (poly L-lactic acid) PLLA nanofibers and the cells exhibited fiber guided filipodia-like protrusions and developed into sarcomeres.[8] Yang *et al* seeded neural stem cells (NSCs) on aligned PLLA nanofiber scaffolds and they found that the direction of NSC elongation and outgrowth is parallel to the fibers and the NSC differentiation was higher on PLLA nanofibers than that on micro fibers.[9] Yin *et al* found that human tendon stem/progenitor cells (hTSPCs) seeded on aligned PLLA nanofibers have significantly higher tendon-specific genes expression than those on randomly-oriented nanofibers in both normal and osteogenic media.[10] *In vivo* experiments showed that aligned nanofibers induced formation of spindle-shaped cells and tendon like tissue. Lee *et al* found that human ligament fibroblasts (HLF) on the aligned nanofibers were spindle-shaped and synthesized significantly more collagen than those on random nanofiber sheets.[11] Li *et al* fabricated radially aligned poly (-caprolactone) PCL nanofibers which induce faster migration and population of fibroblast cells than nonwoven mats consisting of random nanofibers.[12] Their results indicate that the scaffolds based on radially aligned electrospun nanofibers may be useful as biomedical patches or grafts to induce wound closure.

Using non-electrospinning STEP manufacturing platform, Nain *et al*. demonstrated that cells on aligned and suspended fibers exhibited higher migration speeds and changes in migration direction [13]. Furthermore, using arrays of aligned parallel and cross hatch patterns of fibers, neural stem cells were demonstrated to predominantly differentiate into neurons (~80%) and cells up to 4 mm away from those on fibers also predominantly became neurons [14] Subsequently in another differentiation study, coupled with ink-jetting of growth factors on suspended nanofibers, the authors demonstrated spatial control on achieving muscle, tendon and bone lineages. Recently, work by Sheets et al, has demonstrated that cells on suspended fibers have focal adhesion cluster length ~4X longer than those on flat substrates, which may be the reason why cells have different behaviors associated with fiber dimensionality.[15] In the context of disease models, Sharma et al, has demonstrated that the bleb size and number density of blebs on a cell inversely correlates with the area, with blebs on glioma cells eliminated at a cell spread area of ~1600 μm^2. [16]

Thus, it is no surprise that cell-fiber interfaces constitute an increasingly studied new class of biological assays with widespread applications in development biology and disease models. A subset of these biological assays (presented in this work) constitutes the aligned and suspended hierarchical assemblies of fiber networks, which provide the cells with simultaneous 1D (alignment), 2D (spread cell area) and 3D (cell curvature interactions) interfaces within the same scaffold. [17–19]

1.1.2 Surface modification

Nanofiber mats usually have high surface roughness and therefore provide an ideal candidate for construction of hydrophobic surfaces on a large scale. Compared to most other superhydrophobic coatings, nanofiber fabrics have their own advantages, such as being breathable, flexible, and self-supporting.

So far, highly stable superhydrophobic nanofiber fabrics from a variety of materials have been achieved. Ma *et al* achieved nanofibers mats from poly(styrene-blockdimethylsiloxane) block copolymer blended with homopolymer polystyrene (PS), which yielded a contact angle of 163°. [20] Jiang *et al* reported a contact angle of 160.4 ° for a membrane consisting of micrometer-sized PS particles embedded within a fibrous PS matrix. [21] Acatay *et al* reported comparable contact angles for a membrane made of a perfluorinated linear diol and beads mixed with poly(acrylonitrile-co-a,a-dimethyl m-isopropenylbenzyl isocyanate) fibers. [22] Ma *et al* also found that beads-on-string morphology resulted in improved superhydrophobicity compared to the bead-free fibers, with contact angles as high as 175°. They further developed hierarchically structured nanofibers with surface decorated with nanometer scale pores or particles, which leads to higher contact angles and lower hysteresis values compared to smooth nanofiber mats. [23,24]

Recently, aligned polymer nanofibers have been used to construct biomimetic surfaces with controlled wettability. The topography and wetting properties of biosurfaces such as lotus leaves, bamboo leaves, goose feathers and water strider's legs were mimicked with different patterns of polymer nanofibers. Wu *et al* achieved surfaces with anisotropic wetting in three directions based on aligned polymer nanofibers. [25] Lin *et al* developed super-hydrophobic surface made of aligned polyacrylonitrile (PAN) nanofibers, which has a water contact angle of 173.8 ° without any modification. [26] The density of aligned PAN nanofibers is believed to play an important role in determining the hydrophobicity. Lee et al fabricated nanostructured polymeric surfaces with aligned PS nanofibers, which show remarkable structural similarity with cicada wings. [27] By controlling the aspect ratios of the aligned PS nanofibers, a contact angle of 155.8° has been

achieved. In a similar fashion, using STEP fiber assemblies, Mehdi *et al* studied the effect of topographical feature size, spacing and local curvature on the adhesion of bacteria, and concluded that texturizing the surface with appropriately designed nanofiber patterns is able to reduce bacteria adhesion. [28]

1.1.3 Textile Industry

Randomly orientated nanofibers in the typically electrospun non-woven mats is widely used in applications of filters and wound dressing. However, nanofibers need to be collected as continuous uniaxial fiber bundles or yarns to make their commercialization in the fiber and textile industry viable.

Various approaches have been taken to obtain nanofiber bundles/yarns. Fennessey et al twisted unidirectional tows of electrospun nanofibers into yarns using an electric twister, which allowed tensile testing of the nanofibers.[29] Wang *et al* obtained continuous polymer nanofiber yarns by inducing self-bundling of electrospun nanofiber using a grounded tip. Self-bundling yarns made from poly(3-hydroxybutyrate-co-3-hydroxyvalerate) (PHBV), polyacrylonitrile (PAN), poly(L-lactic acid) (PLLA) and poly(m-phenyleneisophthalamide) (PMIA), were prepared successfully using this approach. [30]Li et al prepared continuous nanofiber yarns of PLLA/ nano-b-tricalcium phosphate (n-TCP) composite by conjugate electrospinning with coupled spinnerets.[31] Ko *et al* manufactured continuous (single wall nanotube) SWNT reinforced PAN nanofiber yarns through co-electrospinning process. SWNT contribute to thermal stability and provide a significant reinforcement effect at less than 3 % volume.[32] Teo *et al* reported an approach to assemble electrospun fibers into a continuous yarn using a water vortex. Both the feeding rate and the polymer solution concentration were found to affect the yarn morphology. [33]

1.2 A Brief Survey of Existing Continuous Polymer Nanofiber Fabrication Techniques

Continuous polymer nanofibers have been a subject of intensive research due to their unique properties and intriguing applications in many fields. The three major hurdles for controlling the quality and scope of the applications include achieving precise control on alignment and morphology as well as mechanical characterization of polymer nanofibers. In the following section, we present a brief overview of the current state-of-the-art techniques in nanofiber alignment and morphology control and mechanical characterization .

1.2.1 Nanofiber Alignment Control

One of the key factors impacting applications of continuous micro/nanofibers is the ability to precisely control fiber deposition (both orientation and spacing) in single and multiple layers. The recent advancements in achieving control on fiber deposition include electrospinng (far-field electrospinning (FFES), near-field electrospinning (NFES)) and direct drawing.

FFES is widely used to fabricate continuous micro/nanofibers from various materials (including engineering plastics, biopolymers and ceramics). Based on FFES, various electrospinning set-ups have been developed to achieve aligned nanofiber assemblies. Dynamic mechanical devices such as rotating drums, disks or mandrels are used to collect electrospun nanofibers into aligned assemblies. Katta *et al* demonstrated aligned as-spun nanofibers on a high speed rotating drum.[34] Matthew et al demonstrated the effect of the drum's rotating speed on the degree of electrospun collagen fiber alignment. [35] Kessick *et al* used an alternating-current (AC) high voltage supply instead of typical direct-current (DC) supply for electrospinning and found that polyethylene oxide (PEO) collected on a rotating mandrel showed a greater degree of alignment using an AC potential than a DC potential.[36] Some researchers also achieved aligned electrospun nanofibers by

manipulating the electric field. Li *et al* demonstrated that two electrodes placed in parallel were able to collect aligned fibers in the gap. [37] Using a similar concept, some complex patterns of electrospun nanofibers were obtained by arranging an array of counter-electrodes.[38] Similarly, Teo *et al* collected aligned nanofibers by placing two blades in line with one another with a gap between them.[39] Dalton *et al* used two rings placed in parallel to collect highly aligned fibers deposited at the perimeters of the rings. [40] In all these approaches, due to the inherent electric instabilities, a high degree of parallelism among micro/nanofibers was difficult to achieve, which may be the result of residual charge accumulation on the deposited fibers that interferes with the alignment of incoming fibers.

NFES has demonstrated improved fiber patterning through reduction of applied voltage and the source-to-target distance. Bisht *et al* deposited aligned polymeric nanofibers on two-dimensional and three dimensional substrates using low voltage (200V) near-field electrospinning.[41] The bending instabilities are reduced, resulting in better control of the polymer solution jet. Sun *et al* demonstrated orderly collected nanofibers by using a 600 V voltage and a tungsten electrode with tip diameter of 25 μm. [42] However, precise multilayer fiber patterning on large surfaces using NFES has yet to be demonstrated.

As an alternative approach, direct drawing uses polymer wetted probe tips for precise micro/nanofibers deposition. Harfenist et al demonstrated the capability of polymer solutions to be quickly drawn and interconnected into custom three-dimensional networks using various nanomanipulating instruments. [43] In parallel, Nain *et al* used proximal probes (AFM cantilevers and glass micropipettes) to draw polymer fibers down to a few hundred nanofibers in diameter and

several hundred micrometers in length.[44,45] Although some well positioned fibers have been demonstrated, this technique cannot operate continuously as (a) it is difficult to precisely deposit sub 250nm diameter fibers due to limitations of optical resolution, and (b) the short time constants available for continuous fabrication due to evaporation of the solvent.

1.2.2 Nanofiber Morphology Control

Creating a hierarchical surface roughness by decorating nanofibers with nanometer scale pores has recently initiated great interest among researchers. By using a highly volatile solvent during electrospinning, porous fibers have been obtained from a wide variety of polymer species, such as polystyrene (PS), polycarbonate (PC), poly (methylmethacrylate) (PMMA), poly-L-lactide (PLLA) and polyoxymethylene (POM).[46–50] The mechanism of pore formation was attributed to a combination of thermal and vapor induced phase separation.

Micro/nano tubes are increasingly finding potential for applications in a wide range of emerging fields: fluid storage for fuel cells, catalysts, drug release and photonics. [51–53] This is due to their high specific interface area, which strongly enhances the reactivity, absorption rate as well as the efficiency of transport within and across tube walls. To prepare tube structures, three approaches are commonly employed: self-assembly, tubes by fiberfiber templates (TUFT) and co-electrospinning. Self-assembly strategies include assembly of rod-like sub-units into barrel shaped frameworks. [54] Linear sub-units, such as natural antibiotic gramicidin A, can form tubular structures by coiling into helical conformations. [55] TUFT uses polymer nanofibers as templates which are then coated with precursor materials. Tube structures are obtained by selective dissolution or thermal degradation of the polymer nanofibers. [56,57] Compared with the other two approaches, co-electrospinning is more commonly used due to its simplicity and versatility. During a co-electrospinning process, two immiscible solutions are simultaneously spun into

core/shell fiberfibers from a spinneret containing coaxial capillaries. Tube structures are then typically obtained by selectively removing the core. [58–60] To date, tubular structures made from peptides, polymers, and ceramics have been obtained. However, precise control in fiber morphology, deposition alignment and assembly still need to be demonstrated.

1.2.3 Mechanical characterization of polymer nanofibers

Due to the reduced fiber diameter and the volume, the defects contained in nanofibers is significantly reduced compared to the bulk material. In addition, polymer chains may be aligned along the fiber axis during the nanofiber manufacturing process. As a result, polymer nanofibers possess superior mechanical properties compared to bulk materials. However, mechanical characterization of single polymer nanofibers is difficult due to the tiny load (nano Newton level) needed to break a polymer nanofiber. In addition, manipulation of single polymer nanofibers is challenging due to their fragile natures. In the past decade, various approaches have been developed by using an AFM cantilever as the force sensor. Tan *et al* conducted a three point bending test on suspended single PLLA nanofibers and measured their Young's modulus. [61] With the same method, Sung et al characterized the elastic modulus of TiO2 nanofiber. [62] In parallel, Li *et al* have demonstrated that elastic modulus can be obtained by indenting a nanofiber using an AFM cantilever tip. Although three point bending and nanoindentation provides straightforward approaches to investigate the modulus of single polymer nanofibers, there are some problems remained to be addressed. For example, the slippage between the cantilever tip and the nanofiber leads to erroneous results and it is difficult to locate the cantilever tip on nanofibers with diameter less than 250 nm. In addition, due to the absence of boundary conditions, it is difficult to obtain the fiber break strength using three point bending of nanoindentation. Recently, Yu *et al* reported a tensile test of multiwall carbon nanotubes by attaching one end of the nanotubes to the cantilever and the other end to an epoxy droplet. [63] However, it is time consuming to

prepare samples and the process needs to be conducted within SEM, where the electron beams may damage polymer nanofibers. Development of integrated Approach provide the platform for single fiber mechanical characterization on TEM grids with fixed-fixed boundary conditions. Using this approach, mechanical characterization of fibers spanning a wide diameter range (30-800nm) was performed. [64]

1.3 Focus of the Work

This research aims to establish a robust nanofiber fabrication platform for physical and biological applications, which provides unique control on polymer nanofiber i) alignment, ii) spacing, iii) diameter (sub 100nm to μm) iv) morphology and v) deposition in multi-layer assemblies. The proposed research includes:

1. Develop isodiametric design space for polymer nanofibers thorough investigations of polymer solution rheology. The effect of polymer solution concentrations and molecular weights on nanofiber diameters will be systematically investigated as fiber spinnability design space using STEP process was previously demonstrated to span semi-dilute entangled concentrations. Using STEP, polymer nanofibers with uniform diameter ranging from *sub 100nm* to *microns* and lengths of at least several millimeters will be deposited in arrays with control on adjacent fiber spacing.

2. Control both the surface and interior morphology of nanofibers through manipulating relative humidity and solvent types. We will introduce nanopores on the nanofiber surface by increasing both solvent polarity and relative humidity. Meanwhile, we want to achieve hollow/ porous fiber cross-sections by controlling the polymer solution solidification process. The nanofibers with porous morphologies would have large surface area, which allows these to be used as absorbents.

3. The mechanical properties of polymer nanofibers may be different from the bulk materials. It is necessary to establish a platform to mechanically characterize single polymer nanofibers. Using an *Integrated Approach*, nanofibers with solid boundary conditions will be deposited on TEM finder grids. An AFM cantilever will then be used to deflect the fiber at different strain rates and measure the forces associated with nanofiber deformation, which will allow determining the material constants of nanofibers. Specifically we will determine the tension, modulus, tensile stress and polymer chain orientation for different molecular weights of polystyrene subjected to deformations at different strain rates.

4. For real life applications, aligned nanofibers will be used as one dimensional building blocks to construct bottom up three dimensional hierarchical assemblies, which will be used as bio-scaffolds. The effect of fiber orientation and spacing on cell attachment and spreading areas will be evaluated. Further, a nanofiber assembly based cell force measurement platform will be developed, which allows probing cell forces in an environment similar to *in vivo* extra cellular matrix. Cell forces associated with cell division, migration and apoptosis process can be measured through the deflections of nanofibers.

5. To further demonstrate the applications of nanofibers, STEP process will be combined with sol-gel process to produce inorganic nanofibers, such as TiO_2 nanofibers. The photocatalytic activity of TiO_2 nanofibers is directly related to their specific surface area (SSA) and different sol-gel routes will be developed to control TiO_2 nanofiber morphologies.

Chapter 2 Isodiametric Nanofiber Design Space for Depositing Aligned Polymeric Nanofibers

Amrinder Nain, Ji Wang, Polymer Journal, 2013, 45, 695-700. Used with permission of Nature Publishing group, 2015.

2.1 Introduction

Polymeric micro/nanofibers are increasingly gaining importance due to their versatile applications in diverse fields, such as tissue engineering, smart textiles, sensors and actuators. Traditionally, well established techniques of spun bounding, melt blowing dry spinning, conjugate spinning and CO_2 laser thinning produce polymeric fibers having diameters in the micron scales with lengths in excess of meters. [65–69] However, aligned deposition and continuous production of long fibers with nanoscale diameters has been challenging due to the fragility of polymeric materials. Additionally, numerous applications require deposition of smooth, uniform and defect-free nanofiber arrays in aligned configurations with user-defined geometrical spacing. Several processes have been developed to fabricate polymer nanofiber arrays, including electrospinning, template synthesis, phase separation and sequential micro dry spinning. Of all these methods, perhaps electrospinning is the most popular process, which allows the continuous production of fibers ranging from tens of nanometers to a few microns in diameter, and requires specialized strategies for aligned deposition of these fibers. Although nanofibers can be more or less aligned in single and multiple layers, tight control on fiber diameter and spacing has yet to be realized. The deficiencies of current state-of-art fabrication methods continue to hinder improvements in applications of polymer nanofibers.

In this study, aligned polymer nanofibers were achieved using Spinneret based Tunable Engineering Parameter technique (STEP). STEP technique is a non-electrospinning strategy,

which enables deposition of arrays of polymer fibers having uniform diameters ranging from sub 100nm to microns and lengths of at least several millimeters along with the ability to control adjacent fiber-fiber spacing.

2.2 Experimental Section

Solution preparation: All chemicals were used as received without further purification. Polystyrene (PS) of several molecular weights (M_w) (650K, 860K, 1500K, and 2000K g.mol-1, Scientific Polymer Products Inc., New York, USA) were dissolved at room temperature in p-xylene with varying wt% concentrations (from 1 wt% to 18 wt%) for one week prior to experiments. Poly(methyl methacrylate) (PMMA, M_w =540K g.mol-1, Scientific Polymer Products Inc., New York, USA) dissolved in chlorobenzene at 14 wt% and poly(lactic-co-glycolic acid) (PLGA, Purac Biochem Inc., Holland) dissolved in chloroform at 3 wt% were used in this study. Bovine plasma fibrinogen (Sigma-Aldrich Chemical Inc., USA) was dissolved in a solution composed of 9 parts 1,1,1,3,3,3-hexafluoro-2-propanol (HFP) and 1 part 10×minimal essential medium (MEM) at 20 wt% for one week prior to experiments. Polyurethane (PU5719, Lubrizol Advanced Material Inc., USA) was dissolved in dimethylformamide (DMF) at 30 wt% and heated to 80°C with stirring for 24 hours to prepare a homogenous solution. One gram of titanium isopropoxide (Ti(OiPr)4, Sigma-Aldrich Chemical Inc., USA) was mixed with 2.7 g of a 7 wt% PS (M_w=2000K)-p-xylene solution, followed by magnetic stirring for 1 hour before experiments

STEP spinning: The spinning process was performed at a temperature of 20°C and a relative humidity of 13%-17%. The viscous polymer solutions were pumped through the micropipette spinneret (ID=100 µm) and formed an extruded solution droplet at the exit (**Figure 1**(A)). The substrate was mounted on a DC motor, which, in turn, was mounted on a motorized micro-positioning stage with three degrees of freedom (VP-25XA, Newport Inc., USA). After the

substrate made contact with the solution droplet, the fibers were collected on the substrate in aligned configurations. No voltage source was used in the experiments to eject the polymer solution.

Solvent treatment: A fused PMMA fiber network was obtained by exposing the PMMA fiber assembly to chlorobenzene vapor at room temperature in an enclosed chamber for 20 seconds.

Calcination: As-spun PS-titanium-isopropoxide fibers were left in air for 4 hours to allow for the complete hydrolysis of Ti(OiPr)4. PS was removed by treating the fibers in air at 500°C for 4 hours.

Characterization: All measurements were performed at room temperature. The intrinsic viscosity and the Mark-Houwink–Sakurada constants were obtained through dilute solution viscometry experiments. Field-emission scanning electron microscopy (FE-SEM) studies were conducted using an FEI Quanta 600 microscope working at 5-25 kV. Fluorescent images were taken with an Axio Observer (Carl Zeiss Microimaging Inc., USA). Optical images were taken with an AmScope 800 digital camera attached to a 30× microscope (Zeiss Inc., USA).

2.3 STEP Technique

The STEP technique requires ambient atmosphere to evaporate the solvent, leading to the formation of a solid fiber, but more importantly, does not require the aid of an electric field like electrospinning. As shown in **Figure 2.1**(A) (B), a micropipette loaded with polymer solution is connected to a pressure source, leading to an extruded polymer solution droplet at the tip of the micropipette. A rotating substrate is brought in contact with the solution droplet, thus, pulling out a single filament. During the stretching process of the solution filament, continual evaporation of solvent causes an increase in molecular entanglements, thus reducing the overall deformability. A

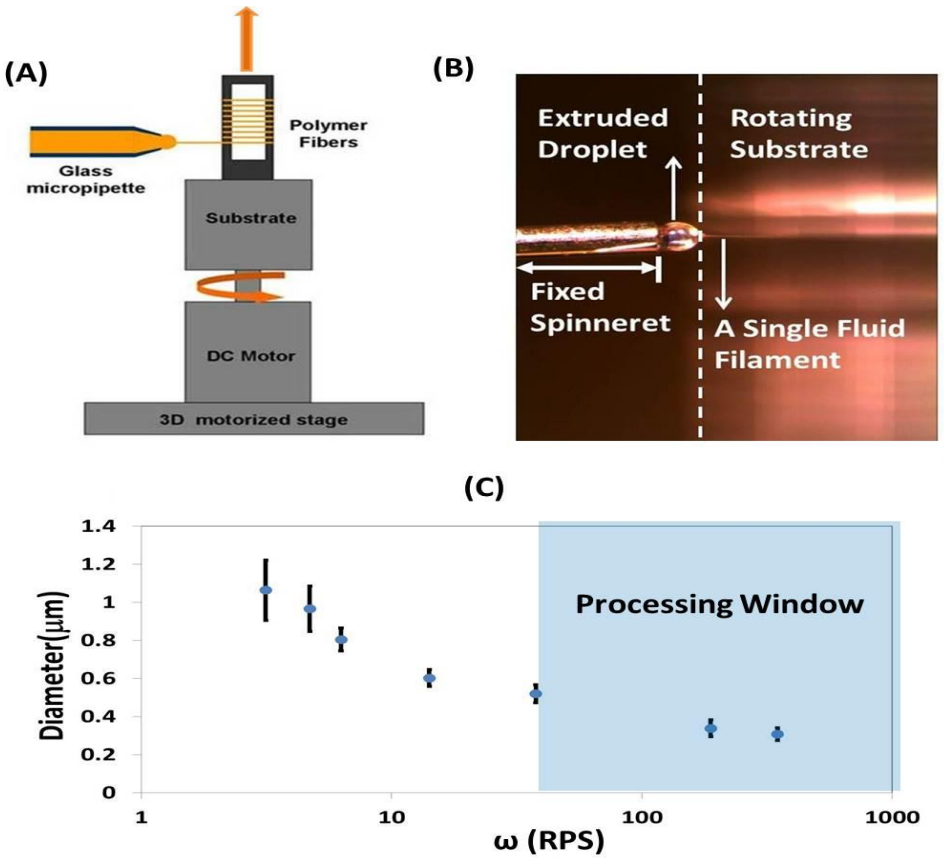

Figure 2.1(A) A schematic illustration of the experimental set-up of STEP technique, (B) an optical image of fiber formation process with the edge of the rotating substrate shown by the dashed line.(C) PS fiber diameter as a function of rotation speed for PS 2000K ($g.mol^{-1}$) 65.1$mg.ml^{-1}$ solution. Fiber diameter was averaged over 50 measurements. Wang et al, Polymer Journal, 2013, 45. Used with permission of Nature Publishing group, 2015

solidified fiber is formed by rapid solvent evaporation and collected on the substrate in aligned configuration. Different from electrospinning, STEP relies on the rotating speed of the substrate rather than an electric field to "stretch and thin" the solution filament. We emphasize that for STEP technique, the fluid filament is pulled out rather than ejected from the tip of the droplet, thus, resembling a fluid element being pulled out from an endless reservoir. As no voltage is involved, both the fluid jet whipping and spraying are avoided in STEP manufacturing, thus, resulting in parallel fiber arrays with narrow fiber diameter distributions.

High aspect ratio fibers of long lengths (mm-cm) having diameters ranging from sub-100nm to microns (aspect ratio: length/diameter > 2000) were obtained by optimizing processing parameters (rotating speed of the substrate) and material parameters (the solution concentration and the polymer molecular weight). For a given polymer solution, the extensional deformation due to filament stretch scales with rotational speed (ω) as shown in **Figure 2.1**(C). In this study, all fibers were obtained at a constant rotating speed ω=40RPS (substrate width=8mm). At this constant rotating speed, we present an engineering design space for fabricating uniform diameter fibers (70-800 nm) of high aspect ratio (> 2000). The isodiametric design space for fabricating continuous fibers is dependent upon achieving a minimum number of polymeric molecular chain entanglements for different molecular weights. The entanglements in a polymer solution are typically represented by critical overlap concentrations (C*) and critical entangled concentrations (C_e). (**Appendix A**)

2.4 Isodiametric Design Space

PS was dissolved in *p*-xylene in increasing concentrations at four molecular weights (650K, 860K, 1500K and 2000K $g.mol^{-1}$). Diameter dependence on solution concentrations (C) was then investigated (**Figure 2.2** A) and was found to scale with C* as:

650K: Dia(nm)= $0.3\left(\frac{C}{C*}\right)^{2.1}$ Eq 2.1

860K: Dia(nm) = $2.9\left(\frac{C}{C*}\right)^{1.4}$ Eq 2.2

1500K: Dia(nm) = $10.3\left(\frac{C}{C*}\right)^{1.1}$ Eq 2.3

2000K: Dia(nm) = $60.7\left(\frac{C}{C*}\right)^{0.7}$ Eq 2.4

The scaling laws were developed using C*, as the critical overlap concentrations were accurately obtained from dilute solution intrinsic viscosity experiments. Similarly, diameter dependence on molecular weight for different concentrations was investigated (**Figure 2.2** B) and found to scale as:

10%wt: Dia(nm)=1E-9 $(M_w)^{1.8}$ Eq 2.5

14%wt: Dia(nm)=4E-8 $(M_w)^{1.6}$ Eq 2.6

18%wt: Dia(nm)=8E-5$(M_w)^{1.1}$ Eq 2.7

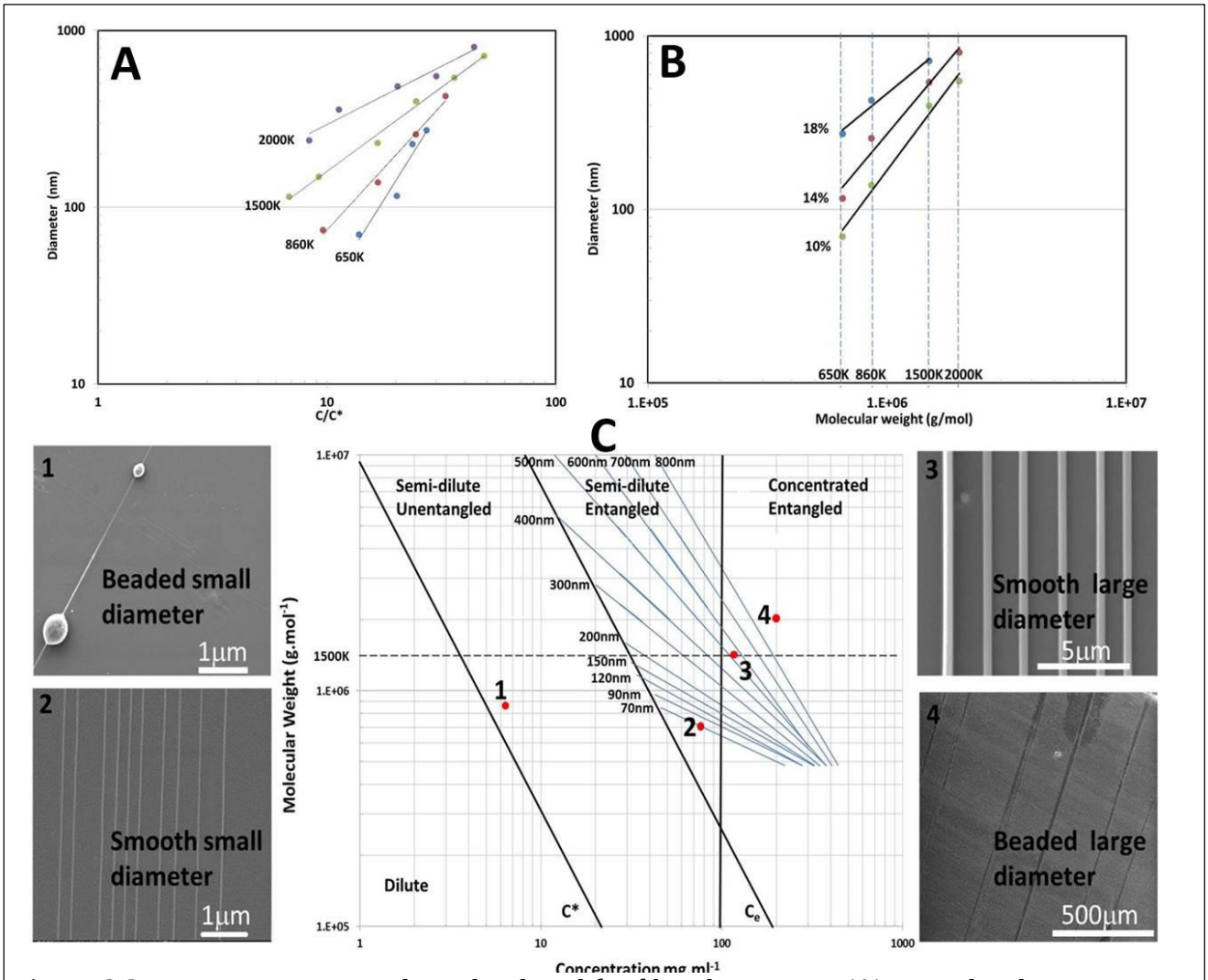

Figure 2.2 Linear regression analysis developed for fiber diameter vs (A) normalized concentration (C/C*), (B) molecular weight,(C) the isodiametric design space for polystyrene nanofibers superimposed on Graessley diagram: blue color lines represent isodiametric lines(numbers on these lines denoting fiber diameters). Inserts 1-4 are representative images corresponding to the 4 points (noted as 1-4) in the design space. Each data point in (A) and (B) is an average result over at least 50 measurements. Wang et al, Polymer Journal, 2013, 45. Used with permission of Nature Publishing group, 2015

From equations 2.1 to 2.4, lower molecular weight species exhibit larger exponents which demonstrate that a higher concentration is required for the formation of polymer chain entanglements necessary to form smooth and uniform fibers. From equations 2.5 to 2.7, decreasing

exponents demonstrate diminishing role of molecular weight in fiber formation process as the concentration increases, which can be explained through the relation between the gyration radius of polymer chain (R_G) and the polymer solution concentration (C): $R_G \sim C^{-1/4}$. [70] An increase in polymer solution concentration makes the polymer chains in solution more compact, thus limiting the effect of molecular weight.

The role of increased polymer chain entanglements with increase in i) molecular weight (at the same concentration), and ii) concentration (at the same molecular weight) is to restrict the ability of individual polymeric chain segments to undergo *physical* deformation in the extensional stress field during the fiber formation process. The scaling laws developed for fiber diameter control (equations 2.1-2.7) are mapped to obtain the isodiametric design space (**Figure 2.2** C). By visual inspection of the isodiameter lines (blue lines) in the mapped design space, it is straightforward to determine regions of solution rheology with sufficient polymer chain entanglements required for fabrication of smooth, uniform fibers with diameters ranging from 70nm to 800nm, having lengths of at least several millimeters. STEP-based uniform diameter fiber arrays were obtained at concentrations closer to and greater than C_e, which signifies the transition from semi-dilute un-entangled to semi-dilute entangled domain. At C_e, the molecular chains are considered to have sufficient overlaps, thus, forming a long range physical entanglement network, which is necessary for continuous fabrication of smooth and uniform fibers. An increase in the concentration beyond C_e leads to compacted polymeric chains due to a decreased number of solvent molecules entrapped in the entangled polymer chain networks, which ultimately results in larger diameters under the same external extensional stress.

The limiting cases for fiber formation of acceptable attributes (smooth, defect free and of substantial length) occur at very low and highly concentrated solution rheologies. At low

concentrations (semi-dilute un-entangled and dilute domains), there are not enough polymer molecules to form long range networks, yielding the classic beaded morphology as shown in insert 1 (corresponding to point 1 in the design space). At the other extreme of highly concentrated rheologies, the absence of solvent molecules leads to the convergence of isodiameter lines, signifying the limits of dry-spinning-based manufacturing methods such as STEP and electrospinning. At these high concentrations, fibers of large diameters (tens of microns) were obtained along with beads, as shown in insert 4 (corresponding to point 4 in the design space), which is comparable to fibers obtained from traditional melt spinning manufacturing methods.[71,72]

Table 2.1 Fiber diameter obtained in PS fiber design space with data in parenthesis obtained through the scaling laws. (Equations 2.1-2.7) .Wang et al, Polymer Journal, 2013, 45. Used with permission of Nature Publishing group, 2015

	Fiber diameter (nm)			
Conc (wt%)	Mw($g.mol^{-1}$)			
	2000K	1500K	860K	650K
2	185±20	Beaded fibers	Beaded fibers	Beaded fibers
3	240±24	72±14	Beaded fibers	Beaded fibers
4	357±52	149±30	Beaded fibers	Beaded fibers
6	(446)	(186)	75±9	Beaded fibers
7	483±64	231±43	(87)	Beaded fibers
10	552±86	397±72	139±19	70±6
14	808±103	541±92	258±29	117±14
16	(958)	(631)	(318)	228±18
18	Macro-fiber	720±116	462±50	274±30

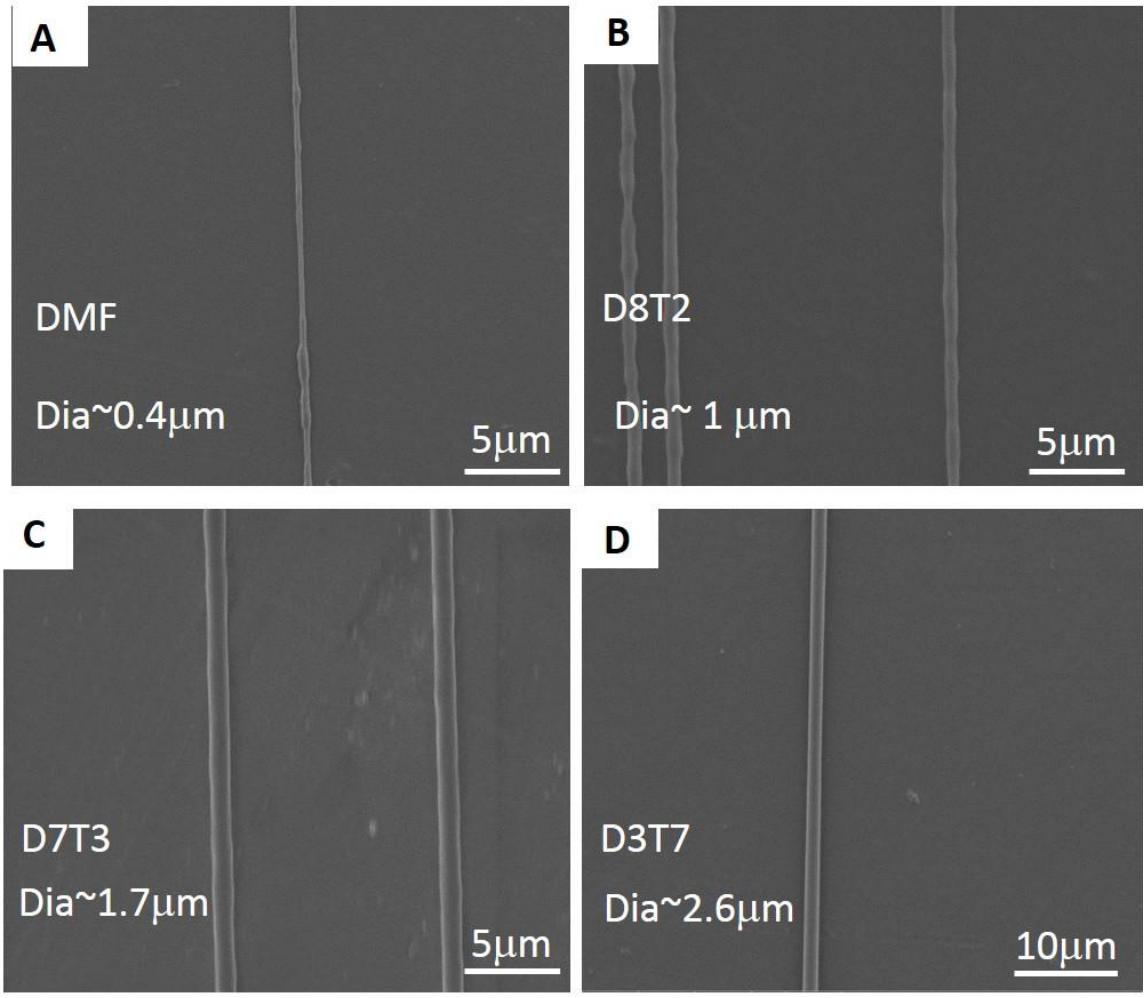

Figure 2.3 Polyurethane fiber obtained from varied solvent ratio (DMF/THF, w/w) at the same concentration (30%w). (A) 100% DMF, (B) 80% DMF and 20%THF, (C) 70%DMF and 30% THF. (D) 30% DMF and 70% THF.

Fibers of increasing diameters were obtained through transition of solution rheologies from semi-dilute to concentrated regimes. As shown in **Figure 2.2** C inserts 2 and 3, aligned 70nm diameter fiber arrays were obtained at semi-dilute entangled region (point 2) while 500nm diameter fiber arrays were obtained at concentrated entangled region (point 3). Fiber diameter distribution is controlled well within 20%, including manufacturing and measurement errors. (**Table 2.1**)

2.6 Polymer Nanofibers Prepared using STEP Technique

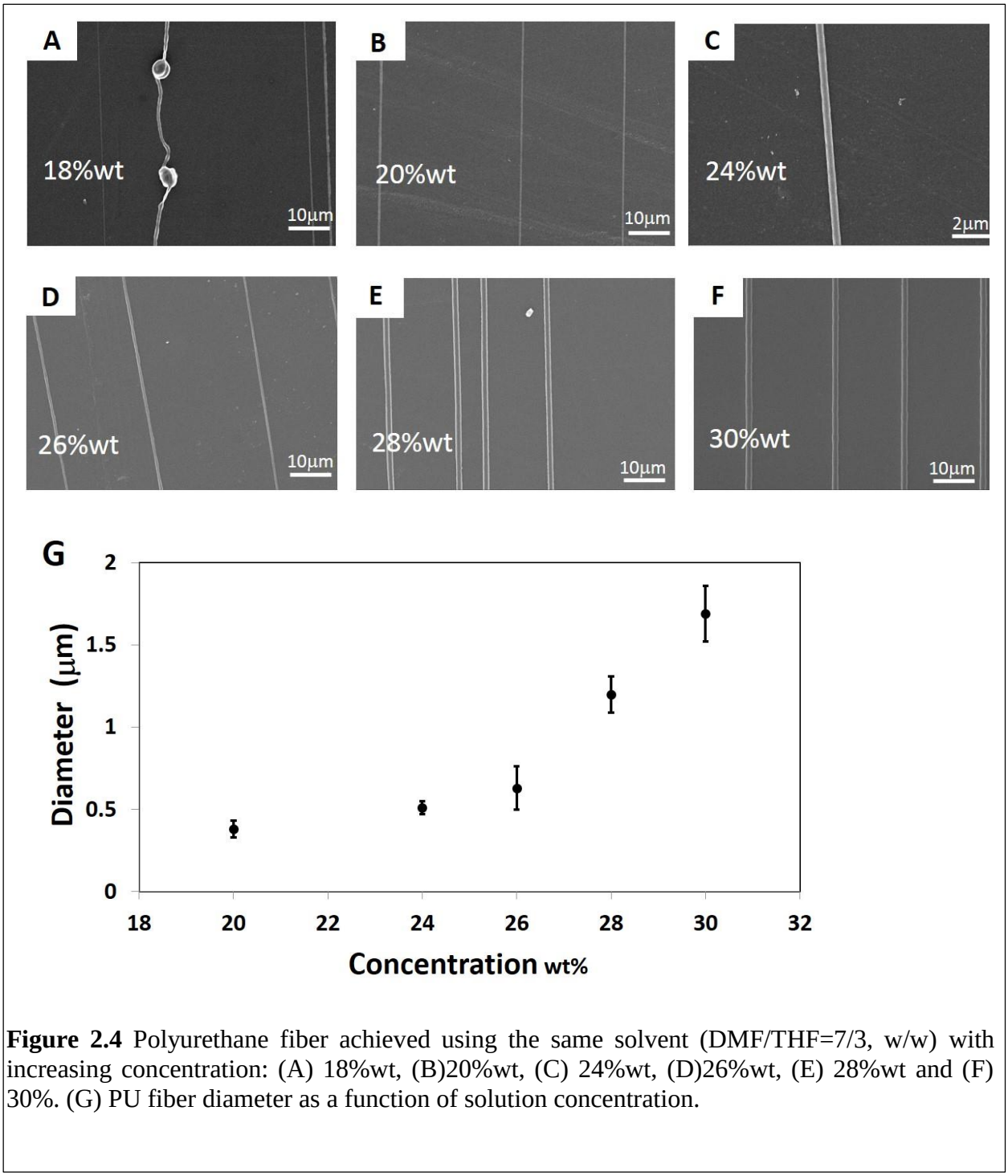

Figure 2.4 Polyurethane fiber achieved using the same solvent (DMF/THF=7/3, w/w) with increasing concentration: (A) 18%wt, (B)20%wt, (C) 24%wt, (D)26%wt, (E) 28%wt and (F) 30%. (G) PU fiber diameter as a function of solution concentration.

The proposed STEP-based methodology is able to achieve nano/micro fiber arrays of various polymer species. Besides solution concentration and molecular weight, solvent volatility is another important processing parameter. To control the solvent volatility, DMF (boiling point 153°C) and

THF (66°C) were mixed at different weight ratio (w/w) as solvent for polyurethane (PU). As the THF component increases in the solvent, the mixed solvent becomes more volatile and larger fiber diameter were achieved as shown in **Figure 2.3**. When using the same solvent (DMF/THF=7/3, w/w), PU fiber diameters scale with solution concentrations as shown in **Figure 2.4**. Note that beaded fibers were obtained at low solution concentration (18%wt). PU fiber diameter increases from 400nm to 1.7 μm as solution concentration increases from 20% wt to 30%wt.

Fibrinogen fibers were also prepared through the STEP technique using HFP (bp 59°C) as solvent (**Figure 2.5)**. However, the fast evaporation of HFP leads to rapid solidification of the solution droplet, which blocks the spinneret and leads to discontinuity of the fiber spinning process. In order to achieve continuous fiber spinning, saline (0.9% wt NaCl solution) was used as the solvent

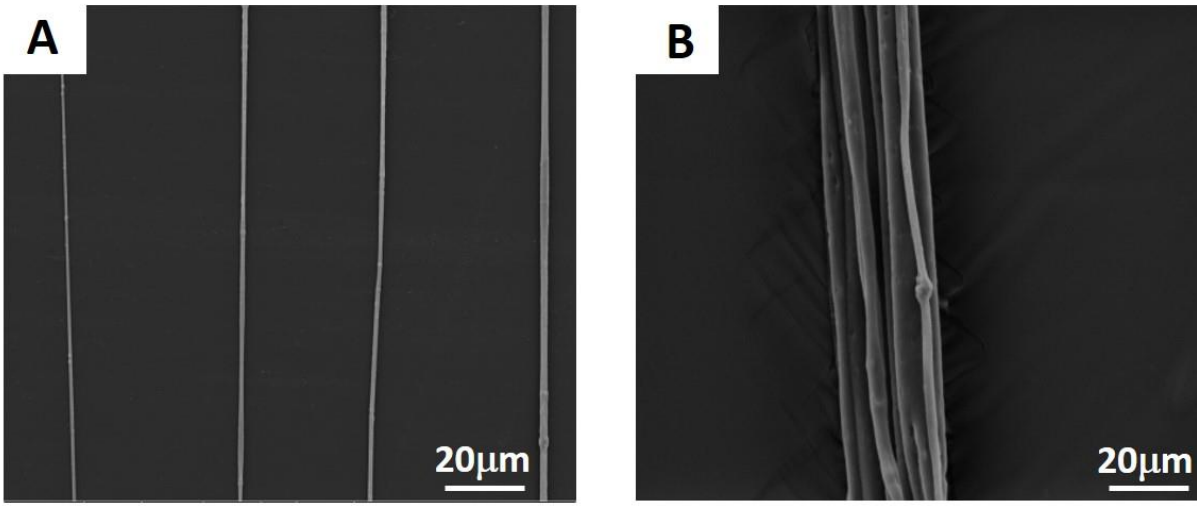

Figure 2.5 Fibrinogen fibers prepared through the STEP technique using HFP as solvent.

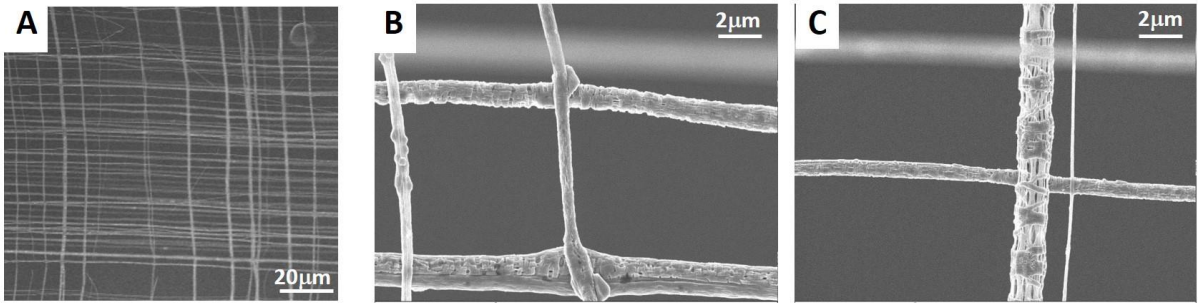

Figure 2.6 (A) Fibrinogen fiber scaffolds. (B)(C) Porous fibrinogen fibers.

for fibrinogen. The solubility of fibrinogen in saline is 10mg/ml, which is not enough to form smooth and continuous fibrinogen fibers. To increase the spinnability, 1%wt PEO (Mw=4000k) was added into fibrinogen/saline solution. As-spun PEO/fibrinogen fibers were exposed to glutaraldehyde vapor in a chamber for 30mins to crosslink fibrinogen. The PEO in as spun fibers were subsequently leached out in water and pure fibrinogen fibers were achieved. Using this approach, continuous fiber spinning process was realized and fibrinogen fiber scaffolds were achieved as shown in **Figure 2.6** (A)**.** Note that the leaching of PEO leads to porous fibrinogen fibers as shown in **Figure 2.6** (B) (C).

Besides PU and fibrinogen, STEP technique has been extended to other polymer species and highly aligned polymer fiber patterns are achieved. **Figure 2.7** (A) presents parallel PEO nanofiber arrays (diameter: approximately 400 nm), while **Figure 2.7** (B) demonstrates a PLGA fiber (diameter 150-500 nm) assembly. **Figure 2.7** (C) shows an inter-connected PMMA fiber network composed

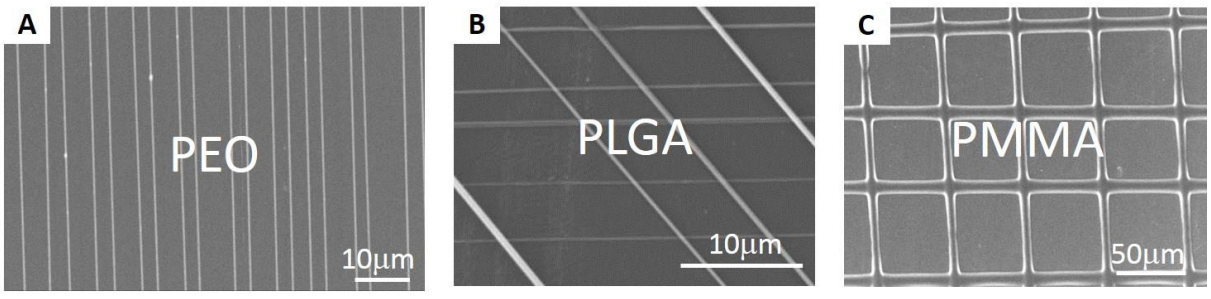

Figure 2.7 Fiber assemblies made from various materials: (A) parallel unidirectional PEO fibers, (B) a PLGA nanofiber assembly, and (D) an inter-connected orthogonal PMMA fiber network. Wang et al, Polymer Journal, 2013, 45. Used with permission of Nature Publishing group, 2015

of 3×4 equal size unit cells that was obtained by treating the crisscross PMMA fiber assembly with solvent vapor. The PMMA fibers became flat ribbons of 4-5 μm in width and were fused at intersections.

2.5 Conclusion

In conclusion, an isodiametric design space is developed to deposit PS fibers having diameters ranging from 70nm to 800nm with lengths of at least several millimeters. The molecular entanglement based scaling laws are used to investigate the role of polymer chain entanglements on fiber formation and demonstrate that smooth, uniform fibers of substantial length are obtained at concentrations approaching and exceeding the critical entangled concentration (C_e). Visual inspection of the isodiametric design space provides knowledge of polymer molecular weight and solution concentration rheology required to fabricate continuous high aspect ratio fibers.

Chapter 3 Aligned Polystyrene Tubes with Controlled Morphologies

Ji Wang, Junbo Hou, Eduardo Marquez, Robert B.Moore, Amrinder Nain, Polymer, 2014, 55, 3008-3014. Used with permission of Elsevier publishing group, 2015.

3.1 Introduction

Micro/nano tubes are finding increasing potential for applications in a wide range of emerging fields: fluid storage for fuel cells, catalysis, drug release and photonics.[73,74] This is due to their high specific interface area, which strongly enhances the reactivity, absorption rate as well as the efficiency of transport within and across tube walls.[75] To prepare tube structures, three approaches are commonly employed: self-assembly, tubes by fiber templates (TUFT) and co-electrospinning process. Self-assembly strategy includes assembly of rod-like sub-units into barrel shaped frameworks. Linear sub-units, such as natural antibiotic gramicidin A, can form tubular structures by coiling into helical conformations.[54,55,76] TUFT uses polymer nanofibers as templates, which are coated with precursor materials. Tube structures are obtained by selective dissolution or thermal degradation of the polymer nanofibers. [53,77] Compared with the other two approaches, co-electrospinning is more commonly used due to its simplicity and versatility. During a co-electrospinning process, two immiscible solutions are simultaneously spun into core/shell fibers from a spinneret containing coaxial capillaries. Tube structures are then typically obtained by selectively removing the core. [58,78]

To date, tubular structures made from peptides, polymers, and ceramics have been obtained. However, challenges in precise control of tube alignment and morphologies still need to be addressed. Herein, we report an effective and robust approach to fabricate highly aligned PS tubes based on a recently reported non-electrospinning STEP technique. The STEP technique provides unique control on tube i) alignment, ii) spacing, iii) length, iv) diameter (sub 100nm to several microns), and v) scalability to develop assemblies. We demonstrate that appropriate selection of

solvent, humidity and solution concentration results in porous tubes, which display excellent absorption capacity.

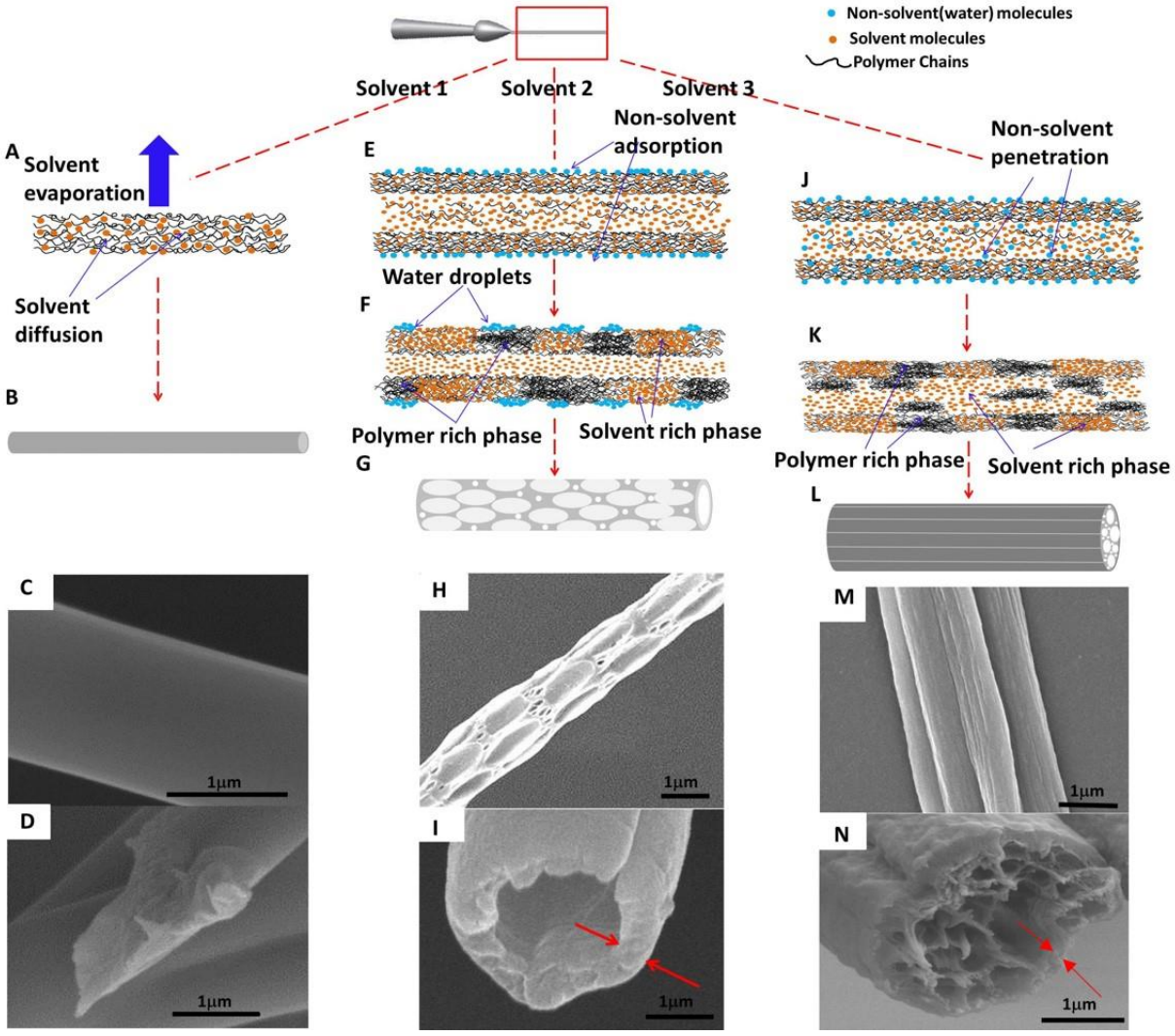

Figure 3.1 (A)-(B) schematic illustration of smooth solid fibers formation, SEM images of a side view (C) and cross section (D) of smooth solid fibers, (E)-(G) schematic illustration of porous tubes formation, SEM images of a side view (H) and cross section (I) of porous tubes, (J)-(L) schematic illustration of wrinkled porous fibers formation, SEM images of a side view (M) and cross sections(N) of wrinkled porous fibers. Red arrows in (I) and (N) indicate the thickness of the skin layer. Wang et al, Polymer, 2014, 55. Used with permission of Elsevier publishing group, 2015.

3.2 Experimental Section

Chemicals and Materials: All chemicals were used as received without further purification. Polystyrene (PS) (M_w=2000 kg.mol^{-1}, Scientific Polymer Products Inc, USA) was dissolved at room temperature in *p*-xylene and *N*,*N*-dimethylformamide (DMF) mixtures with volume ratios of 100:0, 50:50 and 15:85. MWCNTs (diameter in the range 10-20 nm, length in the range of 10-20 μm) were dispersed mechanically in PS solution by an 8 hour sonication treatment at room temperature followed by continuous mechanical mixing before spinning.

STEP Spinning: In a typical STEP spinning process, viscous polymer solutions were pumped through a micropipette spinneret (ID=100 μm). The rotating speed of the substrate was set at 40 RPS for all experiments. All spinning processes were performed at room temperature (25°C).

Characterization: The viscosity of polymer solutions and commercial oils was determined using an AR 2000 rheometer (TA Instrument, USA). To determine the solvent evaporation rate, 10 mL of solvent was injected into a 6-cm diameter glass petri dish, which was placed on an analytical balance to record the weight loss every minute. All measurements were conducted at 25°C. The morphology and cross-section of STEP spun fibers were examined through a field emission scanning electron microscope (FESEM, LEO 1550, Zeiss, USA). For TEM (Philips, EM420) characterization, as spun fibers were carefully collected on a carbon coated copper grid. The specific surface area (SSA) of the fibrous mats was obtained from nitrogen physi-absorption data in the relative pressure range from 0.01 to 0.99 using the Brunauer-Emmett-Teller method. Tensile tests of the fibrous mats were performed on a micro-force testing system (TYTRON 250, MTS) with a 5N load cell operating at 1mm/min strain rate.

Oil Absorption: To analyze the maximum oil absorption capacity of fibrous sorbents, 10 mg of absorbents were placed in a glass beaker filled with 100 mL of oil. After 40 min of absorption, the wet absorbents were drained for 5 minutes and weighed. Oil absorption capacity of the absorbents was determined by the following equation:

$$Q = \frac{m_f - m_0}{m_0} \qquad \text{Eq 3.1}$$

Where Q is the absorption capacity ($g \cdot g^{-1}$), m_f is the weight of the wet sorbent after 5 min of drainage (g), and m_0 is the initial weight of the sorbent (g). The absorption capacity was averaged over three samples.

3.3 Polystyrene Tube Structure

STEP fiber morphology is related to solution filament solidification and phase separation process. Solidification involves both solvent molecules diffusing to solution filament surface and evaporating from the surface. As solution filament solidifies, phase separation (separation of solvent rich phase from solvent poor phase) can be triggered by moisture content in the ambient atmosphere, causing pores to develop on the fiberfiber surface. Both solidification and phase separation are affected by solvent polarity and volatility, which can be tuned by mixing a low polarity and low boiling point solvent p-xylene (polarity index 2.5, bp 138°C) with a high polarity and high boiling point solvent DMF (polarity index 6.4, bp 154°C). In order to examine the effect of solvent polarity and volatility on fiber formation process, we spun fibers at 45% relative humidity (RH) from PS/solvent concentration ($99.2 mg.mL^{-1}$) solutions with three different solvents: (i) pure p-xylene (control), (ii) 50:50 (v:v) DMF with p-xylene, and (iii) 85:15 (v:v) DMF with p-xylene.

For the pure PS/p-xylene system (solvent i), the solvent evaporation rate being high causes rapid solvent removal from the solution filament (**Figure 3.1** A, B) resulting in a solid polymer fiberfiber with uniform cross-section (**Figure 3.1** D). In this scenario, moisture in the ambient atmosphere is not absorbed to the solution filament surface due to the low polarity of the solvent, thus giving rise to a smooth fiber surface (**Figure 3.1** C). Next, by mixing 50:50 (v:v) DMF with p-xylene (solvent ii), the increased polarity causes moisture in the air to condense on solution filament surface (**Figure 3.1** E). Upon water evaporation from the surface, imprints were formed which resembled "pits" (**Figure 3.1** F, G)). [79] Given the high miscibility of DMF and water, absorbed moisture

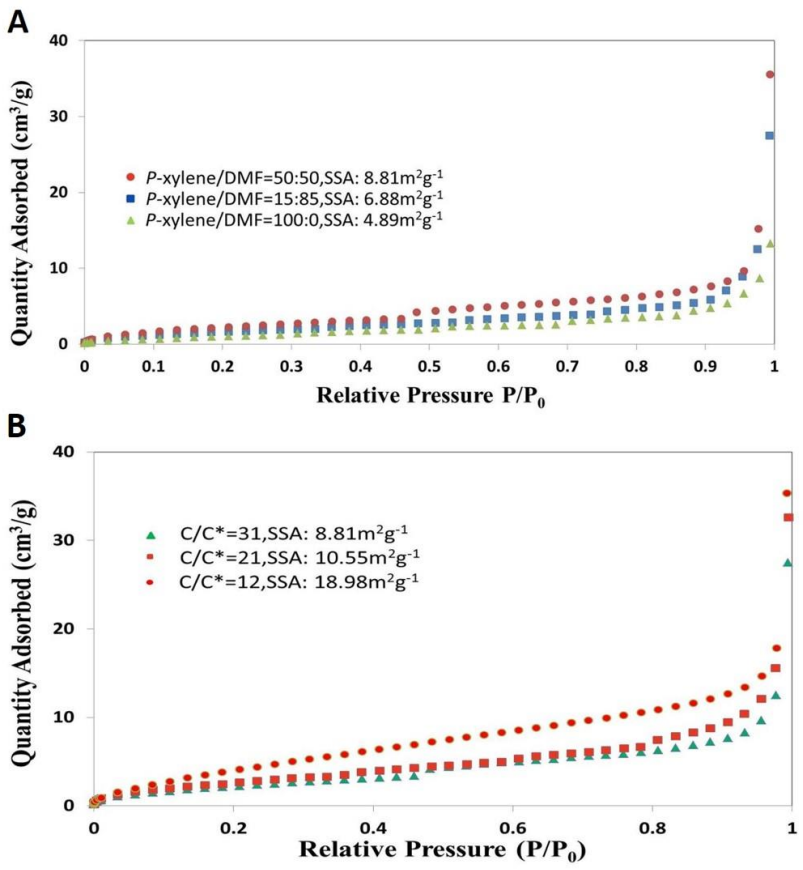

Figure 3.2 (A) Nitrogen adsorption isotherms of PS morphologies formed from different solvent composition, (B) Nitrogen adsorption isotherms of PS porous tubes made from varied concentrations (C/C*=12,21,31). Wang et al, Polymer, 2014, 55. Used with permission of Elsevier publishing group, 2015.

in the polymer-/solvent system decreased PS solubility, thus triggering vapor induced phase separation.[48] As shown in **Figure 3.1** (H), polymer rich phase solidified while solvent rich phase

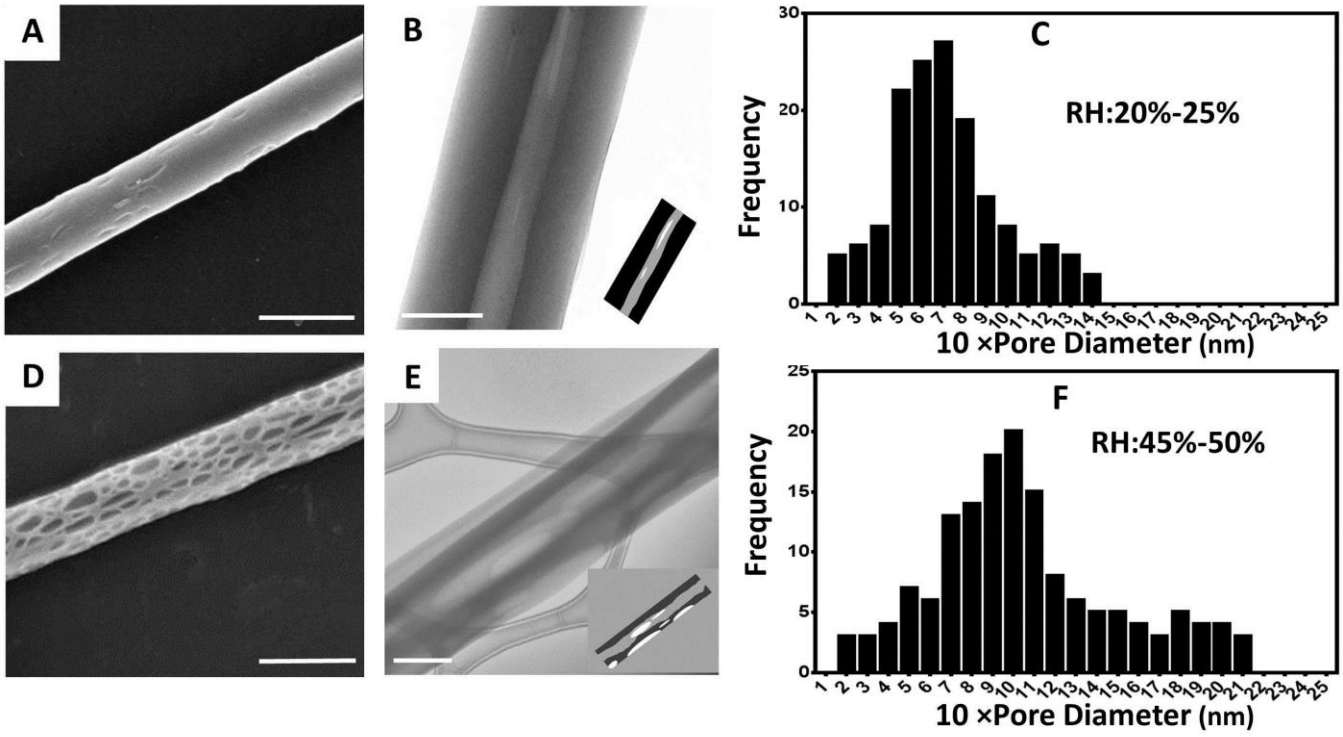

Figure 3.3 (A)-(C) PS porous tubes formed at RH 20-25%: (A) SEM, (B) TEM images of the tube structure, (C) diameter distribution of pores on the tube surface. (D)-(F) PS tubes formed at RH 45%-50%: (D) SEM, (E) TEM images of the tube structure, (F) diameter of pores on the tube surface. Scale bars are 200 nm in (A) and (D) and 100 nm in (B) and (E). Inserts are schematic illustrations of the porous tube morphologies. 150 pores were measured for each RH (Figure C and F). Wang et al, Polymer, 2014, 55. Used with permission of Elsevier publishing group, 2015.

Table 3.1 Pore diameters under varying humidity levels . Wang et al, Polymer, 2014, 55. Used with permission of Elsevier publishing group, 2015.

Humidity range	pore diameters range (nm)	Most frequent pore diameters (nm)	Pore area ratio (total pore area/fiber surface area)
20-25%	20-140	50-80	4.1%
45-50%	20-210	60-110	24.5%

eventually became pores. Furthermore, since solvent evaporation is exclusively taking place from the boundary, a skin layer which is rich in polymer is established at the early stage of solidification.[80,81] As shown in **Figure 3.1** (E, F), the solidifying solution filament consists of a solvent rich core surrounded by a polymer rich shell. As solvent is removed from the core of the filament, a compressive radial stress is generated on the shell, which can be estimated through:[82]

$$\sigma = \frac{r}{\Delta R}\Delta P \qquad \text{Eq 3.2}$$

where r is the fiber radius, ΔR is the shell thickness, and ΔP is the pressure difference across the shell, usually taken as atmospheric pressure. Based on SEM measurements of fiber cross sections (r ~1.81±0.41μm, ΔR ~0.49±0.17μm), the radial stress ranges from 0.2 to 0.6 MPa. Interestingly, the tubes are observed to maintain their cylindrical appearance, indicating that the tube walls are able to sustain the compressive radial stress. Furthermore, using the method outlined in this work, we have observed tube formation for PS fiber diameters as low as 0.3μm, which is in agreement with the theoretical predictions of Guenthner et al,[83] that formation of stable tube structures by evaporation is more likely to take place in small diameter fibers with diameter of hundreds of nanometers. For even larger diameters (dia>5μm), Koombhongse et al. have reported flat ribbon morphologies using single nozzle electrospinning process, which are believed to be collapsed thin skin layers initially formed in solution filament solidification process.[84] Note that the tube outer diameter range achieved in this study (0.3-3.6μm) is comparable to the tube dimensions (outer dia 0.3-4 μm) reported in the past fabricated by co-electrospinning technique, in which a core aqueous solution is needed for precipitation of the shell polymer. [60,78] Instead of conducting coaxial electrospinning, this study demonstrates a convenient alternative approach to achieve polymer tube

structures through tuning solvent evaporation.

As DMF volume ratio was increased to 85% in the mixture (solvent 3), the boiling point of the solvent was further raised, which in turn lowered the solvent evaporation rate and prolonged the fiber solidification process. In this case, moisture in the air penetrated into the interior of the solution filament and initiated vapor induced phase separation (VIPS) (**Figure 3.1** (J-L)), as evidenced by the porous morphology at the core (**Figure 3.1** (M)(N)). Pai et al. reported similar porous core morphology when they electrospun PS fibers in a high humidity environment (RH=37%-43%).[85] Based on the nitrogen adsorption isotherms, the BET specific surface area (SSA) was obtained for varied fiber morphologies. Both porous tubes and wrinkled porous fibers demonstrated higher SSA (8.81 $m^2.g^{-1}$ and 6.88$m^2.g^{-1}$ respectively) than smooth solid fibers (4.89 $m^2.g^{-1}$**).** (**Figure 3.2** (A))

Relative humidity (RH) has been extensively reported to play an important role in controlling fiber surface morphologies.[86–88] In this work, RH was varied to achieve control on tube wall porosities. As shown in **Figure 3.3** (A, B), at low RH (20%), only a few pores were observed on tube walls. On the other hand, at high RH (45%), the tube walls become saturated with pores, as shown in **Figure 3.3** (D, E). Both pore size and distribution are observed to increase with RH, which can be attributed to the coalescence of smaller pores into larger ones. Casper et al. have reported a similar trend of pore size evolution on electrospun fiber surfaces.[46] The pore diameter and distribution observed at both humidity ranges is summarized in **Figure 3.3** (C, F) and **Table**

3.1.

To control the dimensions of the porous tubes, solution concentration was varied in solvent 2

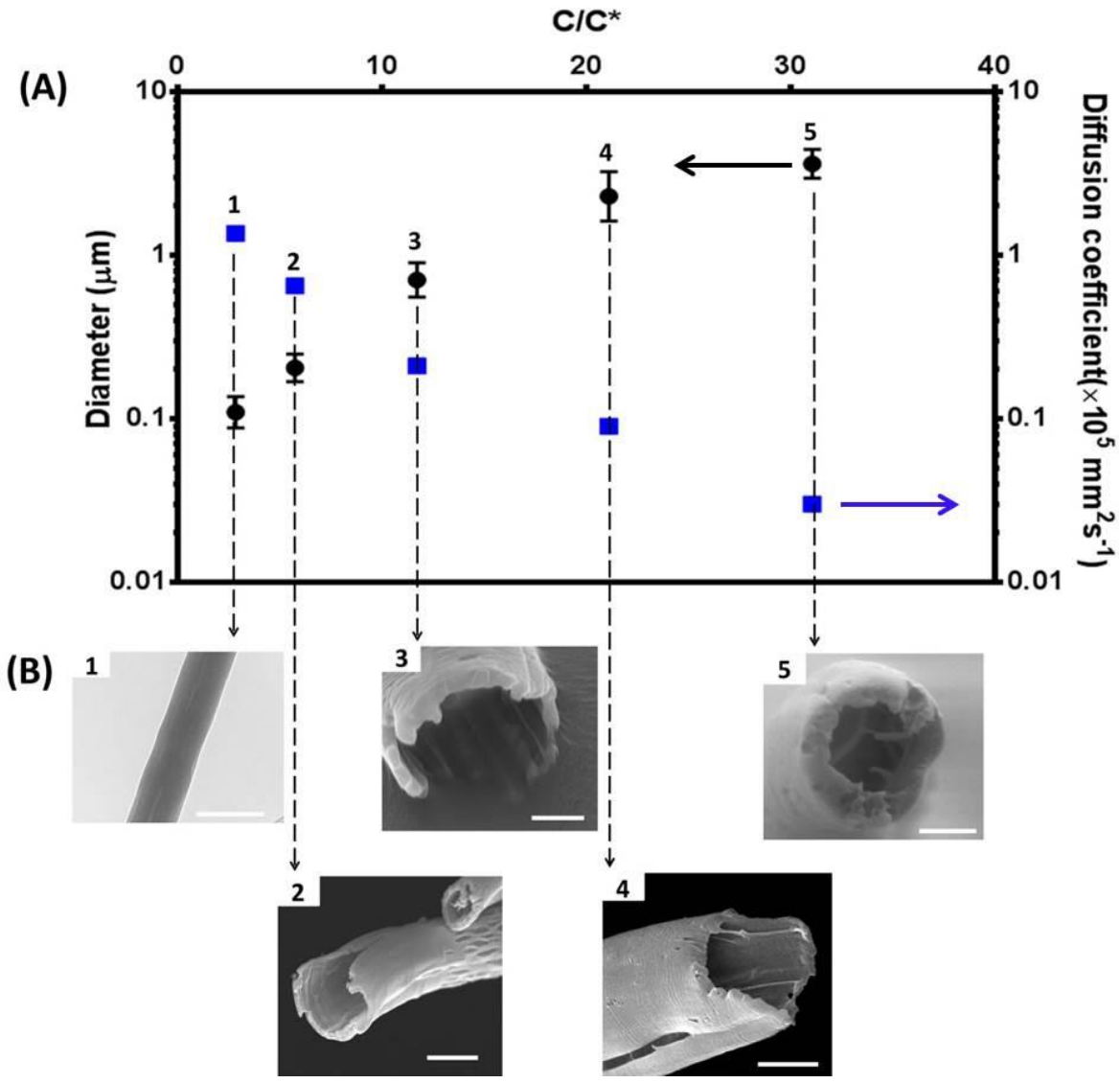

Figure 3.4 (A)PS fiber outer diameter(solid circle) and solvent diffusion coefficient(solid square) as a function of entanglements (C/C*). (B) 1-5 are PS fiber morphologies obtained from C/C*= 3, 6, 12, 22, 31 respectively. Scale bars are 200 nm in B 1- 3 and 1 μm in B 4-5. Wang et al, Polymer, 2014, 55. Used with permission of Elsevier publishing group, 2015.

(50:50=xylene: DMF) under fixed relative humidity (RH~45-50%). By increasing solution

Table 3.2 PS tube wall thickness as a function of entanglements Wang et al, Polymer, 2014, 55. Used with permission of Elsevier publishing group, 2015.

Solution concentration C ($mg.ml^{-1}$)	Entanglements C/C*	Tube Wall Thickness (μm)
9.6	3	Solid fibers
19.2	6	0.05±0.03
38.4	12	0.16±0.04
67.2	21	0.27±0.08
99.2	31	0.49±0.17

concentrations, polymer chain entanglements (characterized as C/C*, where C* is the critical overlapping concentration 3.2 $mg.ml^{-1}$ for 2000K $g.mol^{-1}$ PS in p-xylene) are increased, which restricts the stretching of polymer solution filament in the extensional stress field during the fiber formation process. [44, 45] As a result, fiber diameter was increased from 100 nm to more than 2 μm, as shown in **Figure 3.4** (A). Also, increased polymer chain entanglements lower the solvent molecule diffusion coefficient. (**Appendix B**). At relatively low entanglements (C/C*=3), small diameters provide large specific surface area, which facilitate rapid evaporation of solvent. In addition, the solvent diffusion coefficient is high, which favours diffusion of solvent molecules to the fiber surface. As a result, solvent was rapidly removed from the system and a solid fiber was achieved (**Figure 3.4** (B)). As reported in previous study, for both electropspinning and STEP spinning technique, as entanglements increase, [44, 46, 47] larger diameter fibers are obtained, which decrease the specific surface area (surface area per unit mass). In addition, the diffusion coefficient is significantly reduced. Both the increase in fiber diameter and decrease in diffusion coefficient lead to a slow solvent removal process. As a result, a polymer rich shell is initially

formed, which can subsequently develop into tubes after solidification. As demonstrated in **Figure 3.4** (B), tubular structures were obtained when C/C* was above 6. Continuous production of long tubes was achieved as C/C* reached 12, where large scale tube mats can be easily prepared for diverse applications. It was found that Increase of solution concentration also causes increased tube wall thickness, as summarized in **Table 3.2**. According to nitrogen adsorption results (**Figure 3.2** (B)), the tube structures made from (C/C*=12) show a SSA of 18.98 $m^2.g^{-1}$, which is higher than the tubes made from C/C*=21 (10.55 $m^2.g^{-1}$) and C/C*=31 (8.81 $m^2.g^{-1}$). This could be attributed to the relatively small tube diameters formed at C/C*=12.

3.4 Application in Selective Absorption

In applications such as selective absorption, pores in the tube wall may cause stress concentration and lead to poor mechanical strength. To increase the strength, 2 wt% MWCNTs were added to the polymer solutions to reinforce the resultant structures made from C/C*=12. As shown in

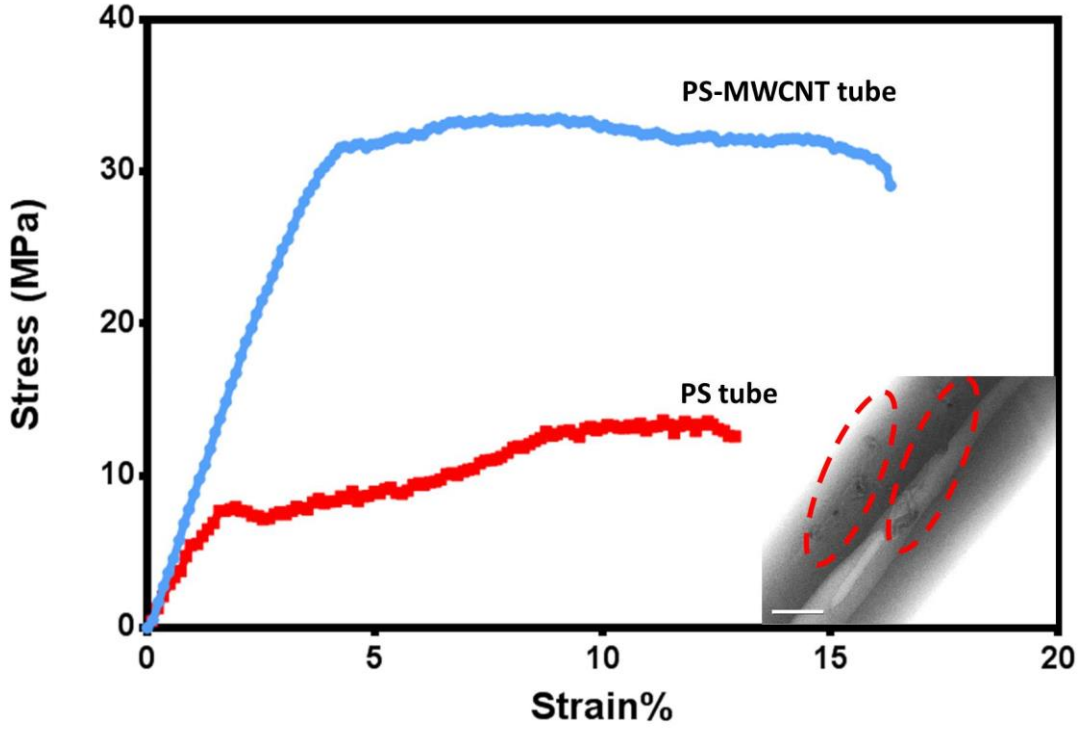

Figure 3.5 Typical stress-strain curves of PS tubes and PS / MWCNT tubes. Insert: TEM image of MWCNTs within PS tubes with scale bar: 50 nm. Red circles highlight the aligned MWCNTs. Used with permission of Elsevier publishing group, 2015.

Table 3.3 Mechanical Properties of PS tubes and PS/MWCNT Tubes. Used with permission of Elsevier publishing group, 2015.

	Diameter (μm)	**Ultimate Strength (MPa)**	**Elongation to failure %**
PS/MWCNT tubes	0.66±0.27	35.8±7.1	18.7±3.5
PS tubes	0.71±0.19	16.3±2.7	13.6±2.7

Figure 3.5 and summarized in **Table 3.3**, stress-strain curves of the resultant tubes demonstrate a

marked improvement in tensile strength. By incorporating MWCNTs, ultimate strength is enhanced from 16.3±2.7 to 35.8±7.1 MPa, while average elongation to failure is increased from 13.6% to 18.7%, demonstrating improvements of 119% and 37%, respectively. Subsequent TEM analysis (**Figure 3.5** insert) indicates MWCNTs alignment along the tube axis, which may be contributing to the increased tensile strength.

Next, the hydrophobic properties of PS/MWCNT tube mats were characterized through oil contact angle (OCA) and water contact angle (WCA) measurements. The oil droplets were immediately absorbed by the tube mat, whereas water droplets remained stable on the tube mat and exhibited a large WCA ~ 119°. (**Figure 3.6**) To determine the absorption capacities of the PS/MWCNT tubes,

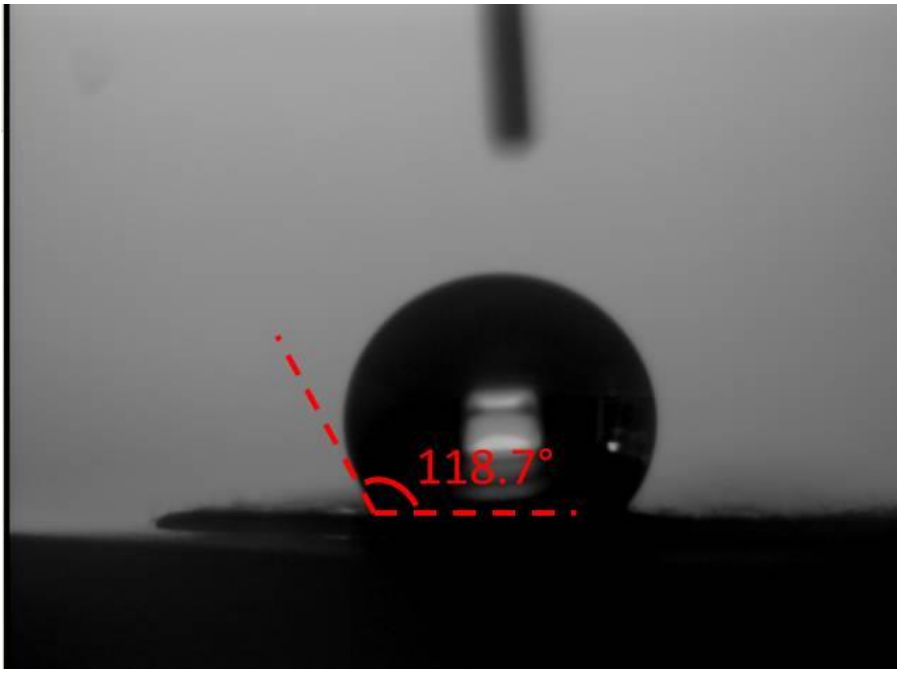

Figure 3.6 Water contact angle on a PS/MWCNT tube mat. Wang et al, Polymer, 2014, 55. Used with permission of Elsevier publishing group, 2015.

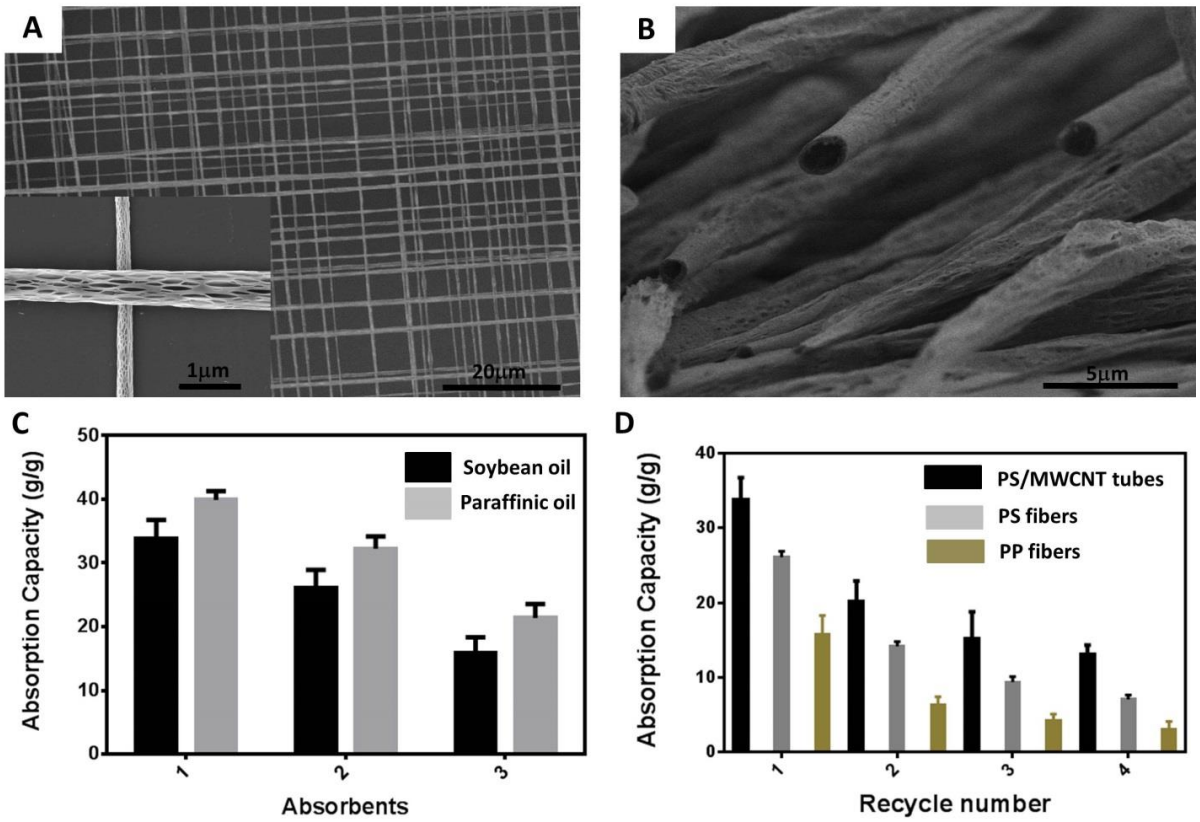

Figure 3.7 (A) A aligned PS/MWCNT tube mat, insert is a zoomed-in area of the mat, (B) cross-section of the tube mats, (C) oil absorption capacity of PS/MWCNT tubes (absorbent 1), smooth PS fibers (absorbent 2) and non-woven PP fibers (absorbent 3), and (D) recycled absorption capacity of PS/MWCNT tubes, smooth PS fibers and non-woven PP fibers. Wang et al, Polymer, 2014, 55. Used with permission of Elsevier publishing group, 2015.

10×10 cm^2 mats comprising a cross-hatch pattern of tubes were prepared using STEP technique, as shown in **Figure 3.7** (A, B). **Figure 3.7** (C) compares oil absorption capabilities of three fibrous absorbents. Smooth PS fiber and PS/MWCNT tubes have significantly higher oil absorption capacities than commercial absorbents such as non-woven polypropylene (PP) fibers, and this can be attributed to the difference in diameters (PS fiber diameter ~800 nm, PS tube diameter ~700 nm, PP fiber diameter ~20 μm) PS/MWCNT tube mats have oil absorption capacity of 33.8g.g-1 for soybean oil and 39.8 g.g-1 for paraffinic oil respectively, which is higher than that of smooth PS fiber mats (26.1 g.g-1and 32.2 g.g-1 respectively). The reason could be their porous hollow

structure, which provides larger area for oil anchoring.[85,89] Note that the oil absorption capacity is higher for more viscous paraffinic oil (paraffinic oil viscosity 68mPa·S, soybean oil viscosity 39mPa·S), which has better adherence on the absorbent surface. [90] To compare the reusability, absorbents with soybean oil were squeezed under 5KPa pressure to remove the absorbed oil and then reused, as shown in **Figure 3.7**(D). For all absorbents, the oil absorption capacity decrease after each cycle, which could be attributed to the reduction of inter-fiber voids during the squeezing process. Note that compared with the other two absorbents, the PS/MWCNT tube mats maintained considerable oil absorption capacity after three cycles.

3.5 Conclusion

In conclusion, through manipulating solvent composition, relative humidity and solution concentration, porous tube structures were obtained directly through solvent evaporation using the STEP technique. For the first time, we demonstrate long porous tubes with surface pores. Incorporating MWCNTs into the tube structures significantly improved the tube mechanical properties. Orthogonal assemblies of aligned tubular structures with MWCNTs in multiple layers demonstrated excellent absorption capacities. We envision that the procedures and methods outlined in this study can be extended to provide organized micro/nano fibers with controlled surface and interior features for a diverse range of applications.

Chapter 4 Mechanical Characterization of a Single Polymer Nanofiber

4.1 Introduction

Recent advances in nanotechnology has enabled nanofibers made from various materials, such as polymers, carbon and semiconductors, which have been used for a wide range of applications, including tissue engineering, filter media, fuel cells and photonics.[57,91–97] One of the motivations for the miniaturization process of materials is the mechanical properties that nano-sized material possess as compared to bulk materials. However, due to the reduced size of fibers, characterizing single nanofiber mechanical properties is challenging and there are two major problems to be addressed:

1. Establishing solid boundary conditions for extremely small diameter fibers is difficult.
2. The load needed to deform a single nanofiber is in the range of nano Newton, which is below the resolution of most commercial mechanical testing system(~0.1mN).[98]

In the past decade, several approaches have been developed to characterize single nanofiber mechanical properties, including tensile tests, three point bending, and nanoindentation.

Tan *et al* conducted tensile tests on single electrsopun PEO fibers (diameter ~700nm). One end of the fiber was attached to a movable stage and the other end to an AFM cantilever. By moving the stage, the fiber was deflected and the forced was measured through deflection of the cantilever. Using this method, Liu *et al* obtained the Weibull distributions of PMMA nanofiber (diameter 380±61nm) strength and CNT/PMMA composite nanofiber (371±48nm) strength. [99] However, it is time consuming to manipulate single nanofibers, especially for sub 250nm diameter fibers. [100] Similarly, AFM cantilevers have also been used for conducting CNTs tensile tests in SEM. [63,101] This method can be applied easily to CNTs but not for polymer nanofibers, which can be

damaged by electron beams. Using a commercial nanotensile testing system (Nano Bionix System, MTS), Tan et al and Wong et al conducted tensile tests on single PCL nanofibers (diameter 500-1700nm) respectively. [102,103] Their results demonstrates that reduced fiber diameter leads to improved mechanical strength. Due to the resolution of the tensile test system (50nN), it is difficult to characterize strength of polymer fibers with sub 100nm diameters.

Bending test for nanofibers is a commonly used approach to detect single nanofiber modulus. Nanofibers are deposited on a substrate with grooves or holes so that a section of the fiber is suspended and an AFM cantilever is used to deflect the suspended fiber at the middle. Samples tested using this method includes CNTs[104,105] , polymer nanofibers [106,107]and biodegradable nanofibers[108]. Using this approach, Tan and Lim characterized Young's modulus of PLLA nanofiber (diameter 250nm-400nm)[61]. With the same method, Sung *et al* characterized the elastic modulus of TiO_2 nanofiber. (diameter 50nm-150nm) [62] Recently, Yang et al demonstrated the bending moduli of electrospun collagen type I fibers (diameter 100-600nm) ranged from 1.3 to 7.8 GPa at ambient conditions and ranged from 0.07 to 0.26 MPa when immersed in PBS buffer.[109] Using the nanoscale three-point bending test, Ding et al found that the elastic modulus of nylon-6/SiO_2 nanofibers (diameter 100-600nm) increased with reduction of fiber diameters.[110] However, whether the adhesion between the sample fiber and the substrate is sufficient for the bending test to be conducted without slippage at the fixed ends remains as a problem. [111,112] In addition, there is a need to ensure that there is no indentation being made on the nanofiber by the AFM tip during deflection.

Another widely used nanomechanical characterization technique is nanoindentation. Nanoindenation tests can be conveniently performed by simply depositing nanofibers on a flat and rigid substrate. Elastic properties of the material can be obtained from the indentation data. Li *et*

al performed nanoindentation on silver nanowires (diameters 42nm-4000nm) [113] and Wang *et al* indented silk fibers (diameter ~800nm) using an AFM cantilever tip.[114] Chen *et al* recently characterized the modulus of ZnO nanofibers (diameter 50-300nm) with nanoindenation approach. In comparison with bulk ZnO, the modulus of ZnO nanofibers demonstrates a decrease of 34%, which indicates the size effects of mechanical behaviors. [115] Using the same approach, Chen and Xu et al measured the elastic modulus of graphite nanofibers (diameter 100-300nm), which is 88±23 GPa.[116] Although the sample preparation process is straightforward, there are several problems that need to be considered for the nanoindenation approach. First, the hard substrate can contribute to the elastic modulus if the fiber diameter is too small (<200nm). [117] Second, fiber surface curvature and surface roughness has to be taken into account. Since the indentation depth is about the same order of the surface roughness, larger data scattering is reported using the nanoindenation approach. [118,119]

Recently, Yuya *et al* reported a technique for measuring Young's modulus of a single electrospun nanofiber using the resonant frequency shift resulting from the nanofiber, which is coupled with micro cantilevers. This approach gave a modulus of the as-spun PAN nanfiber (diameter ~200nm) of 26.8 GPa. [120] Using the same approach, Zussman *et al* measured the modulus of PAN-derived carbon nanofibers (diameter 100-200nm), which ranged from 53.5GPa to 69.8 GPa. [121] Similarly, Amrinder measured Young's modulus of suspended PMMA nanofibers (diameter 500-8000nm) from experimentally obtained resonant peaks and the values were found to agree with the literature values (2-3.5GPa). [64]

Mechanical properties of single polymer nanofibes were related to the polymer chain conformations within the fiber. Polymer chain conformation in nanofibers were examined using X-ray analysis and selected area electron diffractions. Arinstein et al argued that as the scale of supramolecular structures (orientated fragments of polymer chains) in the amorphous part of the nanofibers is comparable to the nanofiber diameter, a noticeable variation in mechanical properties can be expected. [122]Liu *et al* reported the confinement effect of fiber diameters on semicrytalline polymers. They report that the moduli of PEVA fibers increases with deceasing diameter, with the onset at ~10μm. [123] Zhang *et al* observed enhanced crystallinities within PLLA nanofibers (diameter 300-500nm) spun at elevated take-up velocities and they reported an optimum take-up velocity to achieve PLLA nanofibers of high tensile strength. [124] Campseo *et al* investigated the spatial variation of polymer density with an electrospun nanofiber using near field optical measurements. A dense internal core with higher Young's modulus was found to embed in a less dense shell, which has lower Young's modulus. [125]

By far, varied approaches have been developed to characterize single nanofibers. However, achieving solid boundary conditions for these nanofibers usually involves micromanipulation within SEM/TEM, which limits their application to conducive materials. A simple approach to prepare large amount of single polymeric nanofibers with solid boundary conditions is highly desirable. Also, an effective nanofiber deformation strategy with simple mechanic model would greatly facilitate the mechanical characterization process.

In this study, we report an integrated approach to conveniently deposit and mechanically characterize single polymer nanofibers based on a recently reported sequential STEP technique. The STEP technique provides unique control on nanofiber i) boundary conditions, ii) alignment, iii) diameter (sub 100nm to microns). By laterally deflecting the single suspended nanofibers, both Young's modulus and break strength of nanofibers were obtained. Polymer chain orientation was

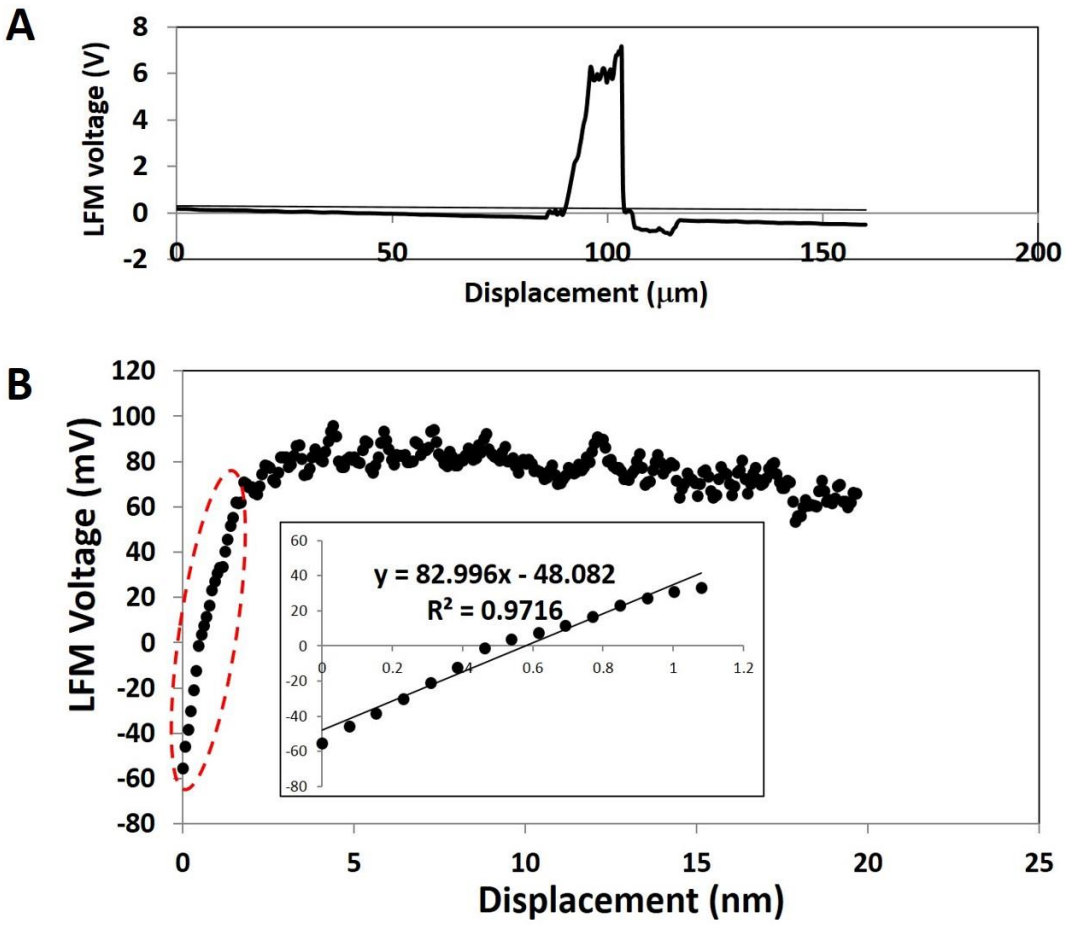

Figure 4.1 (A) A typical LFM voltage vs displacement curve, (B) a lateral friction curve from the slop of which, the sensitivity of cantilever was calculated. Insert in (B) demonstrates the determination of the curve slope.

investigated for both as spun and deformed nanofibers.

4.2 Experimental Section

Solution preparation: All chemicals were used as received without further purification. Polystyrene (PS) of several molecular weights (M_w) (860K, 1500K, and 2000K g.mol-1, Polymer Scientific, USA) were dissolved at room temperature in p-xylene at varying concentrations for one week prior to experiments.

Single suspended nanofiber deposition: A glass micropipettes with few micrometers in tip diameter are pulled in a pipette puller (P-1000, Sutter Instruments) and fixed perpendicular to a TEM grid which is moved by a motorized XYZ nano-positioner (VP24-XA, Newport). Polymer solution was pumped through the micropipettes and form a pendent solution droplet. By moving the micropipette across the TEM grid at a constant speed, solid polymer fibers were obtained on the TEM grid.

LFM Characterization: Force curves were obtained using a Dimension Icon Multimode AFM (Burker, CA, USA) operated in contact mode. DNP S-10 cantilevers (stiffness 0.17-0.7N/m) were utilized to deflect suspended fibers and the spring constants were calibrated every time before use. The lateral stiffness of the cantilever was determined from the normal stiffness and the cantilever geometry. [126] A silicon substrate was used to calibrate the sensitivity of the cantilevers.[127] The lateral displacement of the cantilever was controlled within the range 20μm-200μm. In the experiment, the signal obtained is LFM voltage (as shown in **Figure 4.1** (A)), which needs to be converted to forces using the following equation [126]:

$$\text{Force(N)} = \frac{\text{Voltage(V)}}{\text{Sensitivity(V/m)}} \times \text{cantilever lateral stiffness(N/m)} \qquad \text{Eq 4.1}$$

To obtain the sensitivity of the cantilever, the cantilever was engaged onto a flat silicon wafer surface and laterally moved to obtain a friction curve as shown in **Figure 4.1** (B). The cantilever

sensitivity was obtained from the slope of the friction curve. The lateral stiffness of the cantilever was obtained through [127,128]:

$$K_{lat} = \frac{2}{\left[6\cos^2\theta + 3(1+\nu)\sin^2\theta\right]}\left(\frac{L}{H}\right)^2 \times K_n \qquad \text{Eq 4.2}$$

Where K_{lat} is the lateral stiffness of the cantilever, ν is the Poisson's ratio of silicon 0.5, L ,θ and H are geometric dimensions of the cantilever, which are obtained from the manufacturers, K_n is the normal stiffness of the cantilever, which is obtained through thermal tuning.

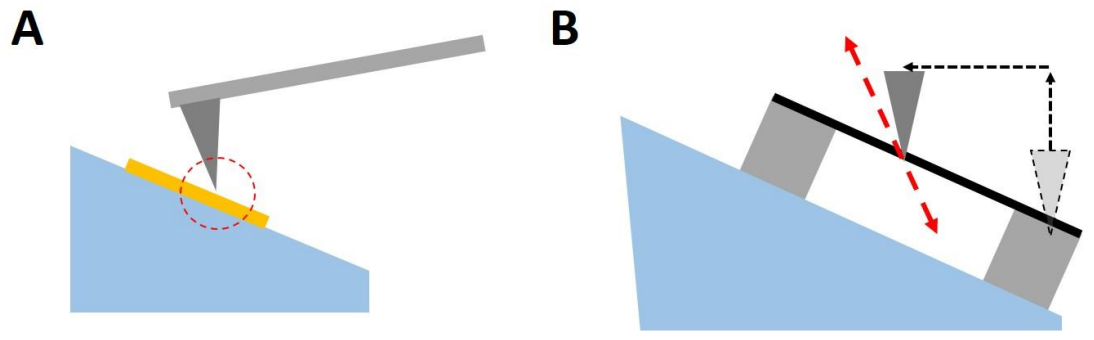

Figure 4.2 Schematic Illustration of LFM process. (A) A TEM grid sample was mounted on a tilted epoxy block. (B) An AFM cantilever was brought to the vicinity of the fiber and deflect the fiber in lateral direction.

To deflect the fibers using LFM, it is necessary to locate the positions of individual fibers on the TEM grid. TEM images were taken at low magnifications (1000-2000 magnification) to obtain the fiber position maps on the TEM grid. The TEM grid was then mounted on a titled epoxy block (the tilting angle is controlled ~30-45°) as shown in **Figure 4.2** (A). The AFM cantilever was first engaged on the TEM grid and then lifted for 5 microns using the step motor control and positioned near the middle of the fiber as shown in **Figure 4.2** (B). It is necessary to title the sample at angle and lifted the cantilever after engagement so that the cantilever will not make contact with the

TEM grids during lateral movement. By moving the cantilever laterally, LFM voltage vs displacement curves can be obtained as shown in **Figure 4.1** (A), which can be converted to force vs displacement curves using equation 4.1 and 4.2.

Three point bending test:

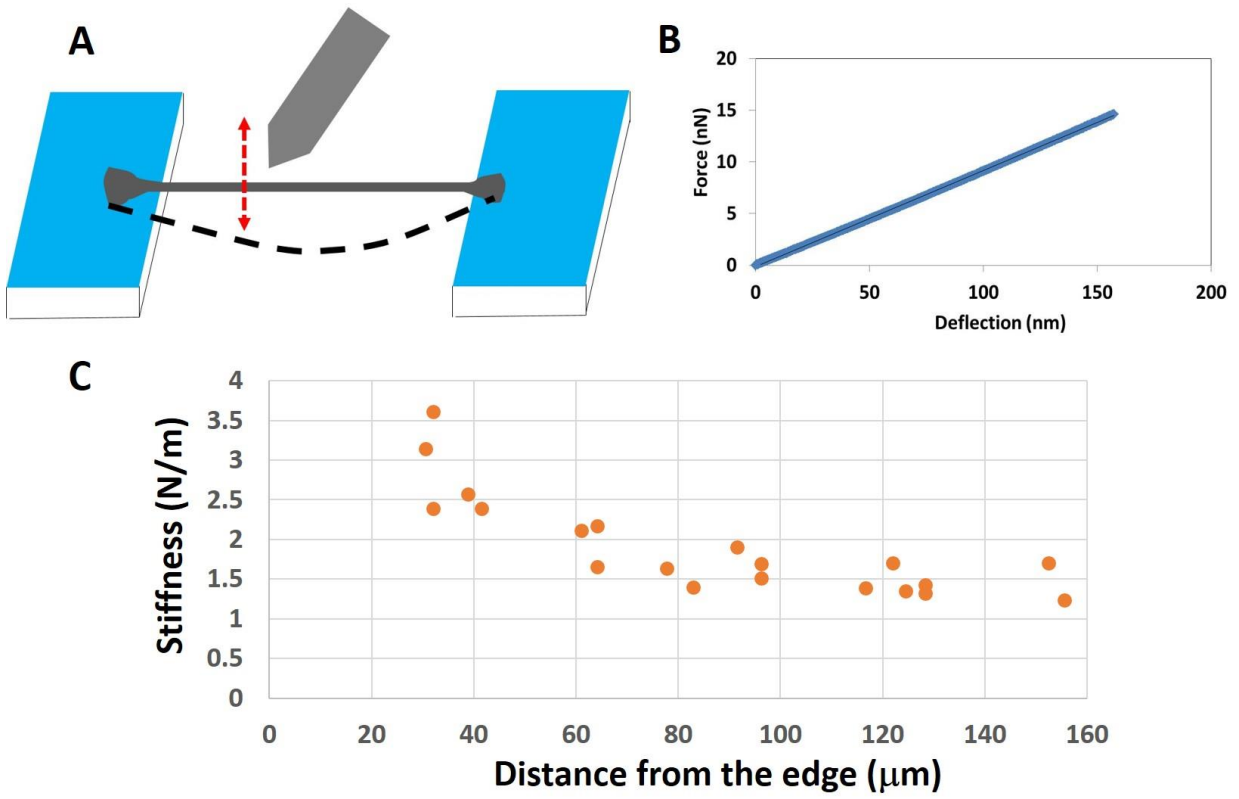

Figure 4.3 Three point bending test. (A) Schematic illustration of the three point bending test. (B) A typical force vs deflection curve obtained from three point bending test. (C) Stiffness variation along the length of a suspended nanofiber with diameter ~200nm.

In our study, three point bending tests were conducted to obtain the stiffness of suspended nanofibers. As shown in **Figure 4.3** (A), a tipless AFM cantilever with known stiffness (calibrated through thermal tuning) was engaged at the middle of a suspended nanofiber. The deflection of the fiber can be controlled through the ramping size (100 nm to 3.5 μm). Cantilever deflection vs

cantilever displacement curves can be obtained. The cantilever deflection can be converted to forces using the cantilever stiffness while the fiber deflection was obtained through:

$$\text{Fiber Deflection} = \text{Cantilever Displacement} - \text{Cantilever Deflection} \quad \text{Eq 4.3}$$

Therefore, typical force vs fiber deflection curves can be obtained as shown in **Figure 4.3** (B). By deflecting the fibers at different locations, the stiffness along the fiber can be obtained. **Figure 4.3** (C) demonstrate the stiffness variation along a 200nm diameter fiber with 320μm suspended length.

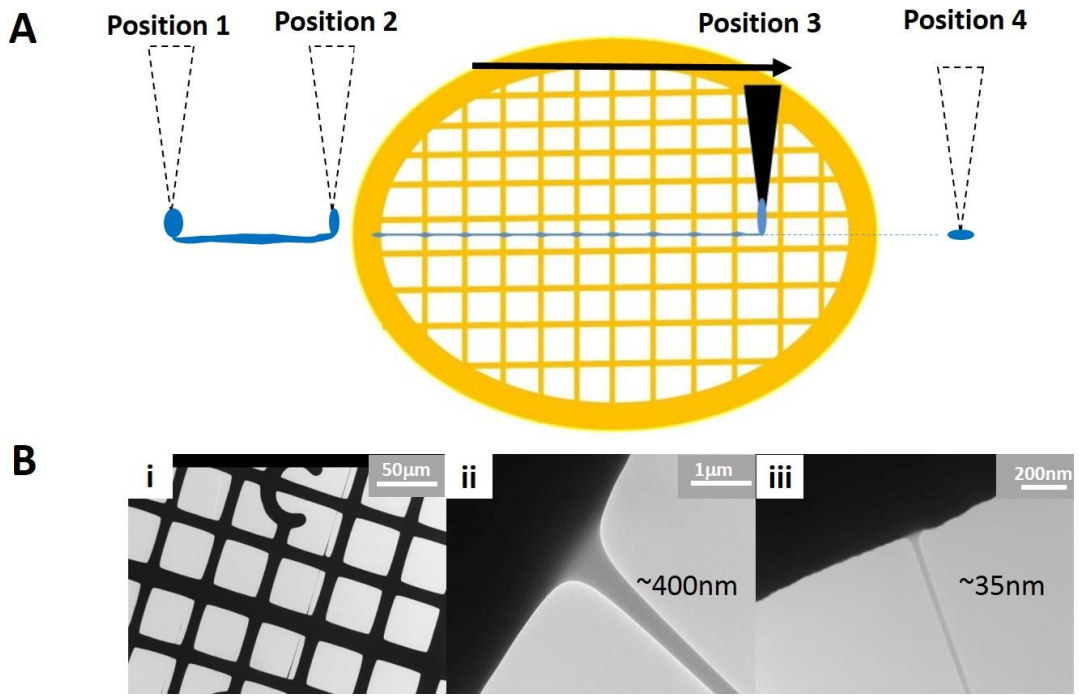

Figure 4.4 (A) Illustration of the single nanofiber deposition process, (B) TEM images of single suspended nanofibers on a TEM finder grid.

Electron Microscope: For SEM (Zeiss, Leo 1550) analysis, the samples were placed on gold-coated stubs and sputter coated. The morphology and selected area electron scattering (SAES) of single PS fibers were obtained using a TEM (Philips, EM420).

4.3 An Integrated Single Nanofiber Mechanical Characterization Approach

As shown in **Figure 4.4** (A), to deposit aligned single nanofibers, polymer solution is pumped

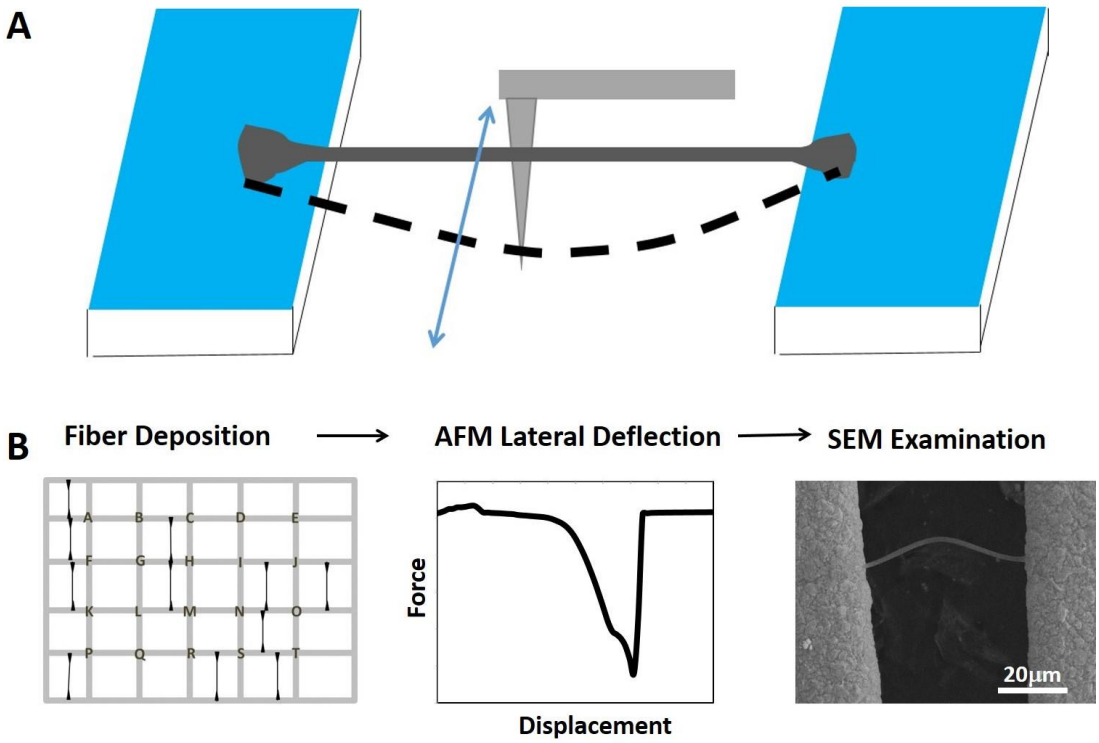

Figure 4.5 (A) Illustration of lateral deflection of a single suspended nanofiber using an AFM cantilever, (B) Illustration of the integrated approach for single nanofibers deposition and mechanical characterization.

through a glass pipette (inner diameter~20μm), which is fast moved across a TEM grid. As the polymer solution droplet makes contact with the TEM bars, aligned suspended nanofibers are formed. By repeating this process, multiple aligned fibers can be achieved on one TEM grid. Through manipulating the translation speed of the glass pipette and the polymer solution concentration, a wide spectrum of fiber diameters can be achieved as shown in **Figure 4.4** (B).

[44]Note that suspended nanofibers are found to physically stick to the TEM bars at both ends, thus establishing fixed-fixed boundary conditions.

In order to deform the single suspended nanofiber, an AFM cantilever with known stiffness is brought to the vicinity of the midpoint of nanofiber and then move laterally to deflect the nanofiber, as shown in **Figure 4.35** (A). Since there is no restriction in the lateral direction and the suspended fibers have fixed-fixed boundary conditions, large deformation can be achieved, which affords us the opportunity to detect the single nanofiber break strength. **Figure 4.5** (B) demonstrates the typical process of our integrated approach for single polymer nanofiber mechanical characterization: (i) multiple aligned suspended nanofibers were deposited on the TEM grid with fixed-fixed boundary conditions, (ii) the single suspended nanofiber was laterally deflected using an AFM cantilever and the force-deflection curve is recorded (iii) SEM images were taken after the fiber deflection to determine the fiber dimensions.

4.4 Modulus and Strength of Single Polymer Nanofibers

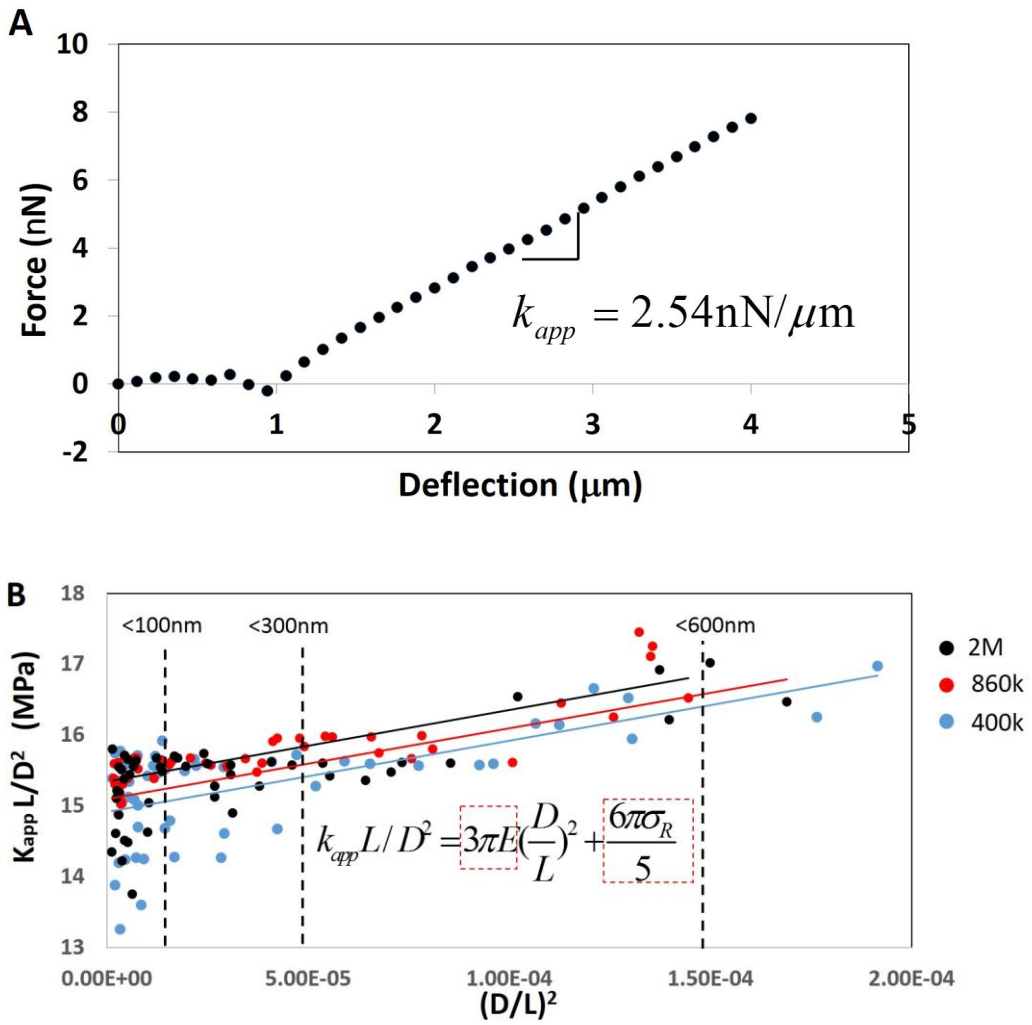

Figure 4.6 (A) Force deflection of a single PS nanofiber with diameter 90nm. (B) Product of apparent stiffness kapp and L/D^2 of PS nanofibers as a function of $(D/L)^2$.

Table 4.1 Mechanical Properties of single PS nanofibers

PS fibers	Slope (GPa)	Modulus (GPa)	Intercept (MPa)	Tensile Stress (MPa)
2M	10.07	**1.07**	14.91	**3.95**
860k	10.08	**1.07**	15.34	**4.07**
400k	10.03	**1.06**	15.08	**4.00**

Table 4.2 Stiffness of a 90nm diameter PS fiber

D (nm)	E(GPa)	L (μm)	k (N/m)	k/k_{app}	k_T (N/m)	k_T/k_{app}
90	1.07	60	4.94E-6	**0.002**	0.0025	**0.998**

By laterally deflecting a single suspended nanofiber, a force-deflection curve can be achieved, the

slope of which gives the apparent stiffness value k_{app} of the nanofiber, as shown in **Figure 4.6** (A). As proposed by Caenot *et al*, the apparent stiffness value of a nanofiber/nanowire can be expressed as[129]:

$$k_{app} = k + k_T = \frac{192EI}{L^3} + \frac{24T}{5L} \qquad \text{Eq 4.4}$$

Where k and k_T are contributions of structure stiffness and tension in the fiber respectively. We assume the tensile stress, which developed during manufacturing process, is uniformly distributed across the cross-section of the fiber and Eq 4.4 can be written as:

$$k_{app} L / D^2 = 3\pi E(\frac{D}{L})^2 + \frac{6\pi\sigma_R}{5} \qquad \text{Eq 4.5}$$

Where D is the fiber diameter and σ_R is the tensile stress. Reporting apparent modulus k_{app} multiplied by L / D^2 versus geometrical parameter $(\frac{D}{L})^2$ give a linear relation, as shown in **Figure 4.6** (B), which allows the determination of elastic modulus E and tensile stress σ_R (summarized in **Table 4.1**), as the slope is proportional to the elastic modulus E and non-zero intercept is proportional to the tensile stress σ_R. Note that the determined elastic modulus of PS nanofiber is 1.07GPa, which is comparable to the bulk material and more than 99% of the stiffness of the suspended fiber is dominated by the tensile force, as demonstrated in **Table 4.2**.

To detect the effect of reducing fiber diameter on fiber mechanical properties, the modulus and tensile stress of PS fibers were obtained at different diameter ranges as shown in in **Figure 4.7**. It

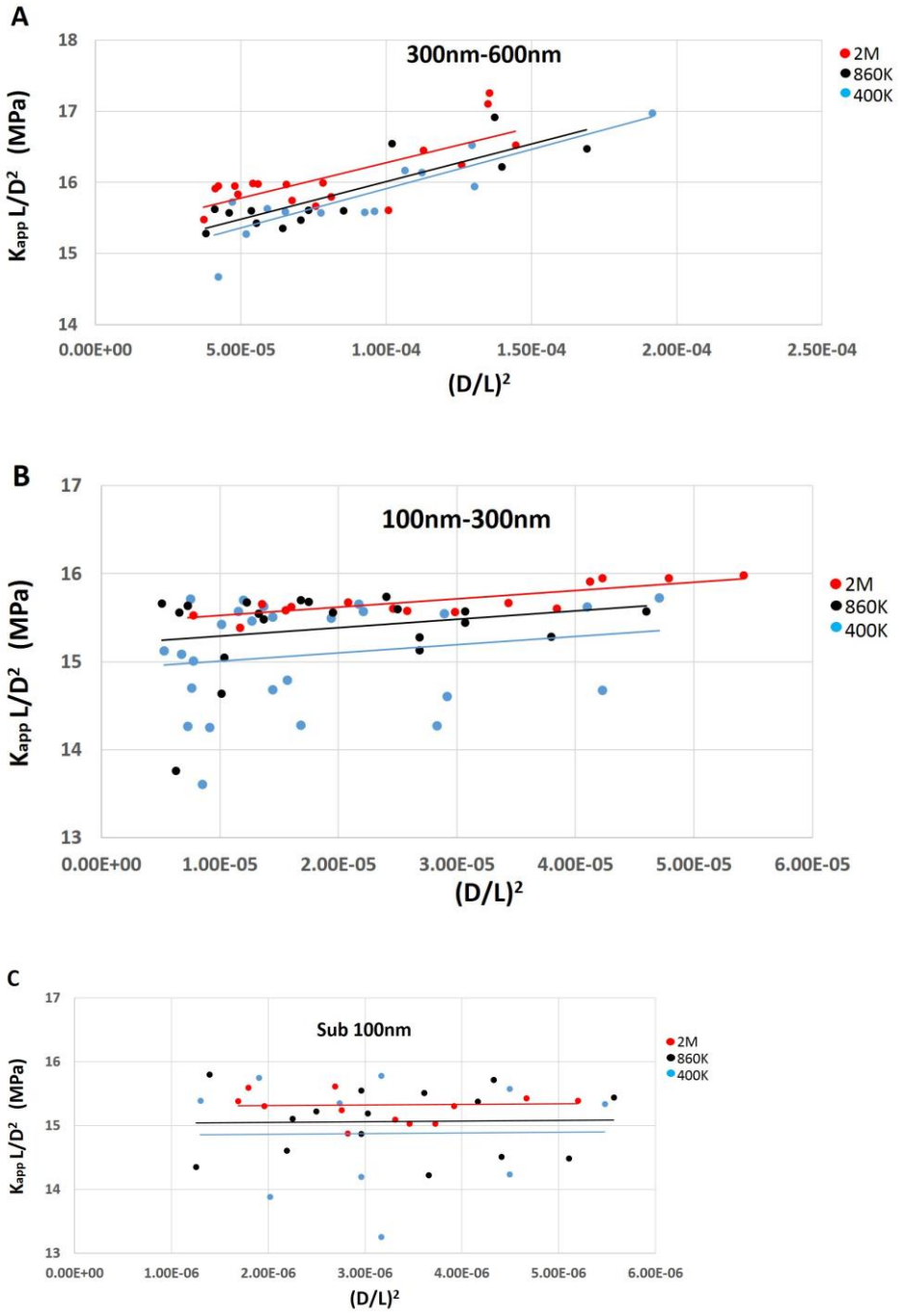

Figure 4.7 Product of apparent stiffness kapp and L/D^2 of PS nanofibers as a function of $(D/L)^2$ for different diameter ranges (A) 300-600nm, (B) 100-300nm, (C) sub 100nm.

was found that PS fibers demonstrate almost constant modulus (~1GPa) and tensile stress (~4MPa)

as fiber diameters reduce. (**Table 4.3** and **Table 4.4)**

Table 4.3 Summary of PS fiber modulus in different diameter ranges

Diameter Range	Modulus (GPa)		
	2M	860K	400K
300-600 nm	1.06	1.12	1.17
100-300 nm	1.01	1.00	1.00
Sub 100 nm	1.06	1.10	1.13

Table 4.4 Summary of PS fiber tensile stress in different diameter ranges

Diameter Range	Tensile Stress (MPa)		
	2M	860K	400K
300-600 nm	4.06	3.96	3.93
100-300 nm	4.10	4.03	3.96
Sub 100 nm	4.06	3.99	3.94

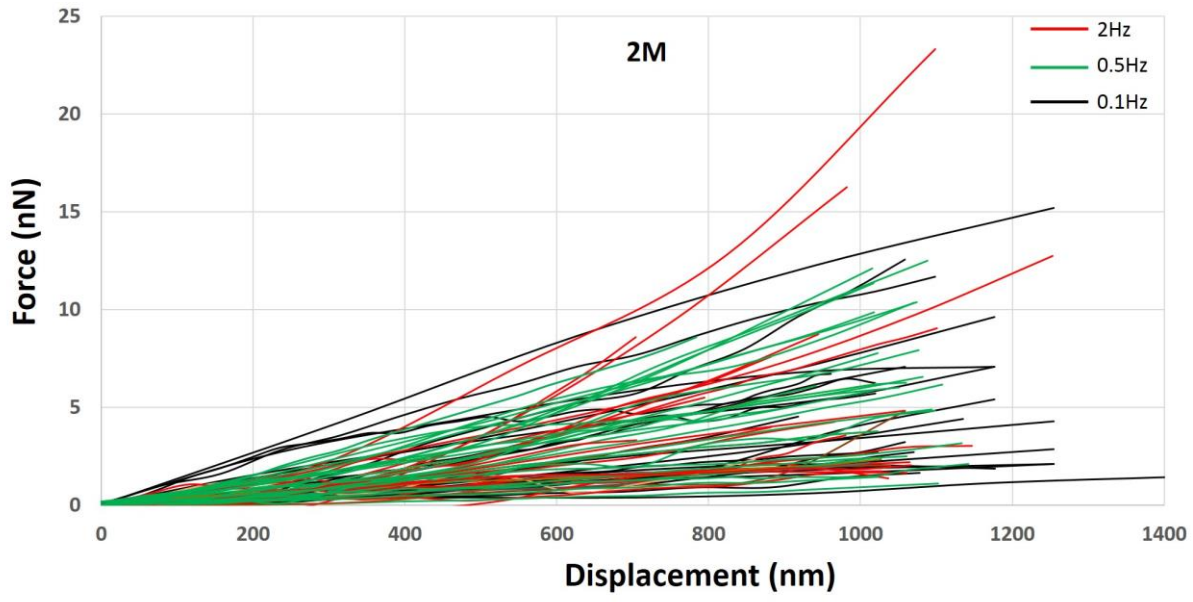

Figure 4.8 Force vs displacement curves for 2M PS fibers at different strain rate (2Hz, 0.5Hz and 0.1 Hz)

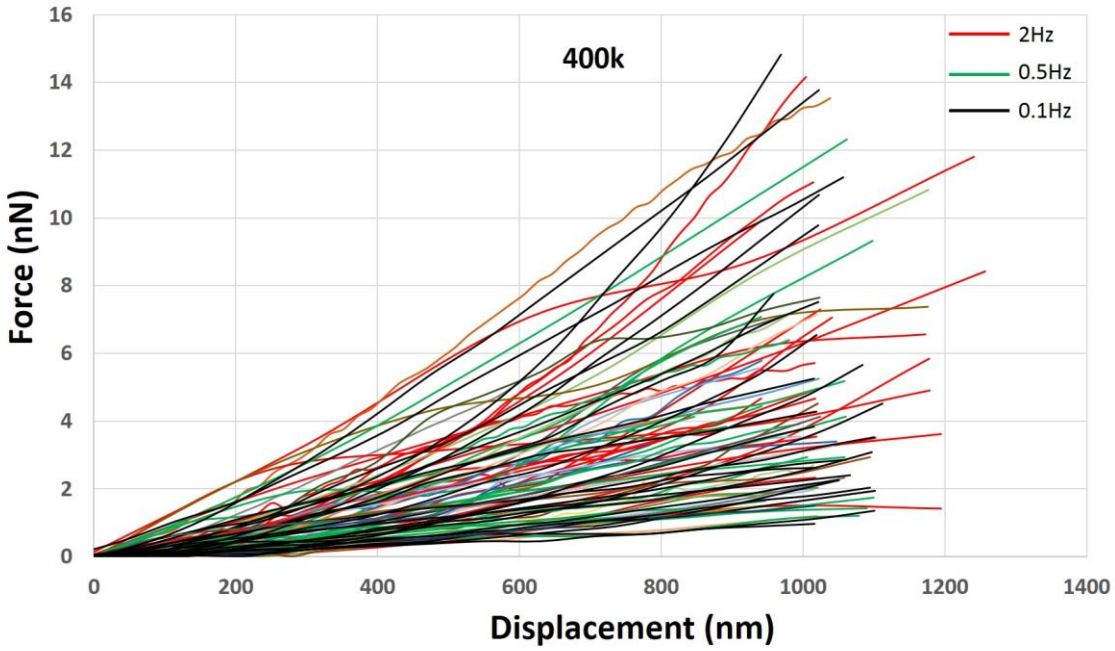

Figure 4.9 Force vs displacement curves for 400k PS fibers at different strain rate (2Hz, 0.5Hz and 0.1 Hz)

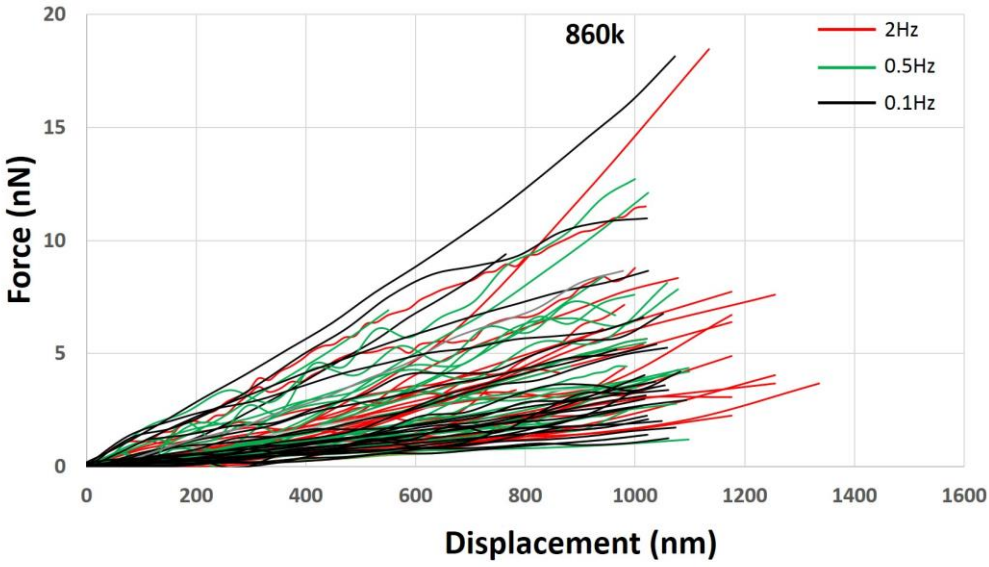

Figure 4.10 Force vs displacement curves for 860k PS fibers at different strain rate (2Hz, 0.5Hz and 0.1 Hz)

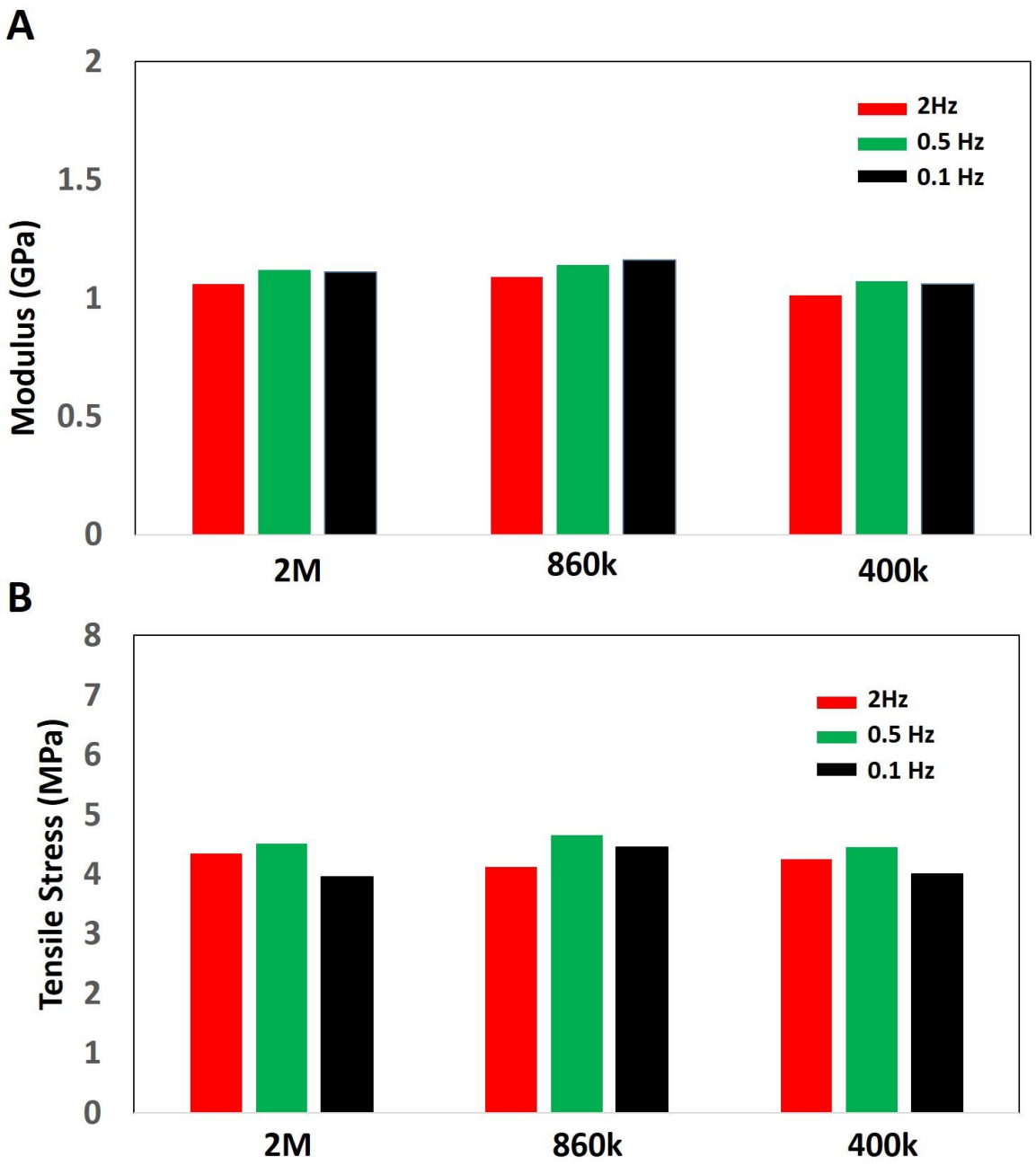

Figure 4.11 (A) PS (2M, 860k and 400k) fiber modulus obtained at different strain rate, (B) PS fiber tensile stress obtained at different strain rate.

As summarized in **Figure 4.8-Figure 4.10**, PS fibers made from different molecular weights (2M, 860k and 400k $gmol^{-1}$) were tested at varied strain rate (2Hz, 0.5Hz and 0.1Hz). As summarized in **Figure 4.11**, the strain rate and molecular weight variation does not produces significant difference in PS nanofiber modulus and tensile stress. (See **Appendix C**)

The tensile force in the fiber can be back calculated from the stiffness:

$$T = (k_{app} - \frac{192EI}{L^3})\frac{5L}{24} \qquad \text{Eq 4.6}$$

As summarized in **Figure 4.10**, for all three molecular weights of PS fibers in this study, the tensile force in the fiber scale with the fiber diameter, specifically, tension scales with the square of the

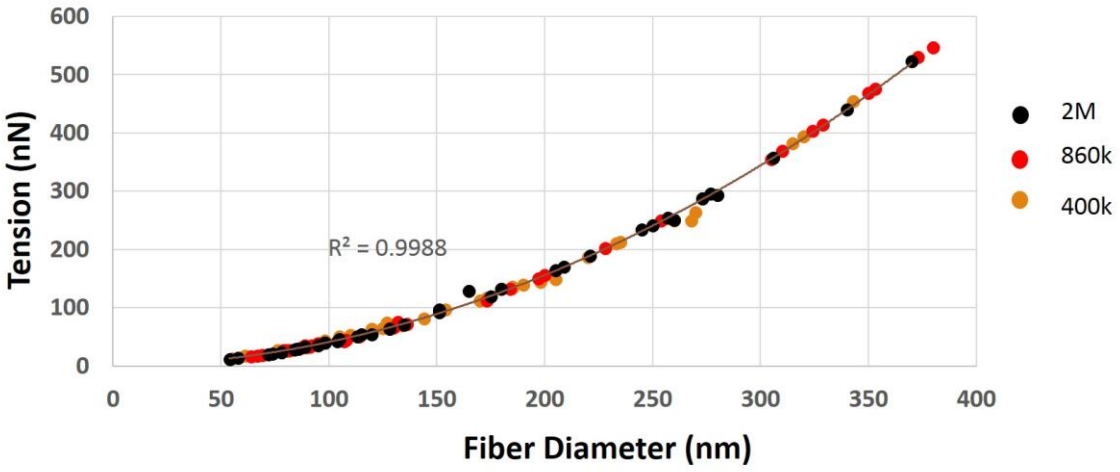

Figure 4.12 Tensile force vs Fiber diameter relation for PS fibers (2M, 860k and 400k).

fiber diameter. (see **Appendix D**) The tensile force is proportional to the cross-section area of the fiber, which verifies our assumption that the tensile stress is uniformly distributed across the cross section area of fiber.

To detect the polymer chain orientation in single polymer nanofibers, selected area electron scattering (SAES) were taken from the suspended PS fibers. (**Figure 4.13**) Isotropic scattering patterns were obtained for both 50nm and 500nm diameter PS fibers, indicates the absence of chain orientation in PS nanofibers.From the SAES patterns (**Figure 4.14**), we have short order distance of 1.4 Å and 2.5 Å , which are contributed by intramolecular correlations of polystyrene. [130,131] Polymer chain orientation along fiber axis have been reported for electrospun nanofibers. [29,132,133] In particular, as the fiber collecting speed increases (usually reported as the rotating speed of the collector), polymer chain are preferably oriented along fiber axis. The orientation mechanism is related to the shear stress experienced by the polymer chains as the solution jet elongates during the trajectory. [134,135] In our study, the translation speed of the glass pipette is in the range of 1-7mm/s, which is much slower than the reported fiber collecting speed (30-100m/s) in electrospinning. Thus, it is possible that the absence of chain orientation in PS fibers is related

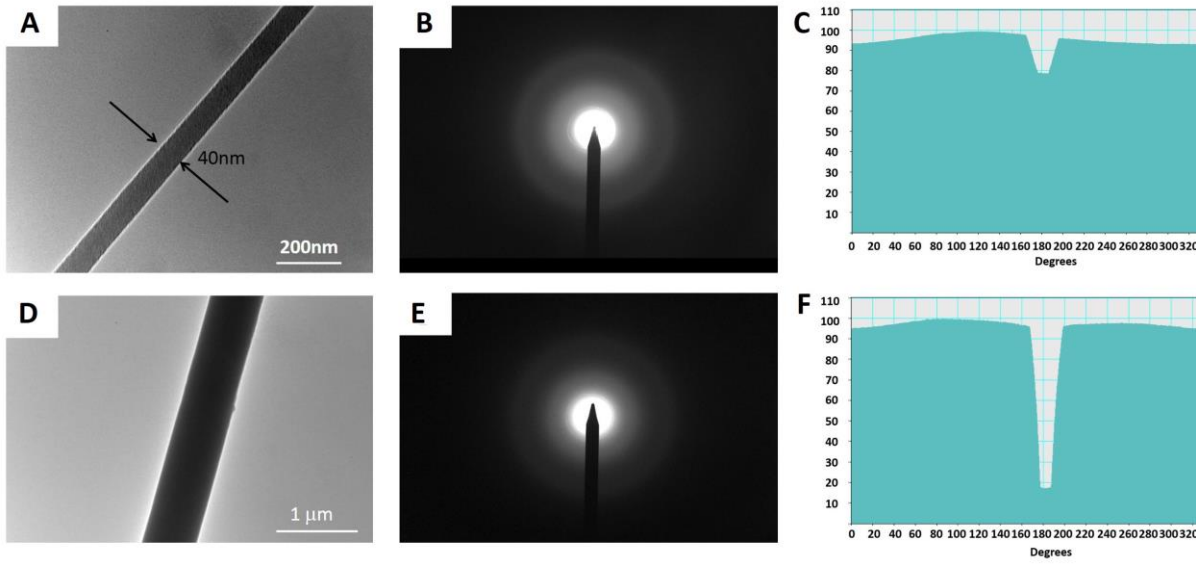

Figure 4.13 TEM images, SAES patterns and intensity versus azimuthal angles plot of a 40nm diameter PS fiber (A)-(C) and a 500nm diameter PS fiber (D)-(F).

to the slow elongation process, which leave the polymer chains enough time to relax during the elongation process.

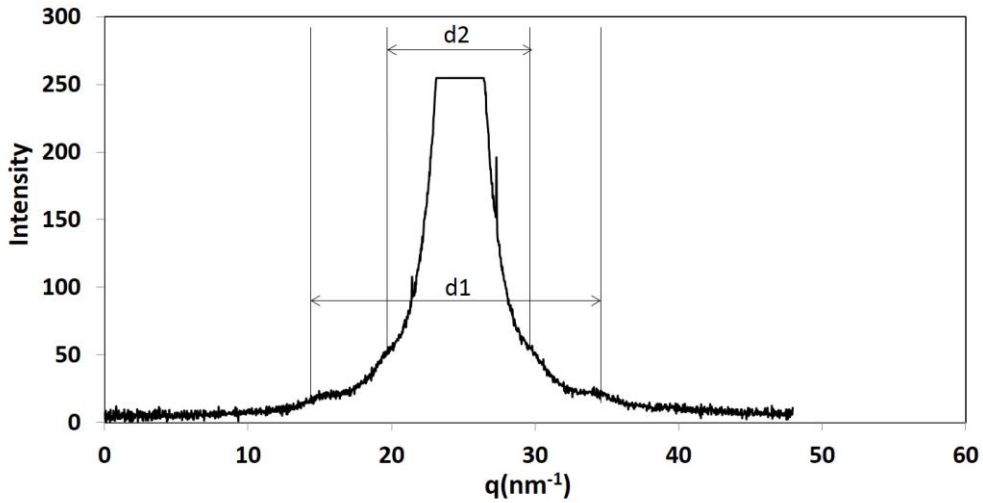

Figure 4.14 Electron Diffraction pattern of polystyrene. Short order distance d1=1.4A, d2=2.5 A .

In contrast with the as spun fibers, chain orientation was detected in deformed fibers. As shown in **Figure 4.15**, after a PS fiber was plastically deformed up to elongation ~ 60%, an obvious necking portion was observed. SAES patterns were taken along the fiber axis, revealing that chain orientation occurs in thick portion (orientation factor f = 0.28), transition portion (f = 0.33) and necking portion (f =0.68) respectively. Similar strain induced polymer chain orientation has been also been reported in bulk materials. [136,137]

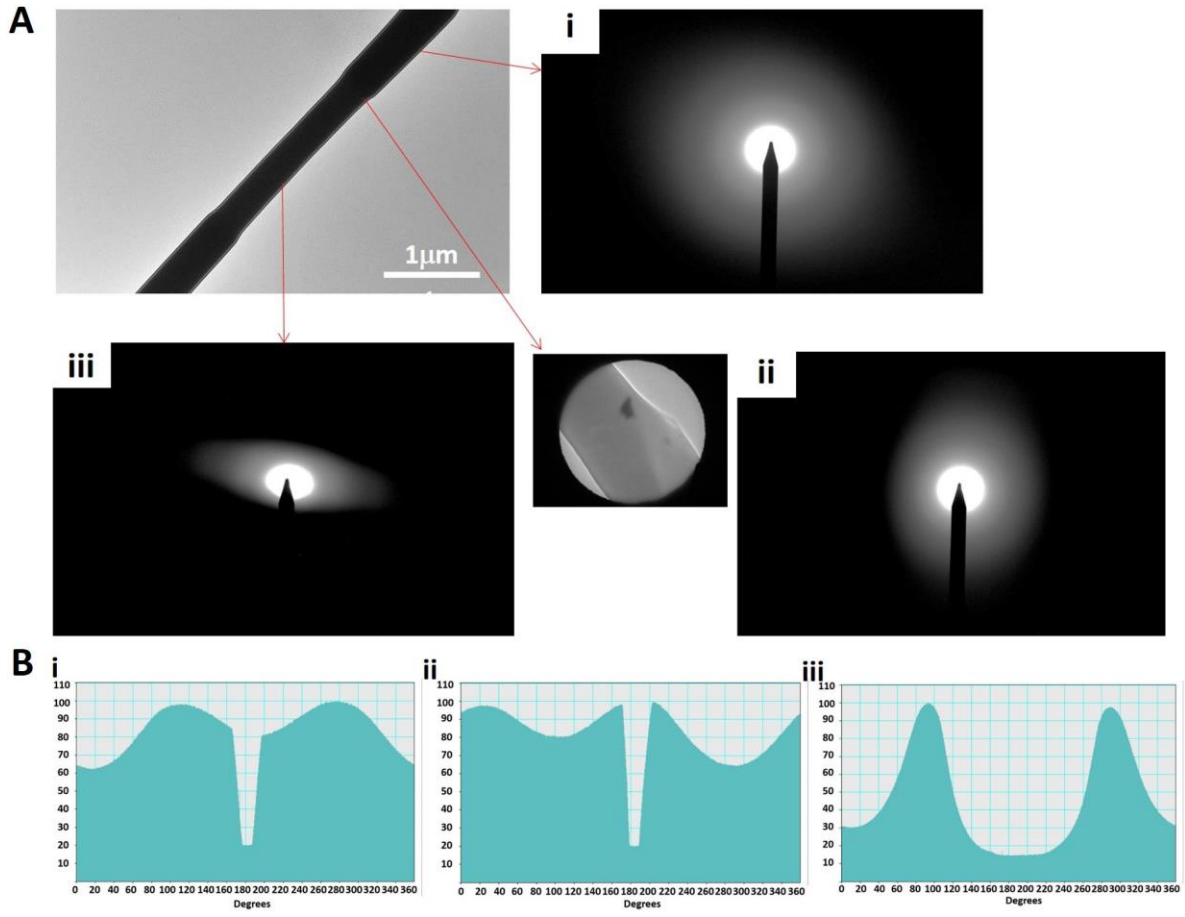

Figure 4.15 (A) TEM image of a plastically deformed fiber. Inserts i, ii, iii are SAES patterns taken on thick portion, transition portion and necking portion of the fiber respectively. (B)Intensity versus azimuthal angle plot for portion (i)-(iii) in (A).

On the other hand, less pronounced chain orientation was observed on nanofibers deformed to 20% elongation, as shown in **Figure 4.16**. The chain orientation factor f is in the range of 0.14 - 0.17. If a crystalline polymer instead of PS is drawn with the same method, highly oriented internal structures may be formed, which is a future work.

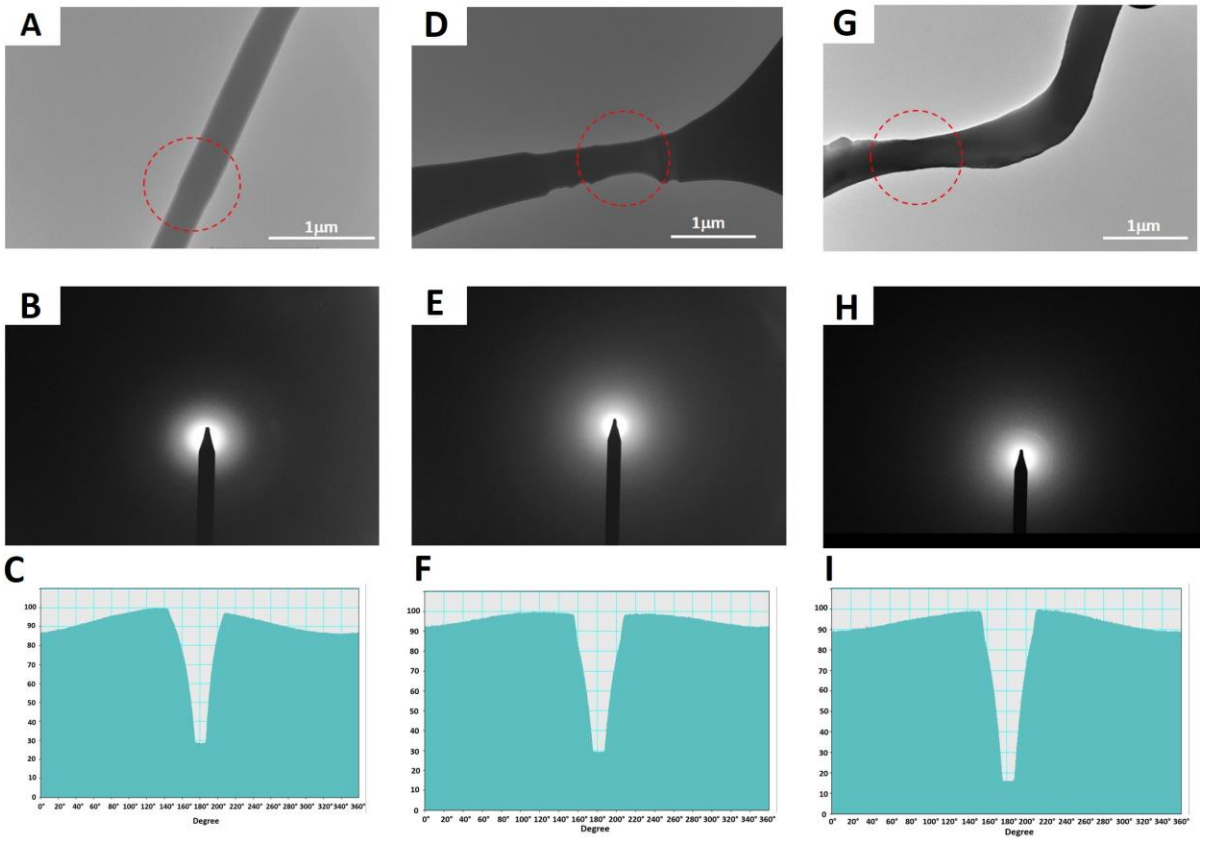

Figure 4.16 TEM images, SAES pattern and intensity versus azimuthal angles plots of deflected PS fibers (~20% elongation): (A)-(C) a deformed 2M PS fiber, chain orientation factor f =0.16, (D)-(F) a deformed 860k PS fiber, chain orientation factor f =0.14, (G)-(I) a deformed 400k PS fiber, chain orientation factor f =0.17.

Single Nanofiber strength was calculated based on the breaking force as shown in **Figure 4.15** (A) (B), using the equation:

$$\sigma_{break} = (\frac{F}{2\cos\theta}) / (\frac{\pi}{4} D^2) + \sigma_R \qquad \text{Eq 4.7}$$

As fiber diameters decrease from 150nm to 50nm, the break strength of single nanofiber demonstrates an increase of 300MPa, as shown in **Figure 4.17** (C). A similar trend of the strength enhancement with decreasing fiber diameter has been reported for gold nanowires. [138,139] Given the constant suspended length of the fiber (60□μm), the enhancement in break strength

could possibly be attributed to the reduction of the defects contained in the fiber. Note that there is no significant difference among PS nanofibers made from different molecular weights.

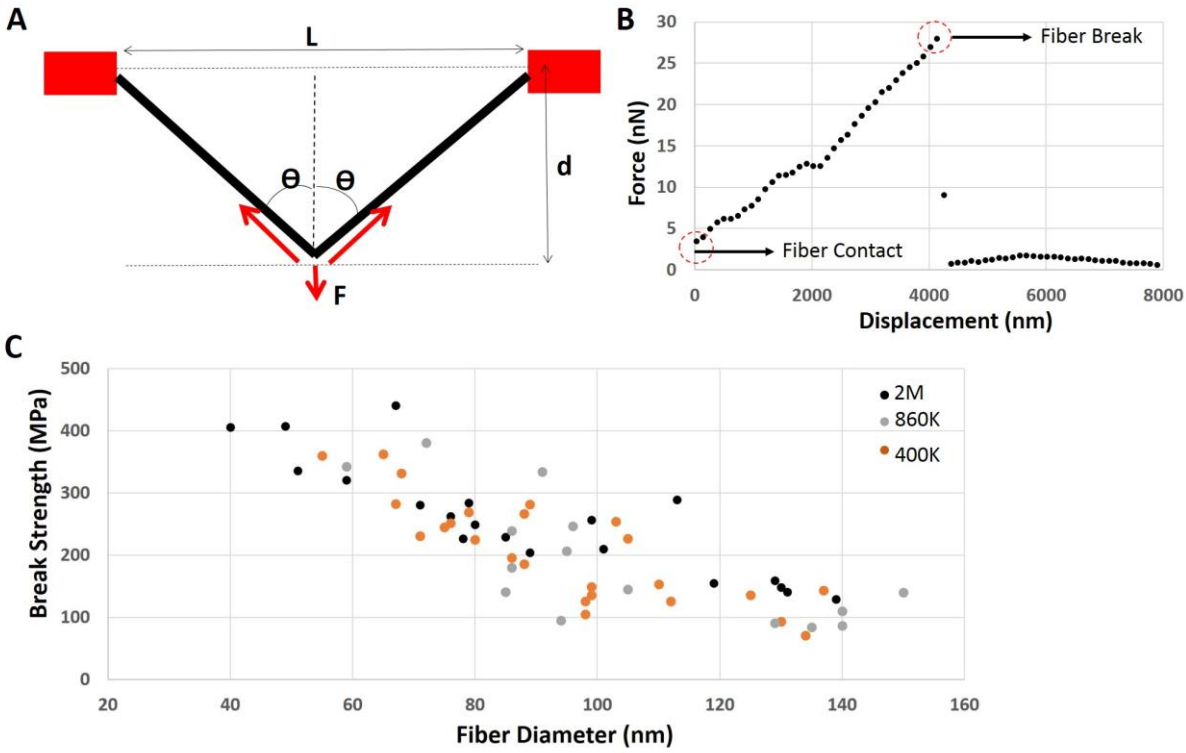

Figure 4.17 (A) Illustration of single nanofiber break by lateral deflection. (B) A force-displacement a single nanofiber break process. (C) Single fiber break strength as a function of fiber diameter.

The strength of a fiber is determined by the most severe flaw, so the fiber fails when the weakest point in the fiber fails. This behavior is usually modeled by a two-parameter Weibull distribution:

$$F(\sigma_f) = 1 - \exp[-(\frac{\sigma_f}{\sigma_0})^{\beta}] \qquad \text{Eq 4.8}$$

Here, σ_f is the fail strength of a nanofiber, $F(\sigma_f)$ is the probability of fail. The single fiber strength for 80-100nm diameter fibers and 500nm diameter fibers was summarized respectively in **Table 4.5** and **Table 4.6**. The Weibull distribution is depicted by two parameters: σ_0 (the characteristic strength) and β (the Weibull Modulus), both of which can be obtained from a linear regression as shown in **Figure 4.18** (A).

Table 4.5 Summarization of single PS fiber strength with diameter about 500nm.

No	Diameter (nm)	Strength (MPa)	No	Diameter (nm)	Strength (MPa)
1	474	12.6	12	470	19.2
2	498	13.1	13	476	19.9
3	597	14.1	14	472	21.1
4	527	14.3	15	533	21.7
5	507	16.9	16	590	22.5
6	544	17.2	17	486	24.3
7	585	17.3	18	482	25.8
8	540	17.4	19	479	27.7
9	492	18.5	20	464	29.4
10	509	18.6	21	580	17
11	510	19	22	485	24.1

Table 4.6 Summarization of single PS fiber strength with diameter ranging from 80-100nm.

No	Diameter (nm)	Strength (MPa)	No	Diameter (nm)	Strength (MPa)
1	94	95	13	80	225
2	98	105	14	105	227
3	98	126	15	85	229
4	99	136	16	86	239
5	85	141	17	96	247
6	105	145	18	80	249
7	86	180	19	103	254
8	88	186	20	79	269
9	86	196	21	89	282
10	89	204	22	79	284
11	95	207	23	91	334
12	101	210			

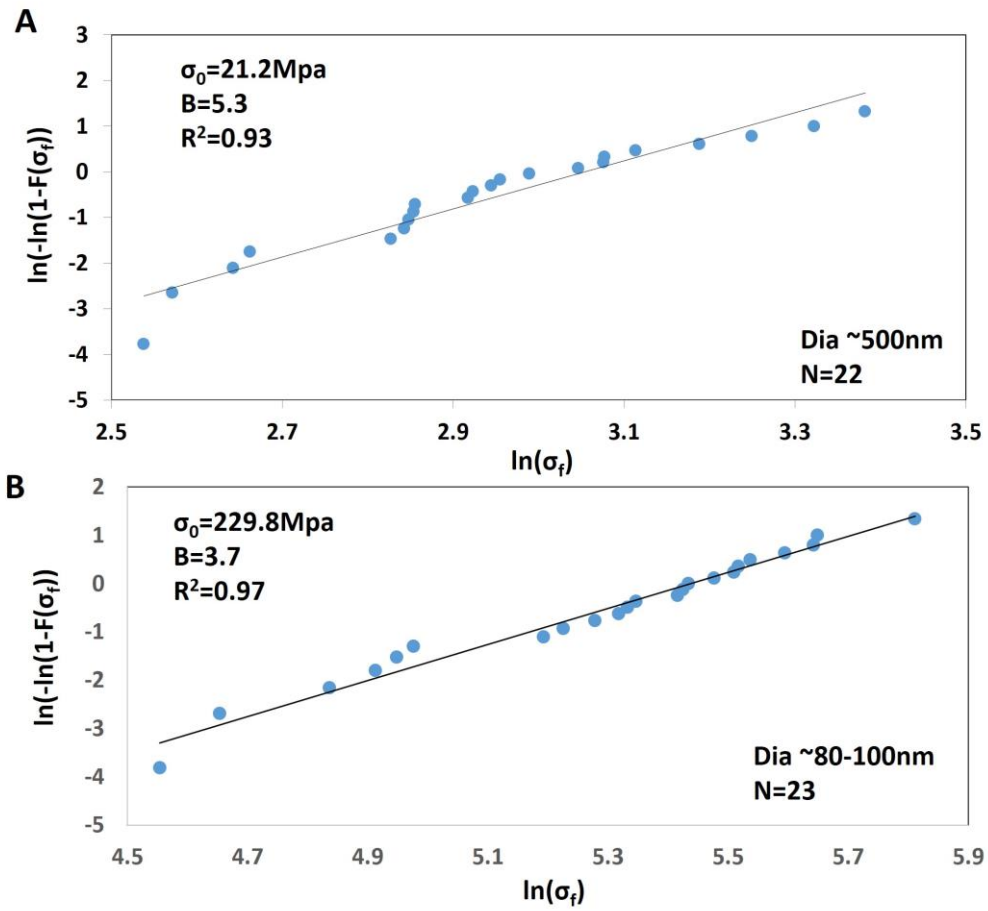

Figure 4.18 (A) Single fiber strength distribution for fibers with diameter about 500nm, (B) single fiber strength distribution for fiber with diameter in the range of 80-100nm.

The linearity of the plot demonstrates the validity of the Weibull model (confidence intervals R^2=0.93). The Weibull modulus β reflects the defects distribution within the fiber. Higher values of β indicates that defects are evenly distributed through the materials while low value of β indicates a diverse population of flaws in size and location. In our study, the Weibull modulus β (5.3 and 3.7) values is larger than reported values of electrospun nanofibers, [99,140] and comparable to carbon fibers. [141,142] The Weibull modulus indicates a relatively evenly

distributed flaws in the PS fiber, which can be attributed to the slow fiber drawing process and the resultant homogenously distributed molecular entanglement density in the PS nanofibers.

4.5 Nanofiber Yarn Strength Prediction

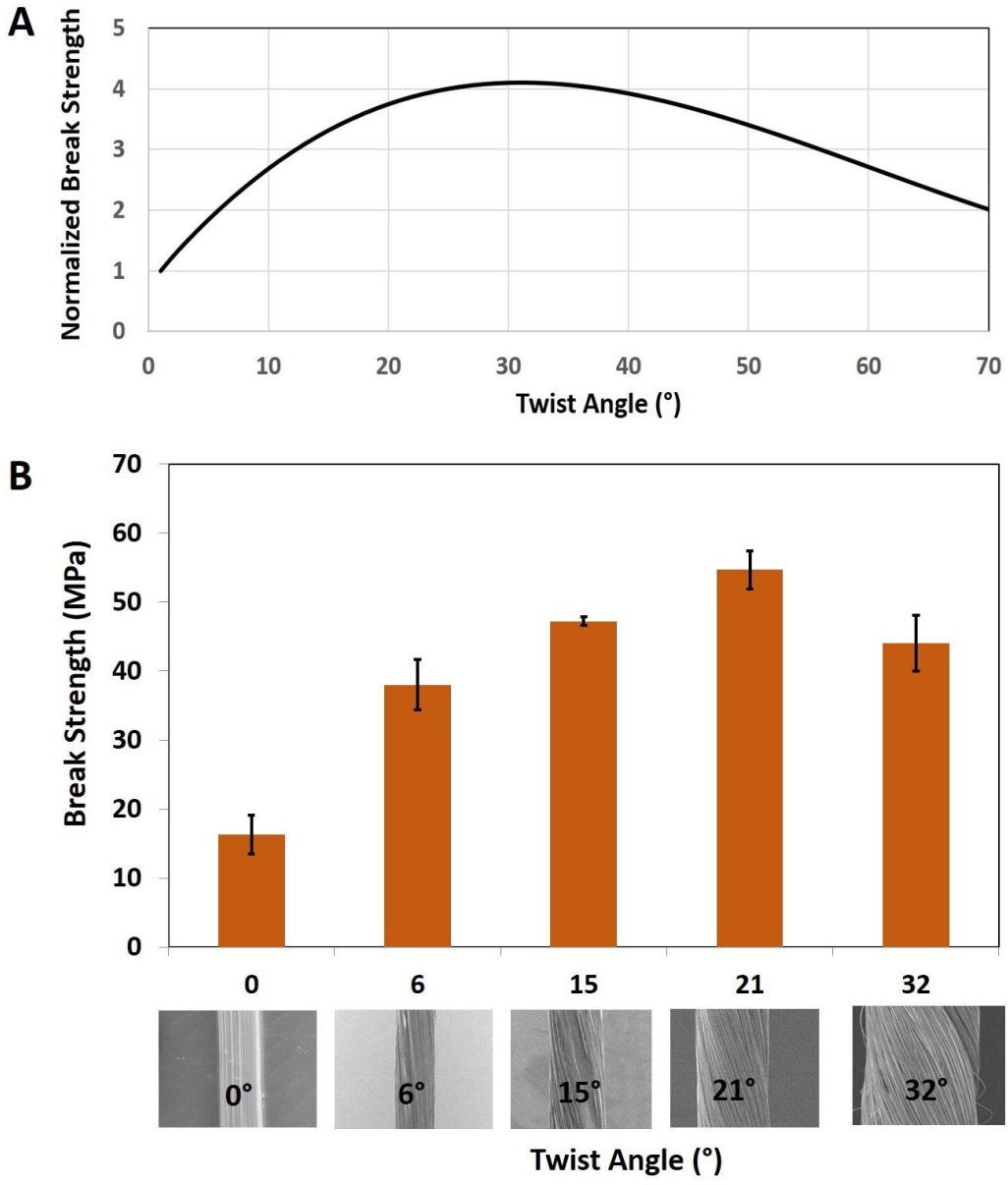

Figure 4.19 (A) Yarn strength as a function of twisting angle based on model calculation. Yarn strength is normalized to the bundle (twisting angle 0°). (B) Experimental results of yarn strength with different twisting levels.

In our study, 500nm diameter PS nanofibers were incorporated into yarns with exactly controlled twist angles. The yarn strength was predicted using an established model[143,144]:

$$\langle \sigma_y \rangle = \eta_q V_f (l_c \alpha \beta)^{-1/\beta} \exp(-1/\beta) \qquad \text{Eq 4.9}$$

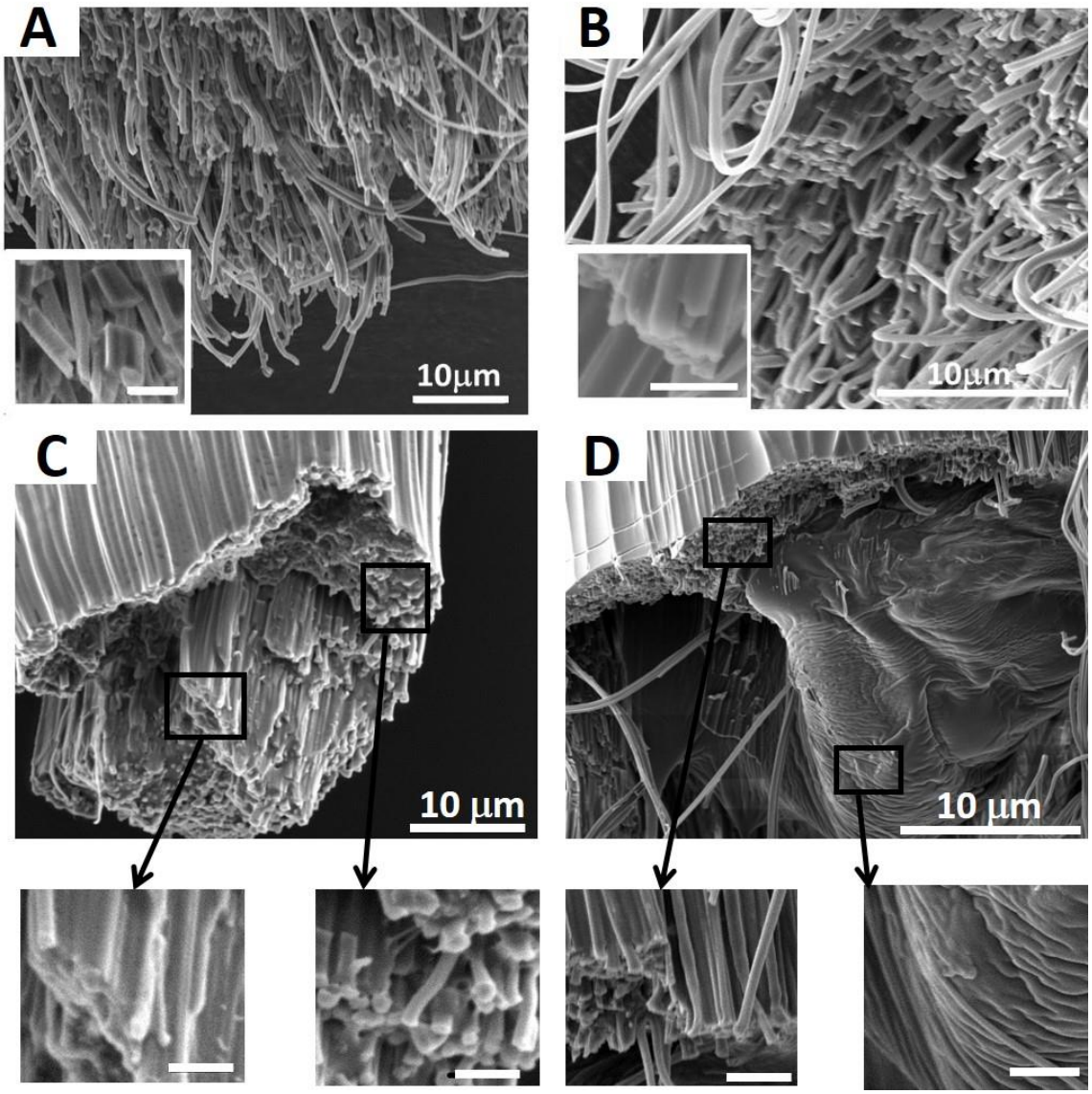

Figure 4.20 SEM images of cross-sections of (A) 6°, (B) 15°, (C)21° and (D) 32° yarns. Scale bars represent 2 μm in inserts.

Where $\langle \sigma_y \rangle$ is normalized yarn strength, η_q is the orientation factor of fibers in the yarn, V_f is the fiber volume fraction of the yarn, l_c is the critical fiber length which relate with fiber interactions within the yarn, and α, $ß$ are Weibull distribution parameters obtained from single fiber break experiments. Yarn twists provide increased inter-fiber friction, enhanced fiber volume fractions and decrease the overall orientation of the fibers. According to the perdition of this model, there is an optimal twisting angle (~30°) as shown in **Figure 4.19** (A), beyond which the yarn strength will decrease. However, the optimal twist angle turns out to be ~21° in experiment, as shown in **Figure 4.17** (B). SEM images of the yarn cross sections reveals that fibers at the center the yarn tends to fuse together under the lateral pressure in the yarn, which is scaled with the twisting level.(**Figure 4.20**). The significant fiber fusion at high twisting level (twist angle 21°and twist angle 32°) may leads to decreased yarn strength and account for the discrepancy between the prediction and the experiment results.

4.6 Conclusion

In conclusion**,** an integrated approach for single polymer nanofiber mechanical characterization has been developed, which offered a unique platform to investigate single nanofiber modulus and strength. Single PS fibers manufactured using the sequential STEP technique demonstrate comparable modulus with bulk material. Significantly increased strength with decreasing fiber diameters were observed. Macromolecule chain orientation was accompanied with large fiber deformation at high strain rate. The single nanofiber strength can be depicted by a two parameter Weibull distribution and used in yarn strength prediction.

Chapter 5 Biological Applications of Hierarchical Nanofiber Assemblies

5.1 Introduction

A large number of studies using flat or gel culture systems have highlighted the role of extrinsic biophysical cues from the surrounding extra-cellular matrix (ECM) on cellular interactions.[145,146] Topographic reactions of cells to micro-meter range features such as wells, islands, and pillars have been intensively investigated based on micro-patterned approaches.[147] It has been shown that cell shape, position and function can be regulated by attachment of cells on engineered substrates coated with different density of ECM.[148,149] However, cells require a full description of 3D nanofibrous ECM to maintain their phenotypic shape and establish behaviour patterns. Recently, electrospun nanofibrous scaffolds have been successfully produced from both synthetic and natural polymers with diameter ranging from nanometer to micrometers.[91,150] Cell studies on these scaffolds have revealed that cell attachment and spreading is affected by nanofiber diameter and scaffolds porosity.[151,152] However, the role of suspended fiber spacing, orientation and fiber stiffness in influencing cell behavior has yet to be demonstrated. Cells on suspended fibers react to mechanical cues by wrapping around the suspended fibers, which has been shown by us to elicit different cell behaviors.[14–16,153,3] Suspended cell-fiber culture systems afford a wide parametric investigation of the role of biophysical cues on cellular interactions. In this study, we present the development of hierarchical nanofiber assemblies as a platform technology to control cell attachment and spreading and investigate the “inside-out” cell forces.

5.2 Experimental Section

Cell culturing: STEP scaffolds were mounted on to glass-bottom six-well plates (MatTek Corp., Ashland, MA). Fiber scaffolds were sterilized by adding 2 ml 70% ethanol for 10 min, then coated in 2 $\mu g.ml^{-1}$fibronectin (Invitrogen, Carlsbad, CA).[15,16] C2C12 mouse myoblasts (American Type Culture Collection, Manassas, VA) were cultured in Dulbecco's Modified Eagle Medium (DMEM) supplemented with 10% fetal bovine serum (FBS) and 1% penicillin/streptomycin (HyClone Laboratories, Logan, UT). Cells were seeded onto the fiber scaffolds via 30 μl droplets at a concentration of 100,000 cells ml^{-1} and incubated at 37 °C and 5% CO_2. Cells were then given 2–6 h to attach onto the nanofibers. After 1 hour of seeding, 2 ml of medium was added to each well.

Fluorescence microscopy: C2C12 mouse myoblasts were stained for F-actin stress fibers, focal adhesions and the nucleus. Cells were fixed in 4% paraformaldehyde, permeabilized in a 0.1% Triton X100 solution and blocked in 10% goat serum. Primary goat antipaxillin antibodies (Invitrogen) were diluted 1:250 and incubated at 4C° for 1 h. Secondary goat anti-rabbit antibodies conjugated to Alexa Fluor 488 (Invitrogen) were then added along with a 1:100 dilution of rhodamine phalloidin (Santa Cruz Biotechnology, Santa Cruz, CA) and placed at room temperature for 45 min and protected from light. DAPI counterstaining was performed by adding 300 nM DAPI (Invitrogen) for 5 min. The substrates were then rinsed with PBS and observed using Zeiss microscope. Fiber scaffolds were kept hydrated in 1 ml phosphate buffered saline (PBS) during imaging.

Caspase-3/7 studies: In our experiment, cell apoptosis is induced by altering the ambient CO2 concentration from 5% to 0%, which resulted in media pH 8.4. Using this approach, MSCs are subjected to alkaline stress, which triggers a caspase dependent apoptotic pathway. To characterize caspase-3/7 activities, MSCs were stained by Caspase-3/7 Green Detection Reagent (Life Technologies, Grand Island, NY) at 2.5 ml/ml concentration for 30 minutes. Apoptotic cells with activated caspase-3/7 will have bright green nuclei, while cells without activated caspase 3/7 will have minimal fluorescence signal.

Statistical Methods: Statistical analysis and graphing were performed using GraphPad software. One way ANOVA testing with Tukey post testing comparing all pairs of data sets was performed. Column graphs are presented with standard error bars.

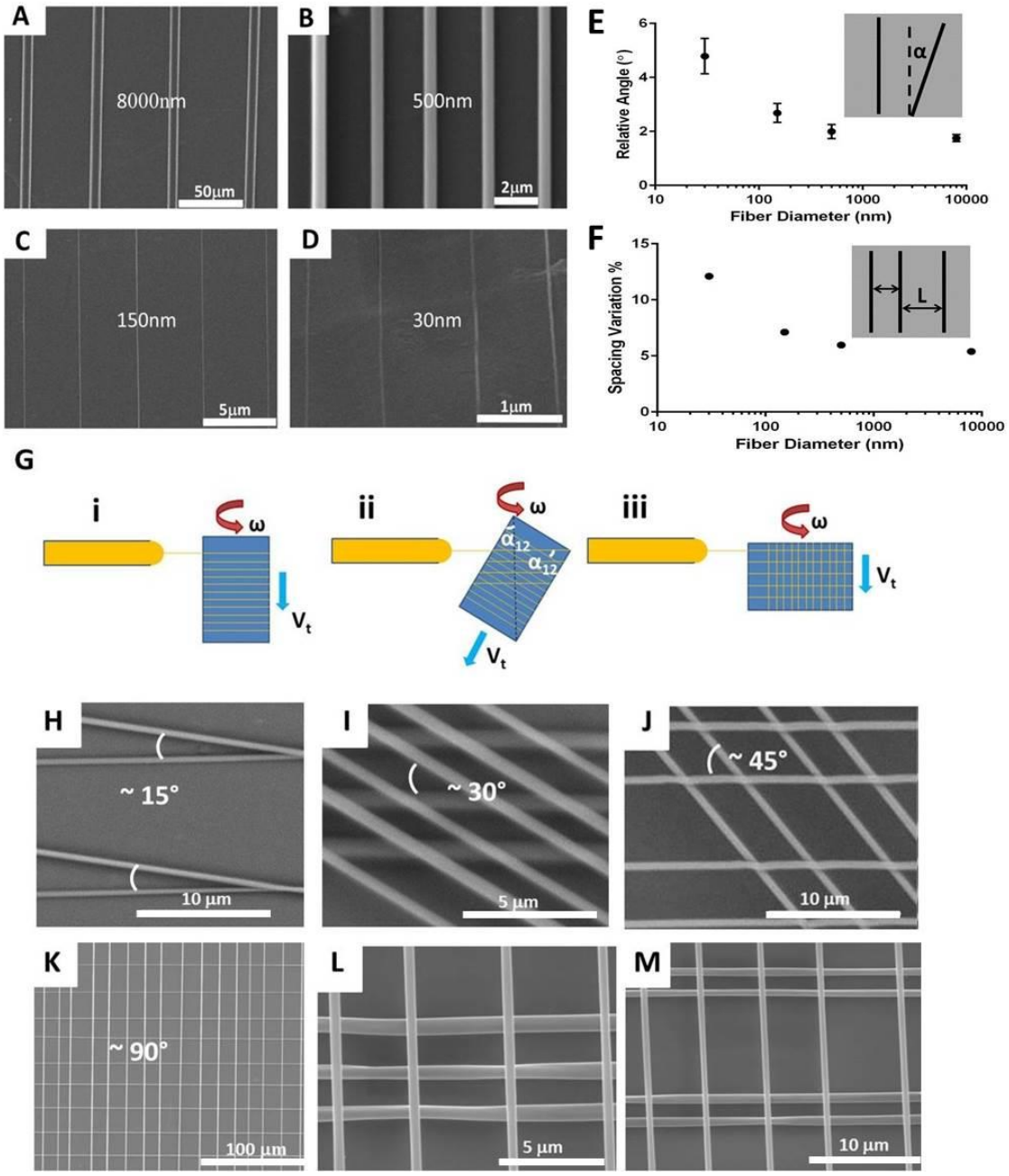

Figure 5.1 STEP capability in achieving control in single and double layer structures. (A-D) Arrays of 8000, 500, 150 and 30nm diameter PS fibers, (E) relative angles between adjacent fibers, (F) fiber spacing variation. Each data point in (E) and (F) is averaged averaged over 30 measurements, **(**G) (i-iii) schematic illustrations of achieving interlayer angle (α_{12}) in double layer structures, (H-J) SEM images of PS double layer structures with interlayer angle 15°,30°and 45° respectively, (K-M) orthogonally deposited PS double layer structures with unit cell size of 16×16 µm^2, 5×2 µm^2 and alternating 5×2 µm^2 and 5×10 µm^2. Wang et al, Langmuir, 2014, 30. Used with permission of American Chemical Society, 2015.

5.3 Hierarchical Nanofiber Assemblies as Biological Scaffolds

The fiber spacing is controlled by adjusting the translation speed according to

$$V_t = d \times RPS + L \times (RPS - 1) \qquad \text{Eq. 5.1}$$

Where V_t and RPS are the translation and rotation speed of the substrate, d is the fiber diameter and L is the fiber spacing. As shown in **Figure 5.1** (A)-(D), for both micro and nanofibers the inter-fiber spacing can be accurately controlled. The relative angels between adjacent fibers and spacing variation are well controlled (**Figure 5.1** (E) and (F)).

Double-layer structures were obtained by depositing fiber arrays on the previously deposited layer. Angles between two layers can be altered from 0° to 90° by rotating the substrate as shown in **Figure 5.1** (G) i-iii, which, when coupled with the ability to control spacing between consecutive fibers, enables a bottom-up assembly environment with fibers serving as 1D building blocks. As shown in **Figure 5.1** (H-K), PS nanofibers were deposited in double layer configurations and the angle between two layers (α_{12}) varied from 15° to 30°, 45° and 90°. By adjusting V_t in both directions, unit cell size was varied from 16×16 μm^2 (Figure 2(K)) to 5×2 μm^2 (**Figure 5.1**(L)) and alternating 5×2 μm^2 and 5×10 μm^2 unit cells within the same architecture (**Figure 5.1** (M)).

Using STEP, there is potentially no limitation on the numbers of layers that can be stacked on top of each other and the architectures of each layer (fiber material, diameter and conformation) can be customized as required. However, not unique to only STEP, but also to other fiber manufacturing platforms, challenges in deposition of fragile nanoscale fibers of substantial lengths at sub-micron spacing will need to be overcome to realize a complete hierarchical assembly design space.

For tissue engineering applications, such as organ regeneration and wound healing, it is highly desirable to control both cell densities and cell spread areas.[154] To achieve this goal, hierarchical nanofiber assemblies with varied porosities were prepared. As shown in **Figure 5.2** (A) and (B), spacing between PS supporting fibers (diameter~ 5 μm) were maintained at 80 μm while 4 different conformations of PS nanofibers (diameter~300 nm) were incorporated into these structures, including single layer (0°) with small and large fiber spacing (SS and SL), double layer (90°) with small and large spacing (DS and DL), with small and large spacing to be ~5 and 20 μm respectively. **Figure 5.2** (C) and (E) demonstrate that as pore size reduces in the architecture, more cells were observed to attach (cell density increased from ~14000/cm^2 to ~56000/cm^2), allowing cell density to be effectively regulated by the pore size. On the other hand, with pore size becoming smaller, more nanofibers were incorporated into the scaffolds, which increase cell-fiber assembly contact points, thus directly affecting focal adhesion arrangement. In our study, the C2C12 mouse myoblast spread area on suspended nanofibers was found to be less than 800 μm^2 (**Figure 5.2** (F)), which is smaller than the values reported by flat substrate studies (>1000 μm^2).[146,155] Note that suspended nanofibers used in this study are more compliant compared with flat glass or plastic surfaces, thus, our results support the concept that cells respond to increased compliance by reducing spread areas.[156] More importantly, it was found that crisscross (DL and DS) nanofiber scaffolds significantly enhanced the cell spreading (cell spread area ~700 μm^2) compared to the single layer (SL and SS) scaffolds (cell spread area ~400μm^2), as shown in **Figure 5.2** (D) and (F). This observation indicates that cell spread area can be adjusted by design of the scaffold architectures.

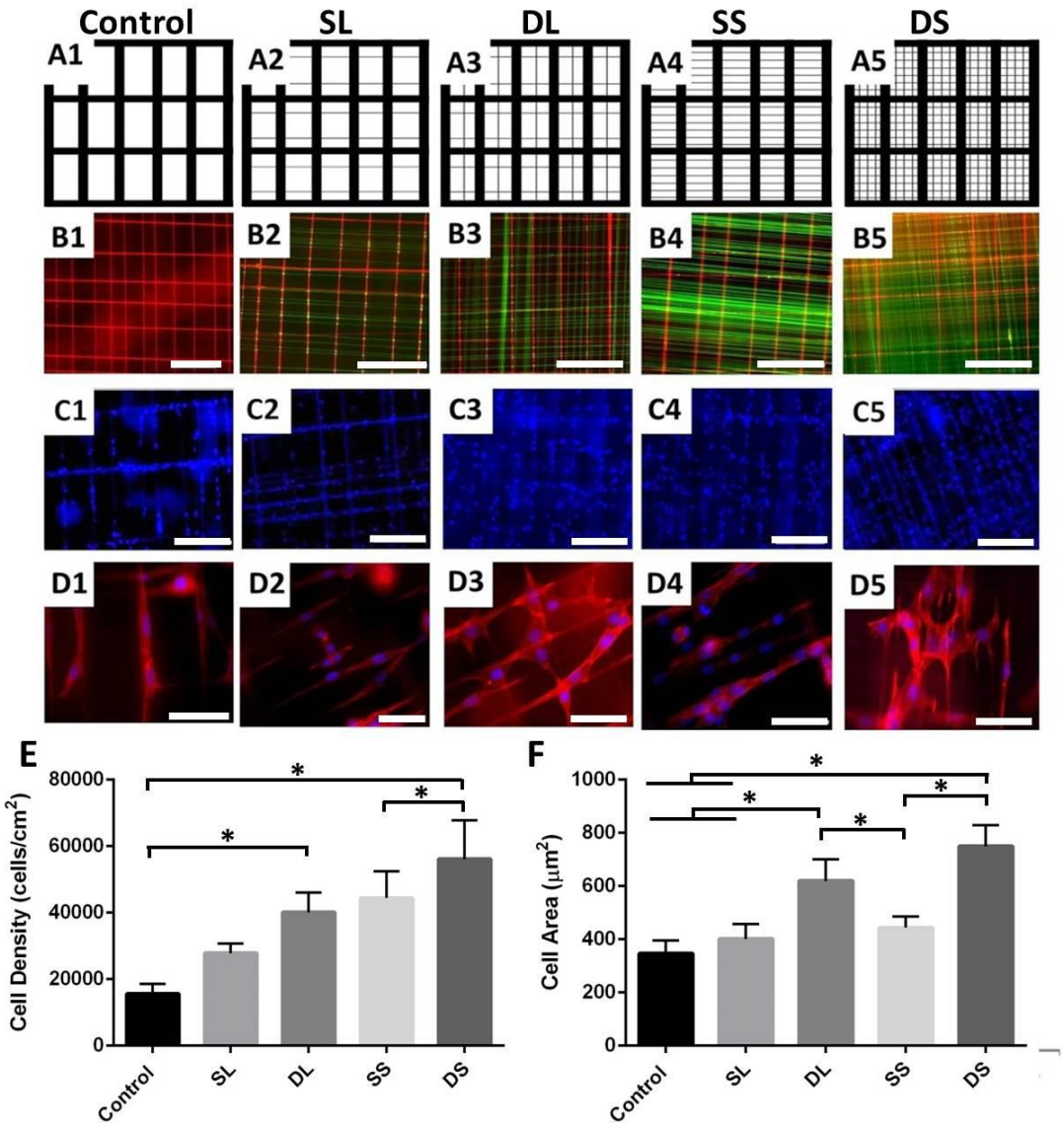

Figure 5.2 (A1-A5) Schematic illustration of varied hierarchical architectures: (A1) control, (A2) control supported single layer nanofiber with large spacing (SL), (A3) control supported double layer with large spacing (DL), (A4) control supported single layer with small spacing (SS), (A5) control supported double layer with small spacing (DS), (B1-B5) fluorescent images of control, SL,DL, SS,DS respectively with microscale fibers stained in red and nanoscale fibers stained in green, (C-D) fluorescent images of C2C12 mouse myoblasts, showing (C1-C5) nucleus (blue), (D1-D5) F-actin (red) attached to control, SL, DL, SS, DS structures respectively,(E-F) cell density and cell area on different hierarchical architectures ±SE. * shows statistical significance (for cell density $P<0.05$, n=60/category, for cell spread area $P<0.01$, n=60/category). Scale bars represent 50 μm in panel B-C and 20 μm in panel D. Wang et al, Langmuir, 2014, 30. Used with permission of American Chemical Society, 2015.

5.4 Cell Force Estimation Based on Nanofiber Nets

Stem cells possess the unique ability to self-renew and differentiate into a number of committed lineages. [157–160] Consequently, they have become a tremendously impactful resource for regeneration of aged, injured and diseased tissues. Mesenchymal stem cells (MSCs) has wide lineage portfolio and inherently contains the ability to specialize into different cell types such as

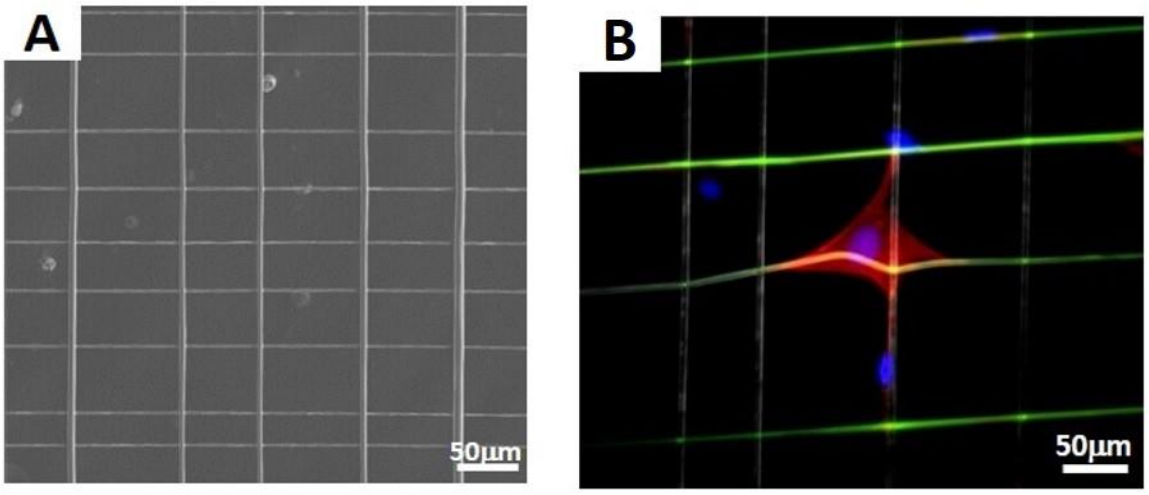

Figure 5.3 (A) A SEM image of fused nanofiber networks, (B) a florescent image showing the nanofibers is deflected by a single cell.

myoblasts, chondrocytes, osteoblasts, and adipocytes in response to external chemical and physical cues.[161–164] Breakthroughs in the past decade have highlighted the role of physical cues on MSCs.[165–167] Pioneering work by Engler and Discher demonstrated that in the absence of chemical cues, matrix stiffness (Pa) could present strong enough influence to drive MSCs specification, with soft surfaces (<1 kPa) producing neurons, medium stiffness surfaces (~10 kPa) producing muscle, and stiff surfaces (>100 kPa) producing bone.[168] To sense the biophysical environment, cells need to generate forces to deform the extracellular matrix (ECM). Cellular forces in nature are ubiquitous and contribute directly to cell behavior and fate.

Forces exerted by single cells can range from pico Newtons to micro Newtons.[169–171] The prevailing approach for measuring cellular forces involves placing them on substrates that contain deformable objects.[172–174] As long as the deformation can be reliably measured, forces can be back-calculated. This approach has taken on several different forms in recent years, including traction force gels and micropillar arrays. Thin polymer gels will wrinkle when cells exert forces on the surface during cell migration.[175–177] Resolution can be improved by embedding fluorescently-traceable microparticles into the gels which are displaced when the cell deforms the gel surface.[178,179] Micropillar arrays have also become a widely-used method of measuring cell contractile forces. Cells seeded on these substrates form adhesions at the tops of several pillars and deflect them as they generate migration/contraction forces.[180,181] Pillar height and

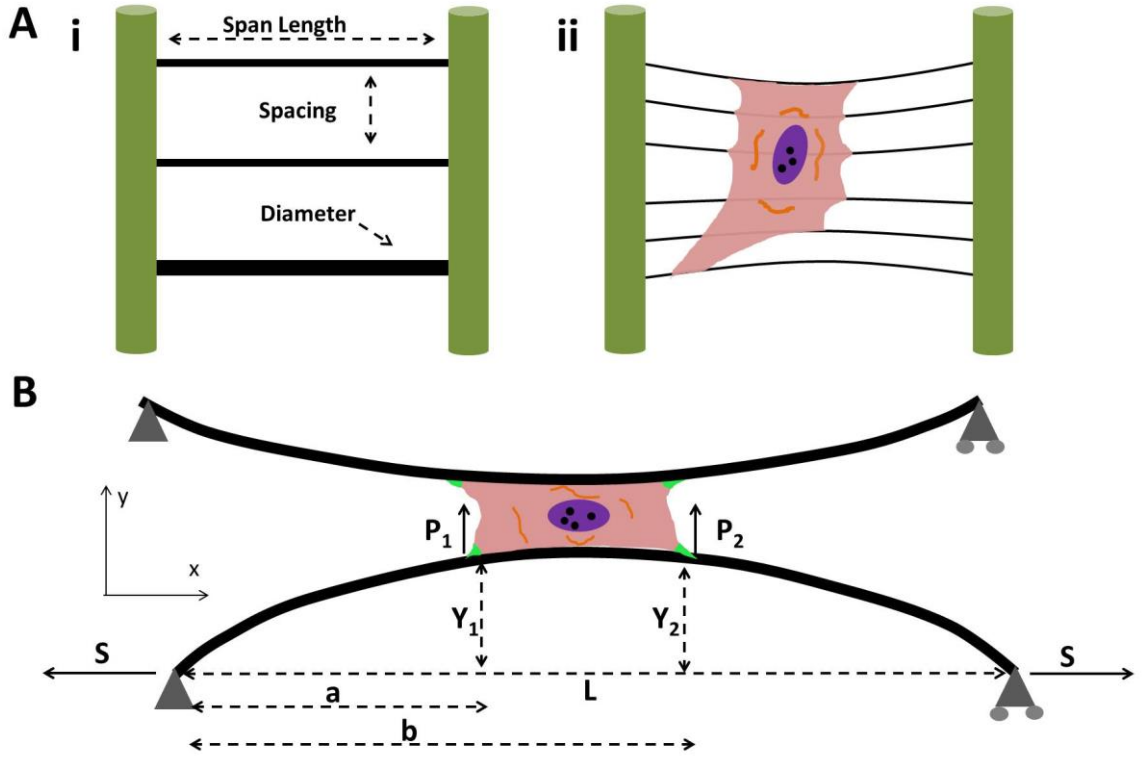

Figure 5.4 (A) Schematic illustration of the nanofiber net (i) Nanofiber net configuration (ii) MSC deflecting fibers on the nanofiber net. (B) A "Tie rod" model for MSC force calculation.

diameter can be adjusted to alter the bending stiffness (N/m).So far, both approaches have provided important quantitative information on force distributions and has led to significant improvement in understanding of spatial and temporal traction response of cells. However, there are few reports about cell mitotic force and apoptotic force, which correspond to a rounded cell shape and a "transition process" between "life" and "death". Besides, 2D gels and patterned substrates are unable to capture features of 3D in vivo fibrous ECM, such as fiber diameter (curvature) and structural bending stiffness (N/m).

In this study, we developed suspended nanofiber networks to probe mesenchymal stem cell forces. Fibers possessing diameters closely resembling those of the native fibrous ECM proteins provide a curved surface for cell attachment and have structural stiffness (N/m) that can be tuned to investigate biophysical influence on cell behaviors. The suspended nanofibers cause cells to react to surface curvature and dimensionality that flat substrates inherently mask, thus providing a unique platform for investigating cellular forces and the role of matrix stiffness in MSCs division, migration and apoptosis.

Nanofiber nets are achieved by fusing nanofiber arrays with microfibers at the intersections, as shown in **Figure 5.3** and **Figure 5.4**. The diameter, suspended length and spacing between nanofibers are precisely controlled. With known mechanical properties of the polystyrene nanofibers (Young's modulus ~1 GPa, tensile stress in the fiber~ 4.1MPa), the fiber stiffness can be varied through adjusting fiber diameter and suspended length. In our current study, the fiber

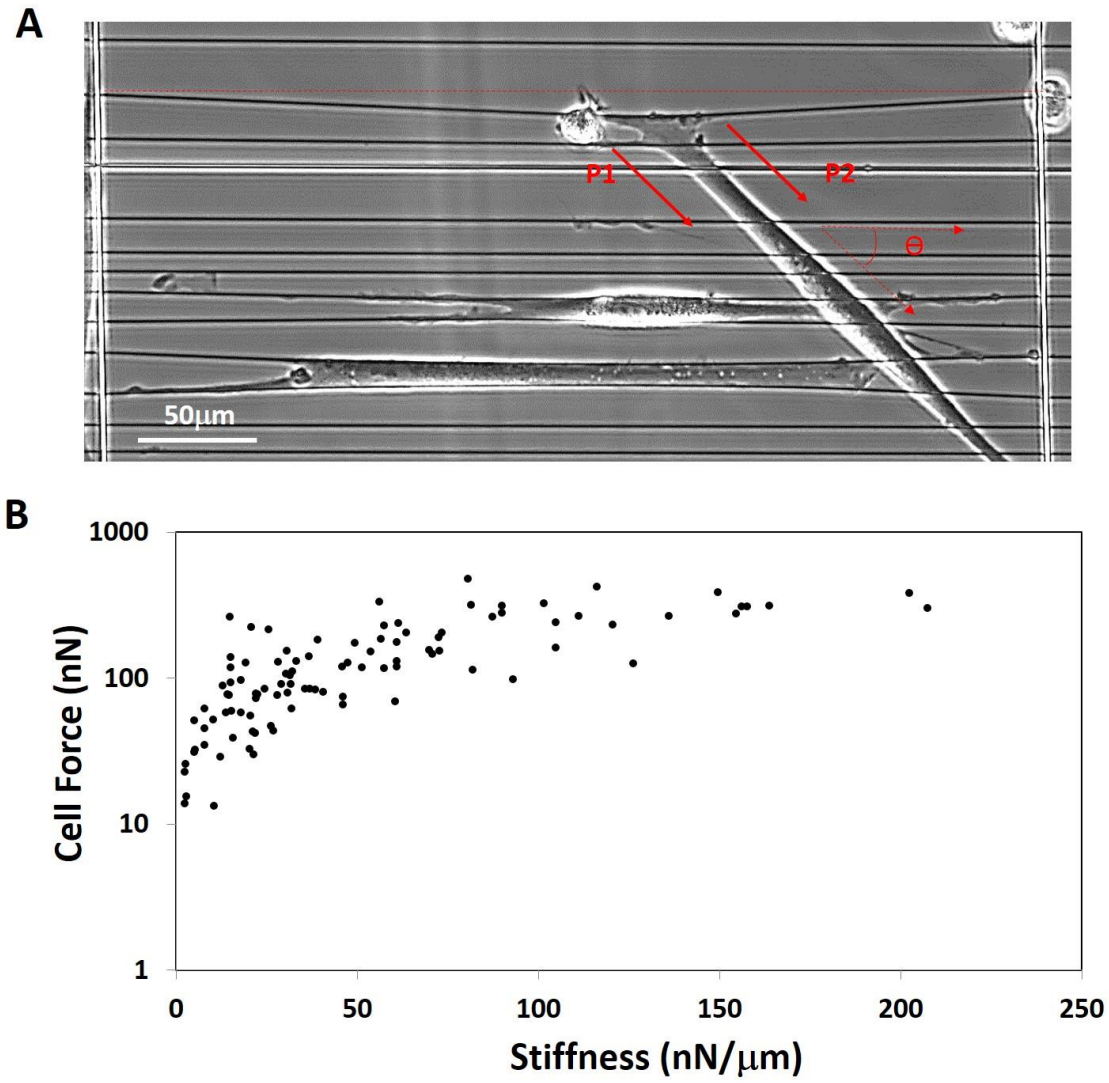

Figure 5.5 (A) A single fiber deflection with L=330μm, d=300nm, Θ=40°, P1=18nN, P2=22nN. (B) MSC contractile forces as a function of local stiffness, N=100.

stiffness is varied from 1nN/μm (corresponding to dia~150nm, length~300μm) to 300nN/μm (corresponding to dia~1000nm, length~50μm), which is comparable to the stiffness range

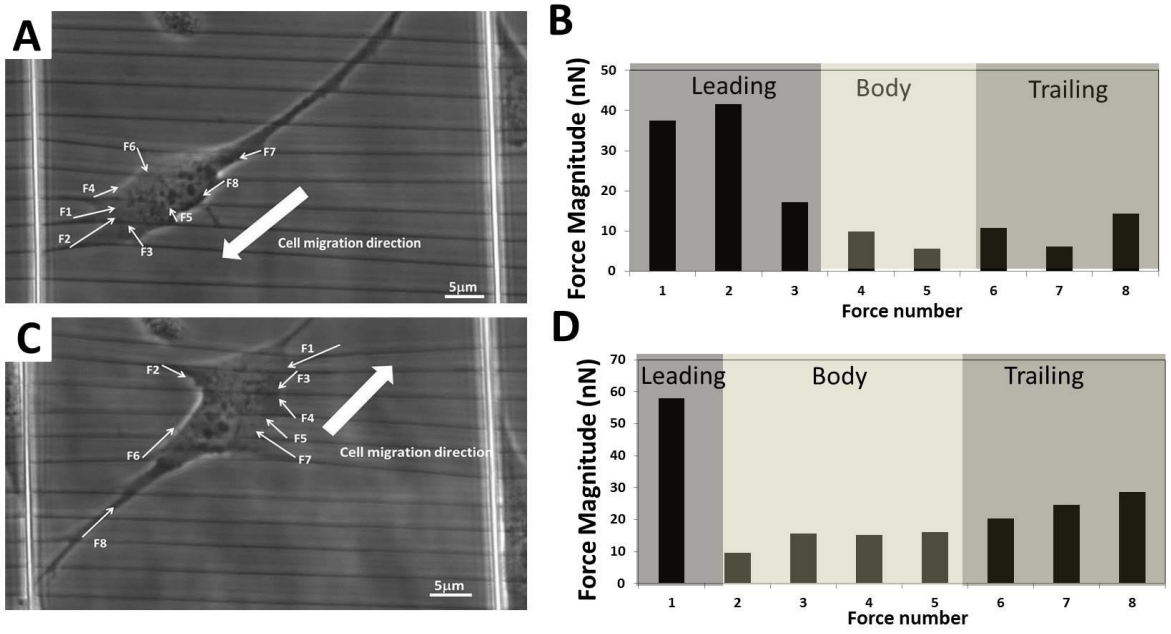

Figure 5.6 Force map of a single MSC (A) (B) at time t= 180minutes, (C) (D) at time t=210 minutes.

achieved by micropillar arrays approaches.[145,182] By controlling fiber dimensions, the fiber stiffness can be varied within a wide range of three orders of magnitude. Note that it is convenient for us to achieve nanofibers with stiffness less than 1nN/μm by further increasing the fiber length or decreasing the fiber diameter.

Cells on suspended fibers form physical contacts with the fiber through which cells apply contractile loads and deflect the fiber. The mesenchymal stem cells were assumed to exert contractile loads through focal adhesions, which locate at both edges of the cell. For cell force calculation, we use the "tie rod" model as shown in **Figure 5.4** (B). Suspended nanofibers were

considered as prismatic beams with “pin-pined” boundary conditions under elastic deformations. [183] We assume the beam is under tension which develops during manufacturing process. With these considerations, the cell contractile forces P1 and P2 are back calculated by solving the following equations:

$$-\frac{P_1 \sinh[\lambda(L-a)]}{S\lambda \sinh[\lambda L]}\sinh[\lambda a]+\frac{P_1(L-a)}{SL}a-\frac{P_2 \sinh[\lambda(L-b)]}{S\lambda \sinh[\lambda L]}\sinh[\lambda a]+\frac{P_2(L-b)}{SL}a=Y_1 \qquad \text{Eq 5.2}$$

$$-\frac{P_1 \sinh[\lambda a]}{S\lambda \sinh[\lambda L]}\sinh[\lambda(L-b)]+\frac{P_1(L-b)}{SL}a-\frac{P_2 \sinh[\lambda(L-b)]}{S\lambda \sinh[\lambda L]}\sinh[\lambda b]+\frac{P_2(L-b)}{SL}b=Y_2 \qquad \text{Eq 5.3}$$

Where $\lambda=\sqrt{\frac{S}{EI}}$, E , I and S are fiber modulus, second moment of inertia and tensile force in the fiber respectively. Y_1 and Y_2 are beam deflections at locations a and b, L is the length of the beam.

As MSCs deflect single fibers, the force directions are defined along the cell body as shown in **Figure 5.5** (A).The force-stiffness relationship is investigated as shown in **Figure 5.5** (B). Two distinct regimes are evidenced, first an increase of the cell force with the stiffness (from 13 nN to 230 nN for stiffness varying from 2nN/μm up to 100nN/μm) and then a second regime that corresponds to a plateau forces value ~260 nN, which signify the upper limit of the forces that MSCs could exert. This finding is in agreement with previous reports from Ghibaudo *et al*, who reported that there is a critical stiffness values beyond which the cell forces become saturated. [184]In their study, the critical stiffness value is 120nN/μm for epithelial cell and 130nN/μm for fibroblast, which is comparable to our results~100nN/μm. The increase of cell force with stiffness within a certain region suggests that the matrix strain may be sensed by cells as tactile set point—

cell contraction forces are regulated to achieve a certain deformation of the matrix, which is supported by previous studies of Discher et al.[185]

One of the important goals in cell force study is to achieve a force map for a single cell by increasing the spatial force resolution. Microdimensional force sensor arrays (μFSA) with large pillar densities and polymer gels with densely embedded beads have been used to achieve detailed single cell force maps. Currently, the spatial force resolution ranges from 2μm to 9μm depending on center to center distance between pillars and beads. [145,182,186] In our study, densely spaced nanofiber arrays (fiber spacing ~5μm) have been prepared for single MSC force mapping as shown in **Figure 5.6** (A)-(D). It was found that the largest contractile forces always localized at the edge of the cell, indicating that much of the mechanical work underlying cell locomotion is generated near the cell boundary. This observation of traction force decline with distance away from the edge is in agreement with previous cell force studies based on micropillar arrays.[182] In addition, we find that the advancing edge of the cell is always exerting larger forces than the mid body and posterior. Similar results have been reported by Dembo *et al*, who argues that the mid-body and posterior are more like passive structures being pulled forward by the contractions generated at the leading edge.[186] Note that our current spatial resolution (5μm) is comparable to most micro-pillar arrays (2-9μm) and polymer gels (5μm). Better resolution can be achieved by further reducing the fiber spacing, which is underway in STEP lab.

Release of caspase-3 is one the most important events in the process of apoptosis through the mitochondrial pathway and used in our study to signify the initiation of apoptosis process. It was found that the activation of caspase-3 is promoted by high stiffness. As shown in **Figure 5.7** (A),

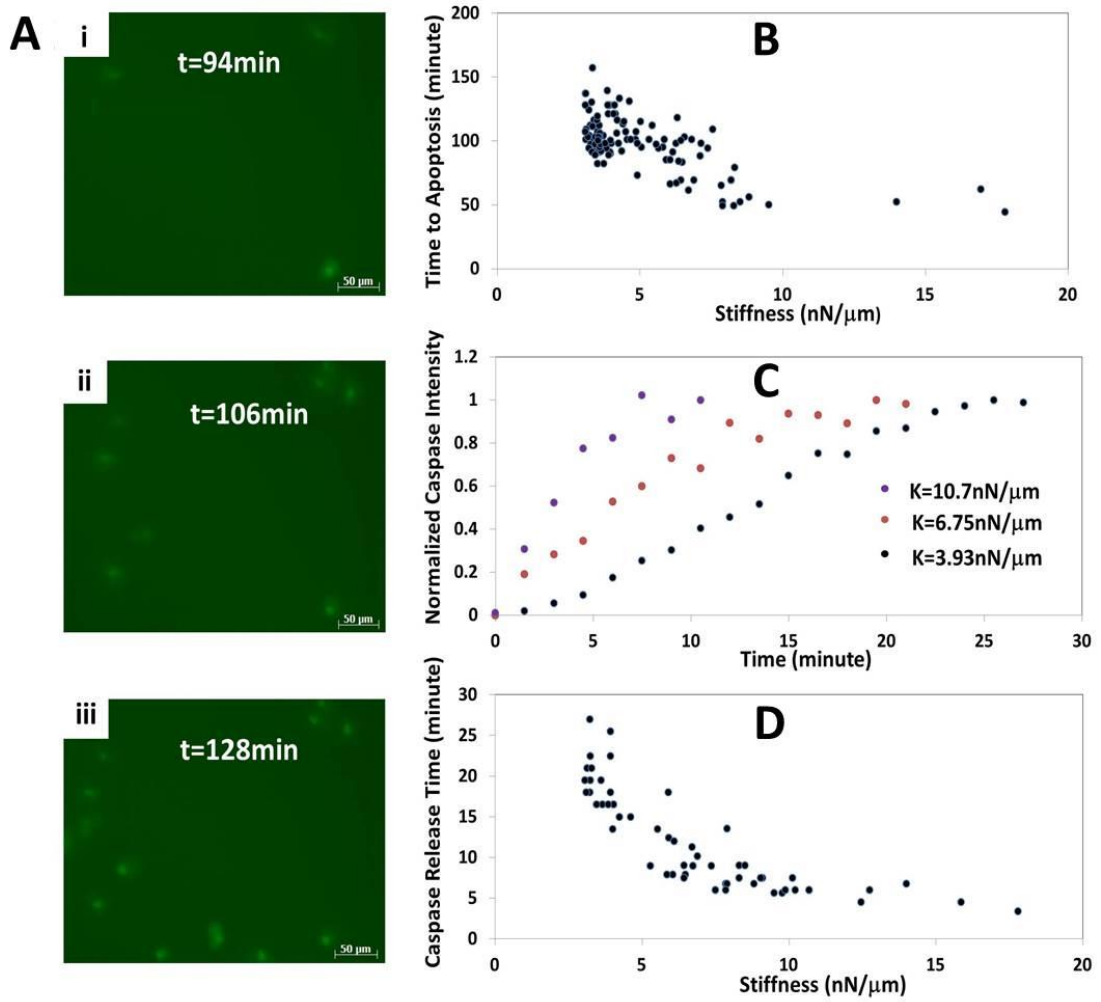

Figure 5.7(A) Time lapse of caspase activation during apoptosis process. (B) Time to commit apoptosis as a function of stiffness. (C) Caspase release curve at different stiffness. (D) Time to achieve peak caspase activity as a function of stiffness.

during the CO2 deprivation, the activation of caspase-3 first starts from the MSCs located near the both ends of the fiber and then gradually develops toward the center of the fiber. The time needed to commit apoptosis is inversely scaled with the fiber stiffness and reaches a plateau value (~50 minutes) after the stiffness value is beyond 10 nN/μm (**Figure 5.7** (B)). The caspase-3 release profile is stiffness dependent (**Figure 5.7** (C)). The caspase-3 release time is also inversely scaled with the fiber stiffness and demonstrate stiffness independent trend beyond 10 nN/μm (**Figure 5.7**

(D)). Note that our results are different from previous flat substrates based studies by Wang *et al*

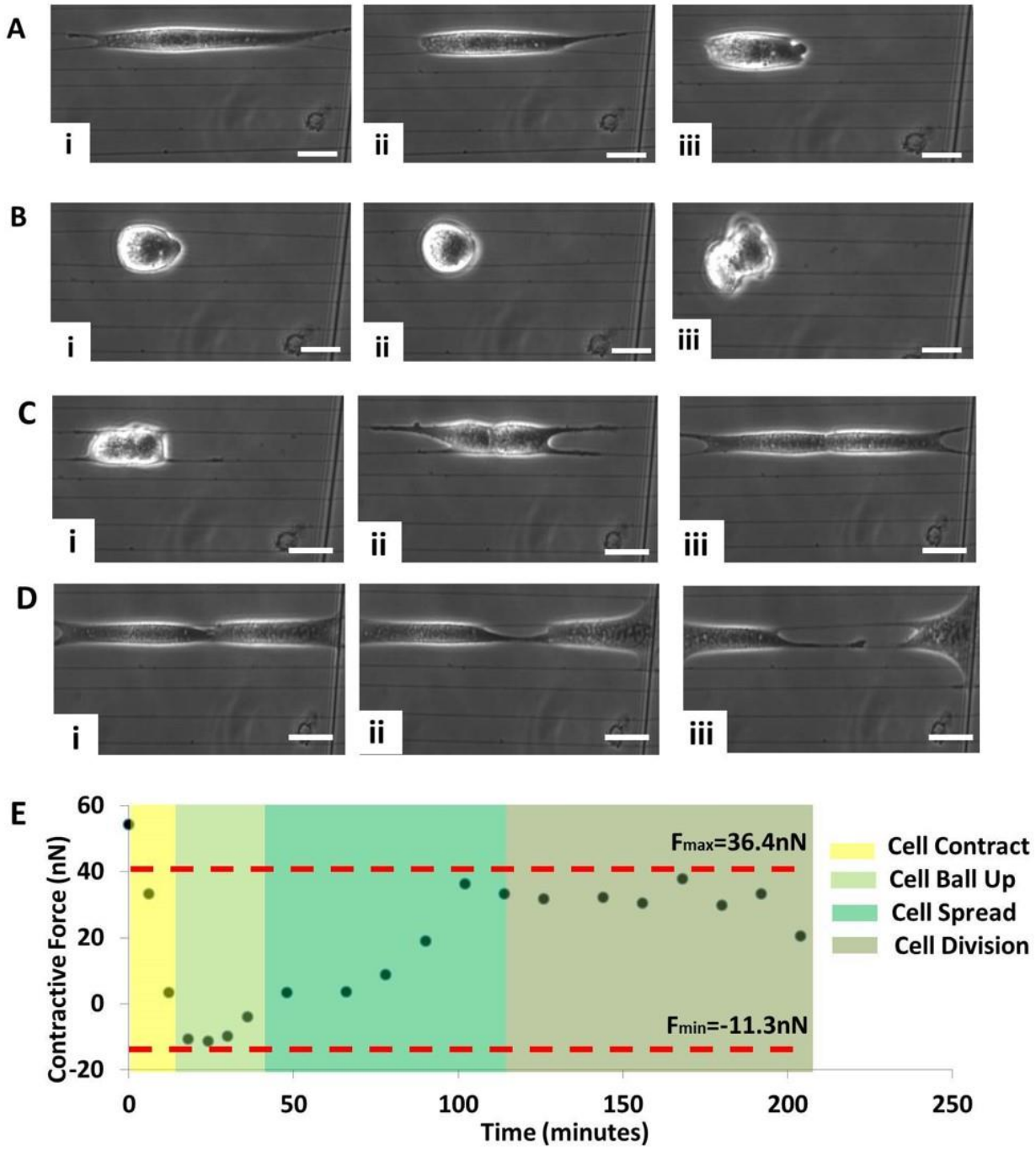

Figure 5.8 Time lapse images during cell division process showing (A) cell contract, (B) cell ball up, (C) cell spread and (D) cell division. (E) Forces exerted by the cell during the division process. Scale Bars represent 5μm.

and Zhang *et al*, who report that cell apoptosis and caspase-3 release is enhanced by soft substrates. [187,188]

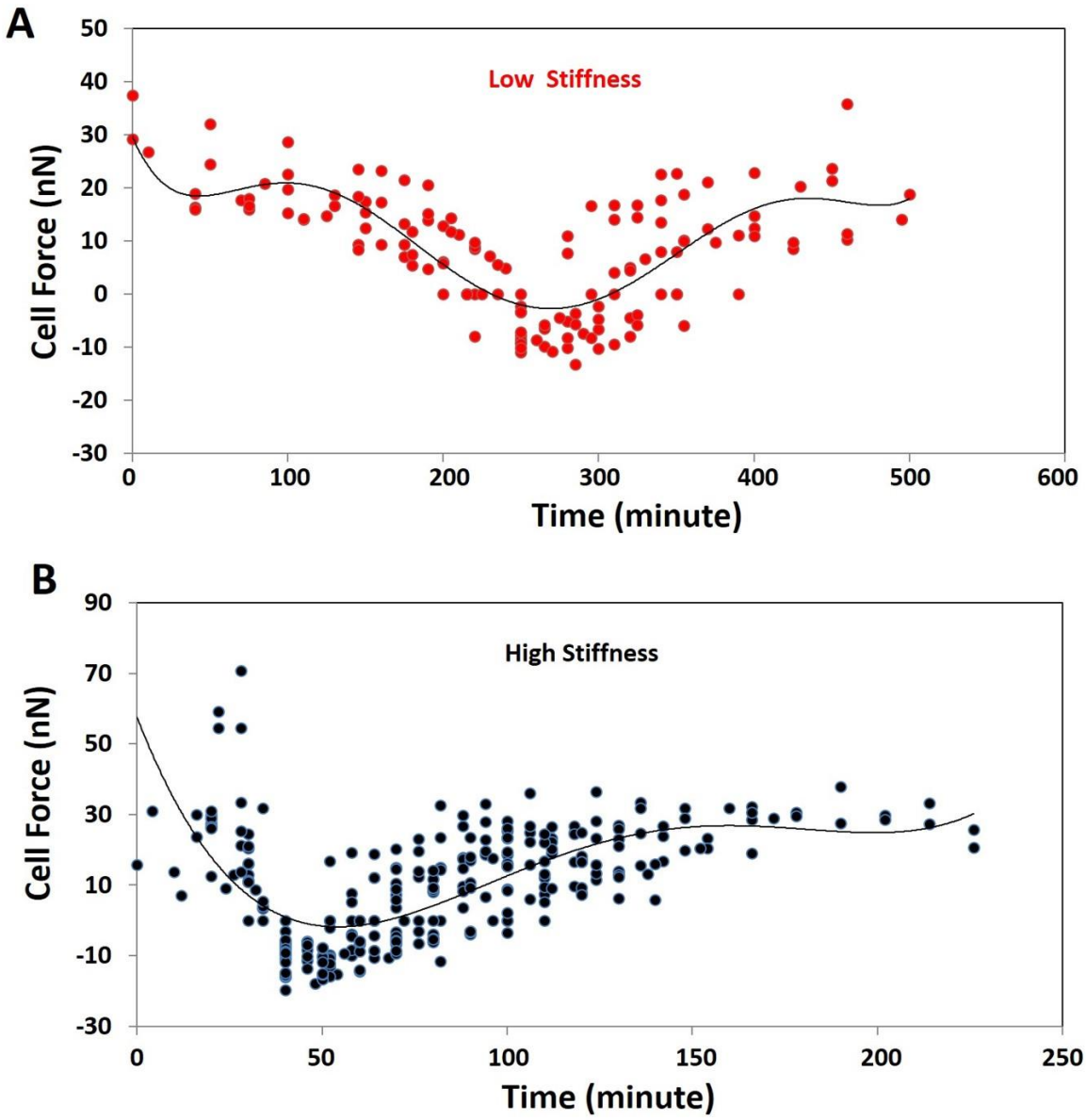

Figure 5.9 Force evolution curves superstition during of (A) MSC division process at low stiffness environment and (B) MSC division process at high stiffness environment. N=20 for high stiffness division and N=12 for low stiffness division.

Table 5.1 Summary of the cell force evolution during division process.

	Low Stiffness Division	High Stiffness Division
Stiffness range (nN/mm)	3.1-4.5	7.9-16.3
Division Force (nN)	16.0±1.9	24.6±2.7
Mitotic Rounding Force (nN)	-8.3±1.1	-9.9±0.9
Division Time (minute)	375.0±22.2	123.5±11.3

Temporal MSC forces during cell division were measured using the nanofiber net as shown in **Figure 5.8** (A)-(D). At entry to mitosis, de-adhesion from the fiber allows the cells to become round. MSC cells experience cell contraction, mitotic rounding, spread after mitosis and cytoplasm division phases, which correspond to the force evolution as shown in **Figure 5.8** (E). The forces corresponding to the mitotic rounding and cytoplasm division are found to be higher on high stiffness fibers, as summarized in **Table 5.1**. ECM stiffness was found to significantly influence the mitosis progress. As summarized in **Figure 5.9** and **Table 5.1**, low stiffness leads to long cell division process (268.2±82.4 minutes), while higher stiffness leads to short cell division process (57.7 ±22.5 minutes). ECM rigidity has been reported to modulate cell growth, including fibroblasts, hepatocytes and stem cells. Winer et al found that human mesenchymal stem cells (HMSCs) halted proliferation process on soft substrates (250 Pa).[189] Ulrich *et al* recently reported the stiffest ECMs (119 KPa) support 5 folds more proliferation of glioma cells than the

softest ones (0.08 KPa). [190] One explanation to those phenotypes is that ECM stiffness can alter the speed of progression through the cell cycle. Our results support the concept that mechanical

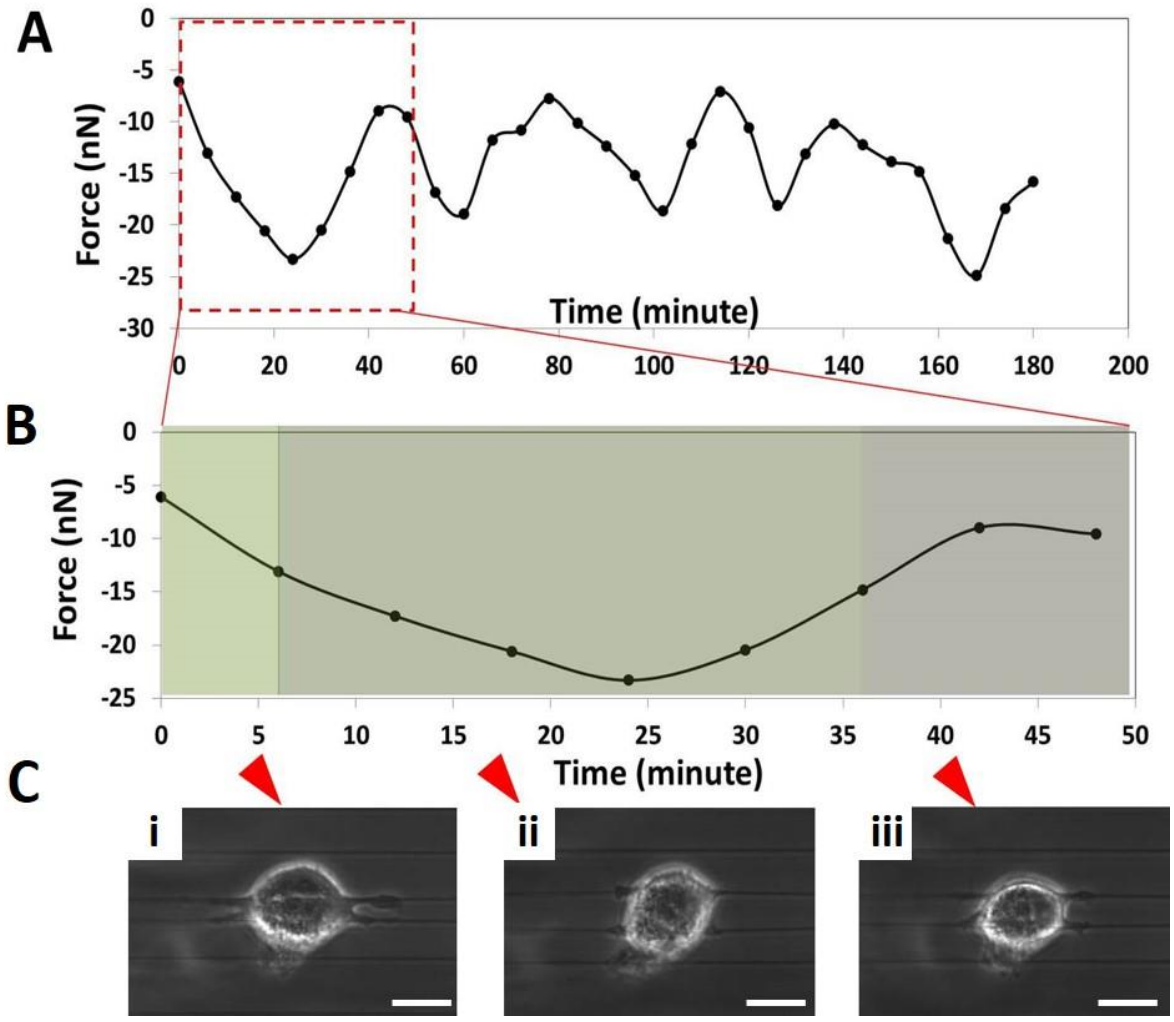

Figure 5.10 (A) A typical cell force oscillation curve during apoptosis process. (B) Force evolution during one period of the cell oscillation. (C) Cell shape evolution during the oscillation process. Scale bars in C represent 20μm.

input from the ECM, which is transmitted through adhesion receptors, might activate mitogenic signaling pathways. [191]

Cell rounding is a balancing result between contractile force and expansive force. While the expansive force is generated by osmotic pressure and related with transmembrane ion gradients,

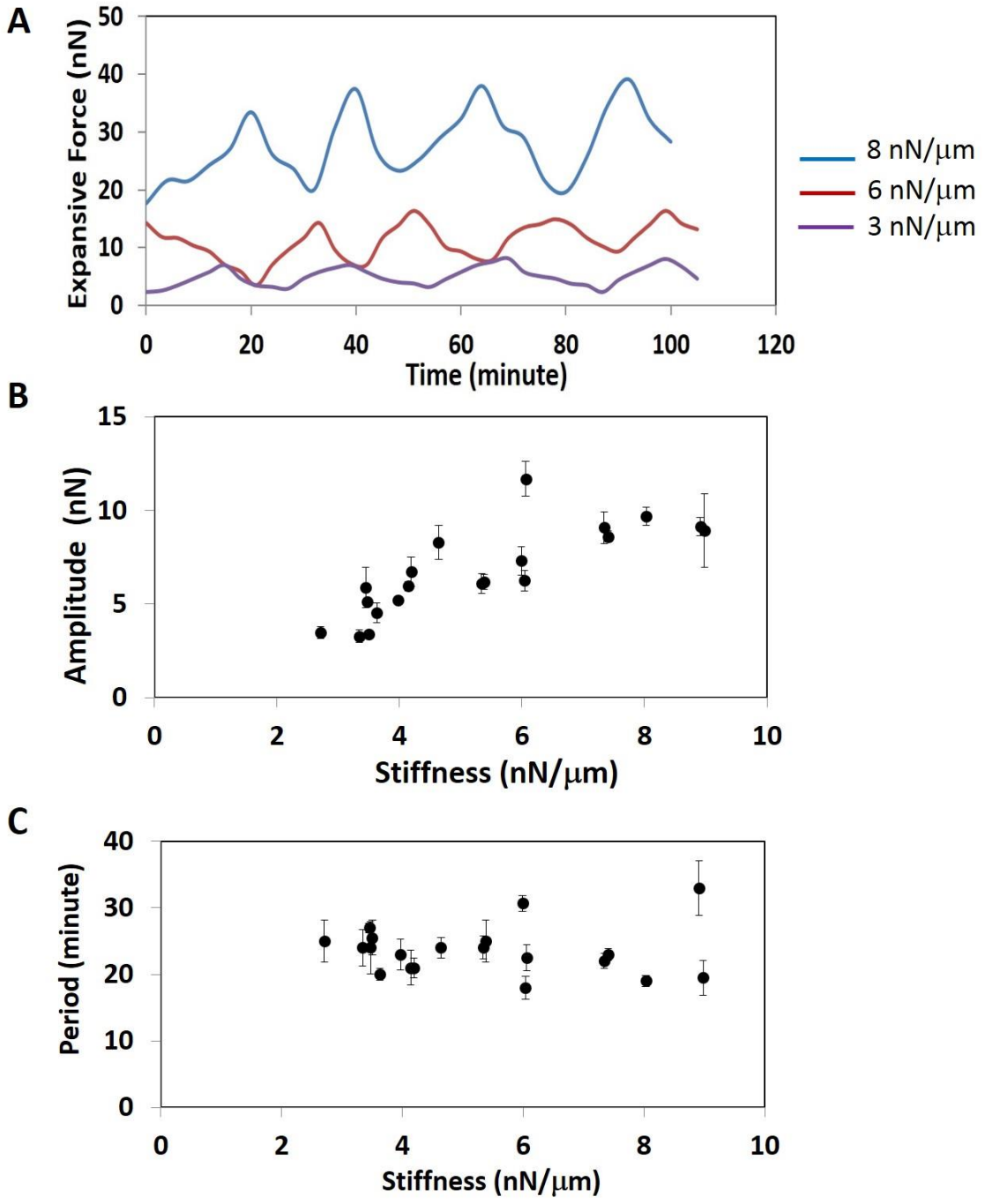

Figure 5.11 (A) Typical apoptotic expansive force oscillation curves at different stiffness regions. (B) Oscillation amplitude and (C) oscillation period as a function of stiffness.

the contractile force is based on contractility of actomyosin cortex. [192] During cell apoptosis process, oscillations in the cell force were observed, which correlated with cell shape alteration. (**Figure 5.10**). The expansive forces exerted by the cell peaks as the cell balls up and gradually decreases as the cell becomes spread. In our study, oscillations are observed only on cells which have point-like contacts with fibers, which is a result of cell rounding process. The oscillation disappears in spread MSCs, which forms extensive focal adhesions with fibers. The dependence of oscillation on the extent of adhesion suggests that there may be a signal transduction pathway triggered by the cell detachment. Cellular oscillation is based on the instability of the cortical layer, which generate contractile forces and create deformation on the cell body. Salbreux *et al* proposed that the instability of the cortical layer is related with calcium density within the cell. [193]

In our study, the oscillation amplitude (nN) increases with the ECM stiffness and become stable for stiffness >6nN/μm, as shown in **Figure 5.11** (A)(B). The actomyosin based rigidity sensing mechanism was summarized by Borau *et al*—softer ECM leads to shrunken and dense actomyosin networks, whereas stiffer ones result in heterogeneous networks with highly stretched filaments.[194] The plateau force value in **Figure 5.11** (B) signifies the maximum force can be exerted by the actomyosin networks, which is independent of ECM stiffness. Note that this plateau value (< 10nN) is much lower than the saturated MSC contractile force value (230nN) in **Figure 5.5** (B), which indicates the contractility of actomyosin is limited in apoptotic cells. The periods of the oscillation do not respond to the stiffness variation. (**Figure 5.11**(C)) The rounded cells oscillate at constant period for several hours, indicating that oscillatory behavior is a robust feature of rounded cells. Interestingly, we observed that roughly 60% of the oscillation cells exhibit blebbing, which is also a dynamic process requiring actomyosin contractility in the cortex. Most

blebbing MSCs have spread area less than 400 μm^2, which is in agreement with our previous studies showing that blebs do not appear past a critical cellular spread area~1400 μm^2. [16]

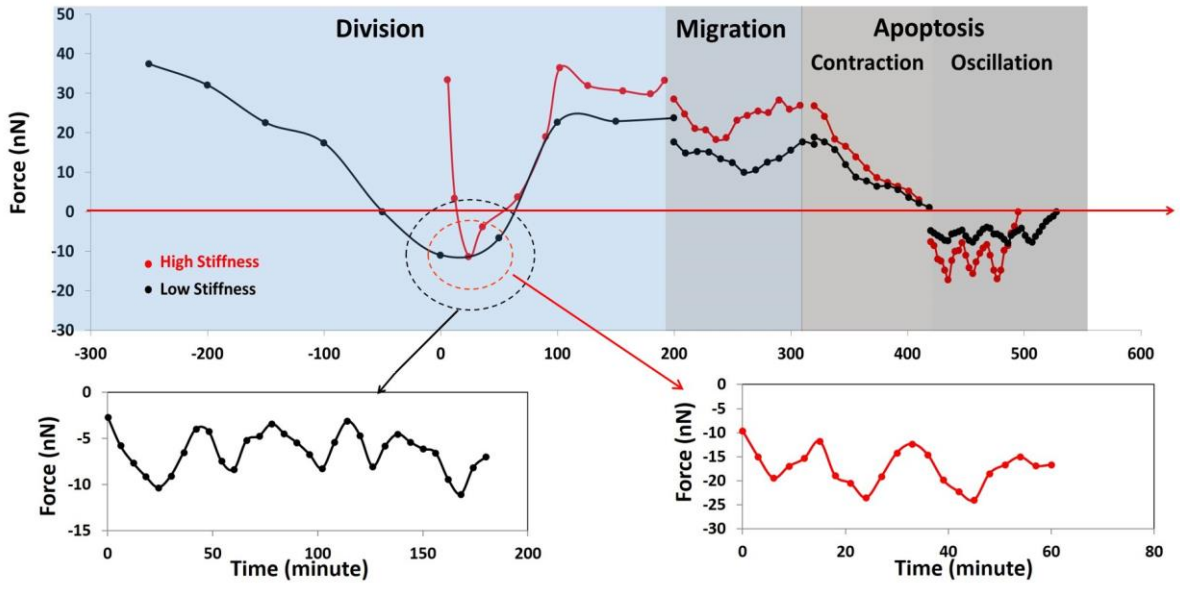

Figure 5.12 Global MSC force evolution curves during life cycle.

The cell force evolution during MSCs life cycle is summarized in **Figure 5.12**, which includes cell division, migration and apoptosis courses. In our study, cell oscillation was also observed during mitosis process. Higher ECM stiffness increases the magnitude of the cell force in each courses, more importantly, higher ECM stiffness accelerates the mitosis and apoptosis process. In other words, MSCs have a shorter life cycle in stiffer environment.

5.5 Conclusion

Suspended planar and non-planar nanofiber scaffolds with precisely controlled pore size and fiber orientation have been developed using STEP technique, which offers an opportunity to closely represent the native environments aimed at recapitulating cell behaviors *in vitro*. Our results

demonstrate that changes spacing and orientation of suspended fibrous hierarchical assemblies elicit varied responses from cells, as measured by cell densities and spread areas. The suspended nanofiber assemblies provide cells with simultaneous 1, 2 and 3D cues, as cells are able to align along fiber axis (1D), spread between multiple fibers (2D) and wrap around fibers (3D). Based on the nanofiber assemblies, we developed ECM mimicking nanofiber nets to investigate MSCs forces during their life cycle. The MSC forces increases with the fiber stiffness until a critical stiffness value is reached. During cell migration, the leading edges of the cell were found to exert larger contraction forces than the cell body and posterior part. MSCs demonstrate expansive rounding forces and oscillation behaviors during mitosis and apoptosis process. Our study examined MSCs behavior over a broad range of stiffness and found that higher stiffness not only enhances cell force magnitudes but also accelerates cell mitosis and apoptosis process. Variation in stiffness may be used as a control parameter to tune cell proliferation and self-renew process. We envision that precisely deposited suspended nanofibers on varied three dimensional shapes could find wide applications in diverse fields such as wound healing, organ regeneration and developmental and disease biology.

Chapter 6 Organized Long Titanium Dioxide Nanofibers/Nanotubes

Ji Wang, Junbo Hou, Michael.W.Ellis, Amrinder S.Nain, New Journal of Chemistry, 2013, 37, 571-574. Used with permission of Royal Society of Chemistry, 2015.

6.1 Introduction

Titanium dioxide (TiO_2), also known as titania, has a number of unique properties, which have wide applications in photocatalysis, super-wetting surface, solar cell and biomedical applications. [195–198]In the past decade, nanostructures of TiO_2 such as nanofibers and nanotubes have been extensively studied for improved properties. These one dimensional TiO_2 structures demonstrate superior properties compared to bulk TiO_2, which is mainly attributed to their increased specific area and quantum confinement effects.[199] There are several approaches reported in the literature

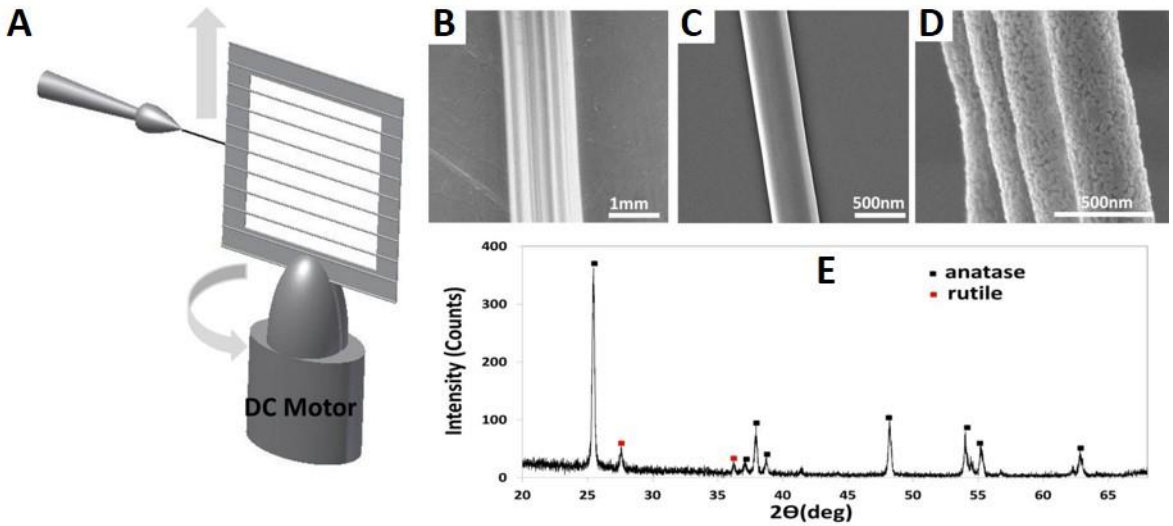

Figure 6.1 (A) Schematic of STEP technique, (B) as spun precursor fiber bundles,(C) scanning electron microscope (SEM) image of a precursor fiber surface,(D) SEM image of aligned titania fibers obtained through calcination,(E) XRD pattern of TiO_2 fibers. Wang et al, New Journal of Chemistry, 2013, 37. Used with permission of Royal Society of Chemistry, 2015.

to prepare TiO_2 nanofiber/tube structures. One approach is the anodic growth of TiO_2 nanotube arrays in electrolytes, which allows formation of self-organized nanotube layers with limited

thickness not exceeding 300 microns.[200–202] Another approach, the electrospinning based sol-gel process, has been widely used to produce titania nanofiber/tube structures of considerable length. Li *et al* reported titania nanofibers obtained from PVP/TiO_2 precursor fibers. [203] By controlling processing parameters, the TiO_2 nanofiber diameter could be controlled from 20 to 200nm. Zhan *et al* obtained TiO_2 hollow fibers through coaxial electrospinning.[204] Caruso *et al* obtained TiO_2 tubes with secondary structures by dip coating electrospun porous poly(L-lactide) fibers. [56]Kim *et al* coated electrospun poly(vinly pyrrolidone) fibers using atomic layer deposition and obtained pure anatase TiO_2 submicrotubes.[57] Although these techniques, which

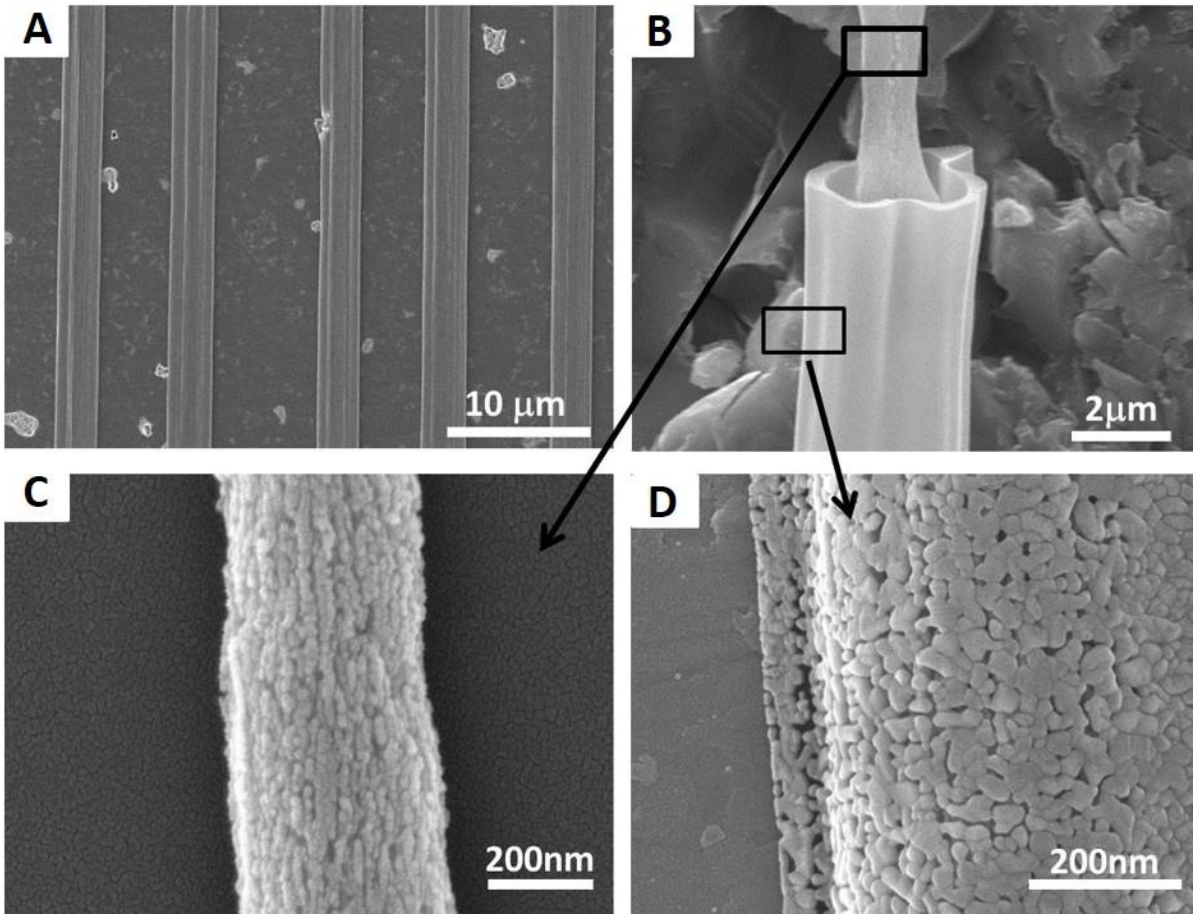

Figure 6.2 SEM images of (A) evenly spaced NW@MT structures, (B) fracture surface of a NW@MT structure,(C) a zoomed-in area of the nanowire, (D) a zoomed-in area of the microtube surface. Wang et al, New Journal of Chemistry, 2013, 37. Used with permission of Royal Society of Chemistry, 2015.

combine sol-gel processes with electrospinning, provide a straightforward strategy for processing long titania fiber/tube structures, the fibers/tubes obtained are usually randomly collected, due to the instabilities associated with the electrospinning process.

In this work, we demonstrate an effective and robust strategy for fabricating organized and long 1D titania structures by combining the sol-gel process with recently reported Spinneret-based Tunable Engineered Parameters (STEP) fiber manufacturing technique. The STEP technique provides unique control on fiber i) alignment, ii) spacing, iii) length, iv) diameter (sub 100nm to several microns), and v) scalability to develop assemblies. Long 1 D structures obtained through this method include fibers, tubes, nanowire in microtubes (NW@MT), and particle chains. The capability and feasibility of the technique presented in this work provides a promising approach for fabrication of aligned 1D inorganic structures as building blocks for use in widespread future applications.

6.2 Experimental Section

Sol-gel coating: PS (2000K $g.mol^{-1}$, 860K $g.mol^{-1}$) was dissolved in *p*-xylene at various concentrations at room temperature for one week prior to experiment. For precursor solution preparation, titanium tetraisopropoxide ($Ti(OiPr)_4$) was added to PS/*p*-xylene solutions. The mixture was vigorously stirred for 12 h at room temperature to ensure homogeneity. As spun fiber bundles were dried in a vacuum desiccator for 24 hours to remove any remaining solvent. Dilute $Ti(OiPr)_4$ solutions (1:19 and 1:39 in isopropanol) were dripped onto the fiber bundles, which were then soaked in isopropanol/water (1:1,v/v) for hydrolysis followed by drying in a vacuum desiccator for another 24 hours. Precursor fibers and sol-gel coated PS fibers were transferred into an autoclave for calcination at 700°C for 4 h. A slow heating rate of 0.5°C/min was adopted in order to prevent collapse or breaking of titania structures.

Characterization: Thermal gravimetric (TG) analysis was employed to evaluate the weight loss of the samples under air flow of 20mL.min^{-1} and a heating rate of 20°C.min^{-1} using a thermal analyzer (TGA/SDTA, 851,METTLER). The X-ray diffraction (XRD) pattern was recorded using a Philips PW-1710 diffractometer (Cu Kα radiation) at a scanning rate of 0.05°/s in 2Θ ranging 20° to 70°. For SEM (Zeiss, Leo 1550) analysis, the samples were sputter coated.

Photocatalytic activity measurement: the photocatalytic activities of TiO_2 structures were tested on photo-oxidation of methylene blue. TiO_2 samples with the weight of 2 mg were added to 20.0ml methylene blue solution with a concentration of 10.0mg/L. The mixture were kept in dark for 30mins to that adsorption and desorption was reached before irradiation. After that, the sample was irradiated by a 160W high-pressure mercury lamp at a distance of 30 cm. The change of absorption at 664nm was applied to identify the concentration of methylene blue using UV-vis spectrophotometer (Lambda 35, Perkin-Elmer) and the concentration of methylene blue was measured as a function of irradiation time.

6.3 TiO2 Nanofibers with Varied Morphologies

Polymer solution is pumped through a spinneret and forms a droplet at the nozzle, which contacts the rotating substrate. Being a non-electrospinning technique, filament whipping or bending is eliminated and the as- spun fibers are collected in parallel configurations on the substrate, as shown in **Figure 6.1** (A). The desired spacing between neighbouring fibers is achieved by controlling both the substrate rotation and translation speeds. Control of fiber diameter is achieved through control of solution rheology (solution concentration and molecular weight of polymer).

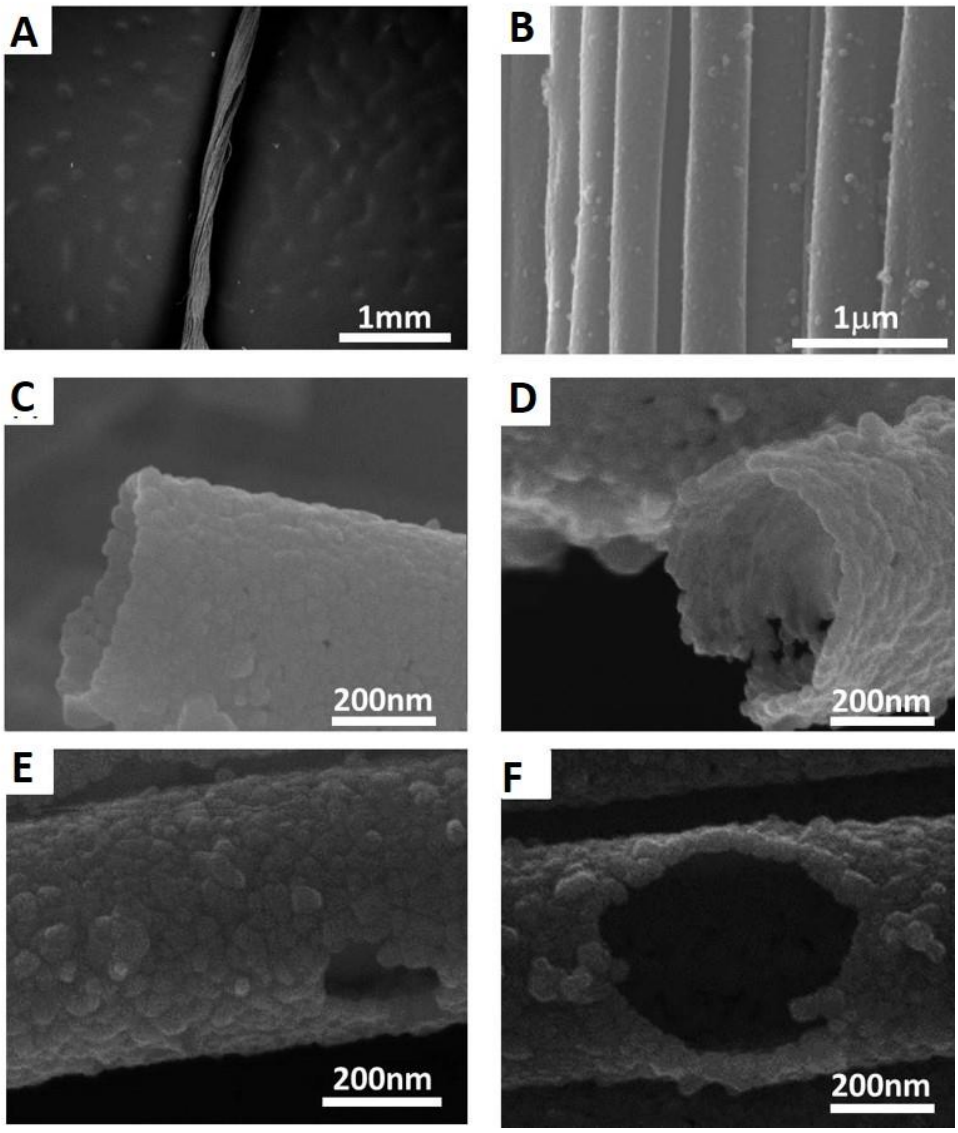

Figure 6.2 SEM images of (A) twisted titania tube yarn ,(B)parallel uniform titania tubes within the yarn, (C)-(D) fracture surface of titania tubes, (E) -(F) titania tube with holes in the wall. Wang et al, New Journal of Chemistry, 2013, 37. Used with permission of Royal Society of Chemistry, 2015.

Using the STEP technique, polystyrene (PS) was used as a carrier of titanium tetraisopropoxide ($Ti(OiPr)_4$). As shown in **Figure 6.1** (B), unidirectional nanofiber bundles (dia ~ 500nm) were obtained from solutions containing 70mg $Ti(OiPr)_4$, 20mg 2000K PS, and 0.3ml *p*-xylene. After hydrolysis in water and drying in a vacuum desiccator overnight, the fibers appear smooth and uniform as shown in **Figure 6.1 (C)**. A TG curve shows that the PS was removed from the fibers

upon calcination. (**Appendix E**) Above 450°C there was no further weight loss, which indicates the organic component has been entirely decomposed. After calcination, continuous nanofibers (dia~350nm) were obtained through sintering of TiO_2 particles which are 30-40nm in diameter, as shown in **Figure 6.1**(D). The reduced diameter could be attributed to loss of PS and crystallization of TiO_2. Note that the original parallel configuration of the fibers was well preserved after calcination. **Figure 6.1** (E) shows a XRD pattern of the calcined sample, which indicates the formation of anatase phase nanocrystals.

NW@MT structures are conventionally obtained through co-axial electrospinning and a dual or triple capillary spinneret were utilized to delivery immiscible solutions. Chen *et al* reported TiO_2

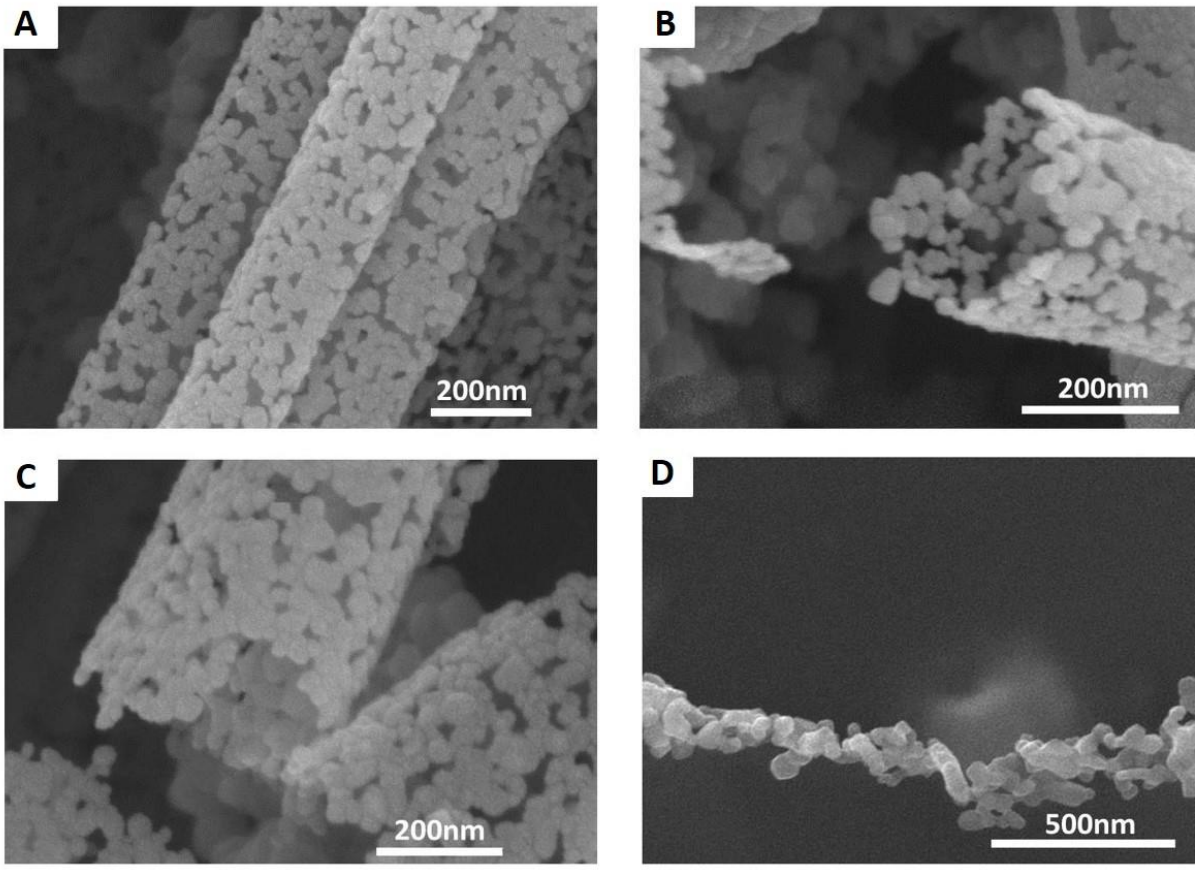

Figure 6.3 SEM images of (A) unidirectional bundles of mesoporous titania tubes, (B)-(C) fracture surface of mesoporous titania tubes, (D) titania particle chains. Wang et al, New Journal of Chemistry, 2013, 37. Used with permission of Royal Society of Chemistry, 2015.

NW@MT structures using a triple capillary spinneret.[204] Here we demonstrated the possibility to achieve NW@MT TiO_2 structures through calcination of micro-scale precursor fibers of uniform composition. The obtained NW@MT structures were uniform in dimension and well aligned with desired spacing (**Figure 6.2** (A)). Our preliminary results suggest that NW@MT structures were highly repeatable from micro-scale precursor fibers (diameter>3μm), while solid titania fibers were obtained when precursor fibers diameter is less than 800nm. Zoomed in SEM image from the fracture surface (**Figure 6.2** (B)) reveals a typical nanowire in a micro tube (NW@MT) structure -- a nanowire of ~500nm in diameter forms within the shell which is smooth on both the inner and outer walls with wall thickness varying between 200nm and 600nm. The formation of NW@MT could be due to shrinkage mismatch between core and shell—core portion continues to shrink throughout calcination process while shell portion becomes solidified at early stage. Continuous core shrinkage also leads to shell buckling, as evidenced by the wrinkled surface in **Figure 6.2**(A) and (B). The average nanoparticle diameter was approximately 10nm in the nanowire as shown in **Figure 6.2** (C), which is much smaller than the average particle size in the shell (30-40nm in diameter) (**Figure 6.2** (D)). As reported by Zhan *et al*, higher calcination

temperature leads to larger titania particle size. [204] The difference in particle sizes in our case indicates there may be a temperature gap between shell and cores during heat treatment.

To obtain TiO_2 tubular structures, a 4 cm long bundle of PS fibers (600nm in diameter spun from 110mg/ml of 2000K PS solution in *p*-xylene) was coated with dilute solution of $Ti(OiPr)_4$ in isopropanol (1:19,v/v) . After hydrolysis, the bundle was twisted into a yarn using a custom made device to increase the integrity. Upon calcination, yarns of long titania tubes were obtained as shown in **Figure 6.3** (A). The tube structures of uniform diameters (approximately 500nm (**Figure 6.3**(B)) were found to have smooth surface, demonstrating a shrinkage of 17% during calcination. A wall thickness of 30-40nm was obtained (**Figure 6.3**(C) and (D)). No cracks were observed along the long tubes, instead,holes in the tube wall were observed, which might be caused

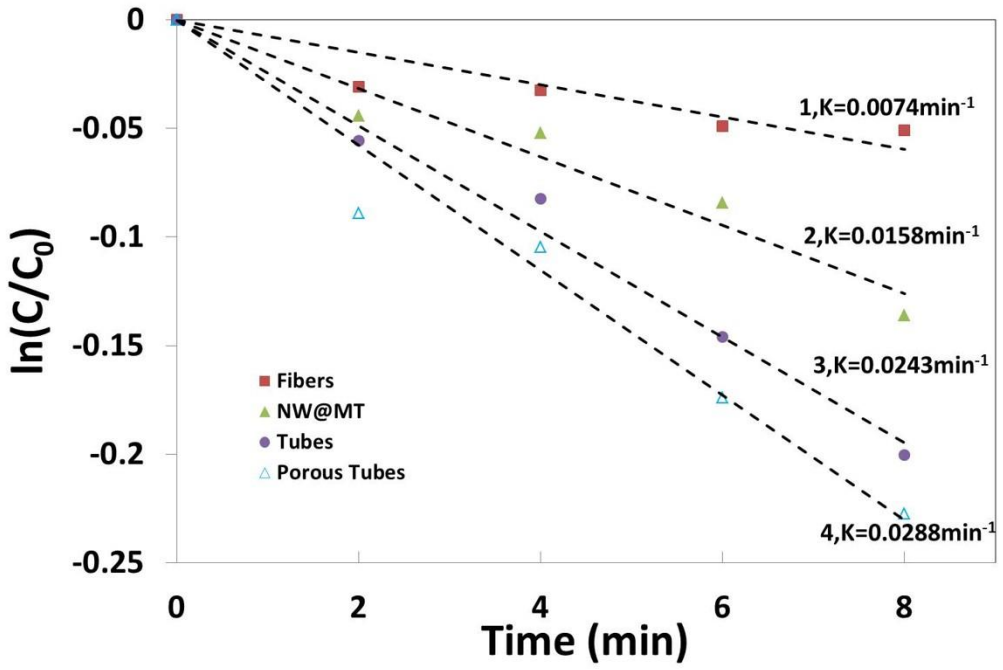

Figure 6.4 UV photodegradation of methylene blue. Curves: (1) without photocatalyst, (2) TiO2 fibers (diameter~350nm),(3) TiO2 NW@MTs (Nanowire diameter ~500nm,Tube diameter 3-4μm),(4) TiO2 tubes (diameter ~500nm),(5) TiO2 porous tubes (diameter~250nm). Rate constants **k** are labelled for curves 2-5. Wang et al, New Journal of Chemistry, 2013, 37. Used with permission of Royal Society of Chemistry, 2015.

by polymer degradation effects on sintered walls. These structures are similar to those reported in literature for carbon micro-tubes, which were obtained through carbonization of polyacrylonitrile/poly(methyl methacrylate) (PAN/PMMA) shell/core fibers.[78]

Hollow tubes with mesoporous walls are highly desirable structures with potential applications in catalysis, selective separation, sensor arrays and magnetic devices. Previous work has demonstrated mesoporous titania fibers/tubes through the addition of tetrabutylammonium hydroxide into precursor solutions.[204] Here we demonstrate a simpler, faster and cost effective approach to achieve porous tube walls by controlling the sol-gel coating solution concentration. 300nm diameter PS fiber (spun from 50mg/ml of 2000K PS solution in *p*-xylene) bundles were used as templates and coated with dilute solution of $Ti(OiPr)_4$ in isopropanol (1:39,v/v). Following the hydrolysis and calcination procedures, as previously described, highly porous TiO_2 hollow tubes with diameter approximately 250nm were achieved as shown in **Figure 6.4** (A). The size of porosity was observed to range from 10-50nm. The length of the mesoporous tubes could be varied from 0.5mm to 8cm by employing fiber bundles of different length as template. Inspection of the tube fracture surface revealed a single layer of TiO_2 nanoparticles less than 10nm in thickness, as shown in **Figure 6.4** (B)-(C). The formation of pores could be attributed to the growth and condensation of TiO_2 grains. To further increase the surface area to volume ratio, 100nm diameter fibers (from 110mg/ml of 860K PS in *p*-xylene solution) were used as templates. After calcination, TiO_2 nanoparticles sintered together, thus forming a continuous chain (diameter: 30-100nm) as shown in **Figure 6.4** (D).

6.4 Photocatalytic Activity of TiO_2 Nanofibers

The photocatalytic activity of TiO_2 is greatly affected by its morphology such as surface area, particle size and porosity. The photocatalytic properties of TiO_2 structures fabricated using STEP

platform were evaluated by photo oxidation of methylene blue, as shown in **Figure 6.5**. Compared to the non-catalyst case, which hardly decomposed under UV light irradiation (curve 1), TiO_2 catalysts yield an increased rate of methylene blue decomposition. Specifically, porous tubes exhibited the highest activity (curve 5) and solid fibers the least (curve 2). Compared with the TiO_2 nanofibers, all the tube structures (including NW@MT, smooth tubes and porous tubes) presented a markedly improved photocatalytic activity. Based on the first-order kinetics of methylene blue degradation: [205,206]

$$\ln(C/C_0) = -kt \qquad \text{Eq 6.1}$$

the photo degradation rate constants k , were calculated (**Figure 6.5**), clearly demonstrating that the porous tube structures provided the highest photocatalytic activity, which may be due to its large specific area. The photo degradation constants in this study are roughly in the range of reported values (0.01~0.03 min^{-1}) of varied titania nanostructures.[205,207,208] (**Appendix F**)

6.5 Conclusion

In summary, highly aligned and long TiO_2 structures including fibers, NW@MT, tubes and particle chains were obtained through the combination of the sol-gel process with the STEP fiber manufacturing technique. On removal of thermal degradable PS, continuous 1-D nanostructures are produced and the obtained morphologies can be controlled through adjusting a series of processing parameters. All nanostructures were several centimeters long and could be manipulated into organized formats such as bundles, arrays and twisted yarns. TiO_2 tube structures demonstrate higher photocatalytic activities than TiO_2 fiber with porous nanotube structures providing the highest photocatalytic activities. We envision the procedures and methods outlined in this study

can be extended to provide a roadmap to produce organized and continuous nanostructures extended to oxides such as SnO_2, SiO_2 and ZrO_2 for a diverse range of applications.

Chapter 7 Conclusions

To summarize the body of this study, highly aligned nanofibers with controlled morphologies and well characterized mechanical properties have been developed and their applications in biology and advanced materials have been demonstrated.

STEP technique was utilized in this study to achieve aligned nanofiber arrays. An isodiametric design space was developed through molecular entanglement based scaling laws. Smooth and uniform polymer fibers with substantial length (at least several millimeter in length) start to form when the solution concentration is beyond critical entanglement concentration C_e, which signifies the transition from semi-dilute un-entangled to semi-dilute entangled domain. Beaded fibers formed from the semi-dilute un-entangled solutions and macro fibers were obtained from highly concentrated solutions. From the isodiametric design space, the same diameter fiber can be achieved from different combinations of polymer molecular weights and solution concentrations. For polystyrene, the diameter can be ranged from 70nm to 800nm. This study demonstrates that STEP technique can be extended to wide range of polymers, including polyurethane, PMMA, PEO and fibrinogen. Aligned polymer nanofibers with substantial length and tightly controlled diameter have been demonstrated using these polymer species.

Fiber morphology can be tuned through manipulation of the solidification process. While fast solvent evaporation leads to solid fibers, prolonged solidification process produces hollow tube structures. For the first time, we demonstrate long porous tubes with surface pores produced using a single nozzle. By adjusting the polymer solution concentration, the tube wall thickness and tube diameter can be accurately controlled. In addition, the surface porosity of the tube wall can be tuned through the relative humidity. It was shown that strength of these porous tubes can be

improved by 120% by incorporating 2% wt MWCNTs. These porous tubes demonstrate large specific surface area and excellent oil absorption capacities.

To characterize single nanofiber mechanical properties, an integrated nanofiber deposition and deflection approach was utilized in this study. Aligned nanofibers were deposited with fixed-fixed boundary conditions by moving an extruded solution droplet across a TEM grid. The position of fibers were obtained at low magnification of TEM and subsequently an AFM cantilever was brought to the vicinity of the fibers and deflect them laterally. This approach allows mechanical tests of wide range of fiber diameters (from 40nm to 500nm) and enough number of samples can be tested to achieve fiber strength distribution. It was found that the modulus of PS nanofibers is ~1GPa, which does not demonstrate difference as fiber diameter reduces. The reason was attributed to the absence of chain orientation in as spun fibers. Also, the molecular weight (2M, 860k and 400k) and strain rate (2Hz, 0.5Hz and 0.1Hz) variations do not produce significant change in modulus. The tensile force developed during the manufacturing process was found to scale with fiber diameter (D^2) and the tensile stress is ~4MPa. Single fiber strength demonstrate significant enhancement as fiber diameter reduces to sub 50nm and the fiber strength distribution can be described by a two parameter Weibull function. The Weibull modulus found in this study are larger than the values of electrospun fibers, which indicates more uniformly distributed defects in STEP fibers. The suspended nanofibers on TEM grid afford us a unique opportunity to investigate the chain orientation is deformed nanofibers. It was found that large elongation (~60%) leads to significant chain orientation (f ~0.28-0.68) and small elongation (~20%) produces less pronounced chain orientation (f ~0.14-0.16). Nanofiber yarns demonstrated an optimal twisting angle for the strength, which is a combined results of fiber orientation, inter-fiber friction, fiber volume fraction and fiber fusion.

Hierarchical nanofiber assemblies were developed as bio-scaffolds with tight control on fiber spacing and fiber orientation. Cell attachment is enhanced by reducing fiber spacing and incorporating more nanofibers into the scaffolds, while cell spreading is promoted by the crisscross configurations of the scaffolds.

Nanofiber assembly based cell force measurment platform was developed, which can provide cell force map of a single MSC during cell division, migration apoptosis process. Cell forces were back calculated from the fiber deflections. It was found that higher stiffness leads to faster cell division and apoptosis process. The force-fiber stiffness relationship exhibits two distinct regimes: first, an increase of the force with the stiffness and then a saturation plateau for even larger stiffness. As the MSC cell migrates, the leading edge is exerting larger contractile forces compared to the cell body and trailing edge. Periodical cell force oscillations were observed during cell apoptosis process and the oscillation amplitude was found to scale with the fiber stiffness. The cell force measurement platform developed in this study provide an unique opportunity to investigate the "inside-out" cell forces –forces exerted by the cell to its surrounding, in an ECM mimicking environment. The stiffness of suspended nanofibers can be conveniently adjusted through changing the fiber diameters and the suspended length. The force resolution and spatial resolution can be further improved by reducing the fiber stiffness and fiber spacing.

Efforts were made in this study to extend the current STEP technique to inorganic fibers. Aligned TiO_2 nanofibers were prepared through the STEP combined sol-gel technique. By tuning the processing parameters, varied morphologies such as solid fiber, nanowire in microtubes, tube, and porous tube were achieved. These 1D TiO_2 structures are several centimeters long and could be conveniently manipulated into bundles, arrays and yarns. It turns out that the porous TiO_2

nanotubes demonstrate highest photo-catalytic activity, which is attributed to the high specific surface area.

The significant contributions from this research can be summarized as:

1 Development of isodiametric design space for nanofiber fabrications

The nanofibers obtained from the design space are smooth and uniform and have substantial length (at least several millimeters). By visual inspection on the design space, required molecular weight and solution concentration for a specific fiber diameters can be determined. The design space has developed for varied polymer species.

Both fiber surface and cross-section area morphologies can be tuned by adjusting solvent volatility and relative humidity

The STEP technique was combined with sol-gel technique to produce TiO_2 nanofibers.

2 Single nanofiber mechanical characterization

Fiber stiffness, modulus, tensile stress and strength were obtained by laterally deflecting the nanofibers.

Strength of sub 100nm diameter fibers have been characterized, which demonstrate a significant enhancement as fiber diameter reduces.

Strength distribution of single polymer nanofibers were obtained, which follows two parameter Weibull distribution. The strength distribution of single nanofibers was used to predict nanofiber yarn strength.

3 Hierarchical nanofiber assemblies as bio-scaffolds

Cell attachment and cell spread area can be controlled through the configuration of nanofiber scaffolds.

Cell force evolution during division, migration and apoptosis process can be accurately measured using suspended nanofibers as force sensors.

The contributions that would impact the progress of this ongoing research can be summarized as following:

1 It is of great interest to generate nanofiber scaffolds with stiffness gradients to control MSC cell differentiation. Bio-scaffolds with varied stiffness can be made from nanofibers with varied diameters (from 200nm to microns) and suspended length (from 50 μm to 1000 μm). In addition, different polymer species can be used to construct the nanofiber scaffolds, which further extend the stiffness ranges. For example, polyurethane can be used to prepare low stiffness scaffolds while PMMA can be used to prepare scaffolds with high stiffness. It is possible that MSC cells would preferentially differentiate into adipocytes on scaffolds made from small diameter fiber (dia<200nm) with long suspended length, while osteoblasts may be expected on scaffolds made from micron sized diameter fibers with short suspended length.

In addition, based on the current nanofiber net system, it is possible to detect the “outside-in” cell forces, which is the forces that a cell can tolerate from external perturbation. For example, by peel off a cell from fibers that it attached to, the cell adhesion force can be back calculated from the deflections of the fiber.

2 It will be helpful to prepare sub 100nm diameter nanofibers from crystalline polymer and characterize their mechanical properties. Significant polymer chain orientation may be achieved during fiber formation process for the sub 100nm diameter nanofibers, which could leads to superior modulus and strength. By controlling the crystallinity of the polymer through annealing process, it may be possible to tailor the mechanical properties of single polymer nanofibers. In addition, it would be interesting to extend the current mechanical characterization approach to inorganic nanofibers, such as TiO_2 nanofibers, which can be conveniently achieved using the STEP combined sol-gel process. Also, the current approach can be extended to investigate the mechanical properties of single nanofiber made from MWCNTs reinforced polymers.

3 More effort will be devoted to biological scaffolds made from biological polymers, such as collagen and spider silk. Following the same approach outlined in this study, it is possible to develop the isodiametric design space for these polymers and construct multilayer hierarchical fiber assemblies, which are both biophysically and biochemically similar to the *in vivo* ECM. Native ECM proteins have diameter ranging from 50nm (a single collagen fibril) to microns (collagen fiber bundle), which are well within the diameter range of STEP isodiametric design space. Concurrent effort will be devoted to develop hierarchical structures using the 50nm diameter fibers as building blocks—first construct microscale fiber bundles and then escalates to millimeter scale tissues, such as blood vessel and tendons.

4 It is of tremendous interest and importance to scale up the productions of STEP fibers. Efforts will be devoted to incorporate multiple spinnerets into the STEP technique. Since there is no electrical sources involved in STEP technique, there is no limits in the spinneret spacing, thus spinnerets can be densely packed to increase the production of the STEP fibers. Instead of collecting a single filament, it will be possible to collect fiber bundles or yarns directly. Also, it

will be helpful to obtain microscale fibers using melt spinning based on the STEP technique. With these microscale fibers, it will be convenient to construct 3D scaffolds on the order of millimeters in thickness, approaching the thickness of tissue structures.

Appendix A Overlap Concentration (C*) and Critical Entangled Concentration (Ce)

PS was dissolved in *p*-xylene at low concentrations ~ 1% by weight and dilute solution viscometry experiments on different molecular weights of PS (650K, 860K,1500K and 2000K g.mol^{-1}) were conducted to obtain the intrinsic viscosity $[\eta]$ and also the Mark-Houwink-Sakurada constants (K=0.0136 ml.g^{-1} and α=0.6920 at 30°C) [1].

Overlap concentration C* which lies at the boundary of dilute and semi-dilute (un-entangled) regions can be determined using the Mark-Houwink-Sakurada relation:

$$C^* = \frac{1}{[\eta]} = 1/KM_w{}^{\alpha} \qquad \text{[Eq A1]}$$

K and α (S1) are Mark-Houwink-Sakurada constants and M_w is molecular weight.

Critical entangled concentration C_e which lies at the boundary of semi-dilute (untangled) and semi-dilute (entangled) regions can be calculated from:

$$C_e = n^{(3\nu-1)}/M_w A_2 \qquad \text{[Eq A2]}$$

Where n is the number of monomers between entanglements and is defined as $n = M_e/m_o$, where M_e is the entanglement density of the melt (PS~13,309g.mol^{-1}),m_o is molecular weight of repeat unit , and ν is the excluded volume exponent calculated as: $\nu = (\alpha + 1)/3.$ [2]

With K and α being the Mark-Houwink-Sakurada constants obtained from dilute solution viscometry , $M_w A_2$ are calculated as [2]:

$$M_w A_2 = 5.3/C^* \qquad \text{[Eq A3]}$$

Both C* and C_e decrease with increasing molecular weights.

Rheology parameter values (C^*,C_e) for different molecular weight are summarized in Supplementary Table 1.

Table A1 Rheology parameter values for different molecular weight of PS. Wang et al, Polymer Journal, 2013, 45. Used with permission of Nature Publishing group, 2015.

	650k (g.mol^{-1})	**860k (g.mol^{-1})**	**1500k (g.mol^{-1})**	**2000k (g.mol^{-1})**
C*(mg/ml)	7.0	5.8	3.9	3.2
C_e (mg/ml)	96.1	55.2	26.7	17.3

Appendix B Estimation of solvent diffusion coefficient in polymer solution

Solvent diffusion coefficient varies considerably as a function of solution concentration. To estimate the solvent diffusion coefficient in different concentration solutions, solutions were placed in a petri dish and allowed to evaporate into air. The weight loss with time was recorded using an accurate balance.

The diffusion of solvent in the petri dish can be considered as a one-dimensional process, which is governed by Fick's Law[209]:

$$\frac{\partial \rho_s}{\partial t} - \frac{\partial}{\partial x}\left[\overline{\rho_p} \frac{D_{ss}}{(1-\frac{\overline{\rho_p}}{\overline{\rho_s}})\rho_s + \overline{\rho_p}} \frac{\partial \rho_s}{\partial x} \right] = 0$$

Where $\overline{\rho_p}$ is polymer density (1.05g/cm^3 for polystyrene), $\overline{\rho_s}$ is solvent density (0.91g/ cm^{3}for DMF/xylene =50:50,v/v), ρ_s is solvent concentration(by weight), D_{ss} is internal solvent diffusion coefficient(mm^2/s).

There are two boundary conditions:

1) $\rho_s = 0, x = L;$ solvent concentration is zero at the solution-air interface, where L is the solution thickness in the petri dish

2) $\frac{\partial \rho_s}{\partial x} = 0, x = 0;$ solvent concentration gradient is zero at the bottom of the petri dish

There are one initial condition:

$\rho_s = \rho_{s0}, t = 0;$ where ρ_{s0} is the initial solvent concentration.

the equation can be solved as: $\rho_s = \rho_s(t, x, D_{ss})$.

At time t, the total mass of the solution is:

$m_{calc} = \overline{\rho_s} A \int_0^L \rho_s dx + m_p$, where m_{calc} is the calculated total mass of the solution, A is the cross-section area of the petri dish, m_p is the polymer mass in the solution.

Therefore, the solution weight loss during any time is $m_{initial} - m_{calc}$, which is a function of D_{ss}.

By matching $m_{initial} - m_{calc}$ with the measured weight loss, D_{ss} was determined.

Table B1 Diffusion coefficient of solvent molecules in different concentration solutions for t=10 seconds. Wang et al, Polymer, 2014, 55. Used with permission of Elsevier publishing group, 2015.

Solution Concentration (%wt)	**Entanglements(C/C*)**	**Estimated $D_{ss}\times10^{-5}$ (mm^2/s)**
1	3	1.36
2	6	0.65
4	12	0.21
7	21	0.09
10	31	0.06

Appendix C Single Fiber Stiffness and Tension Scaling with Fiber Diameter

2M PS single fiber stiffness and tension scaling with fiber diameters

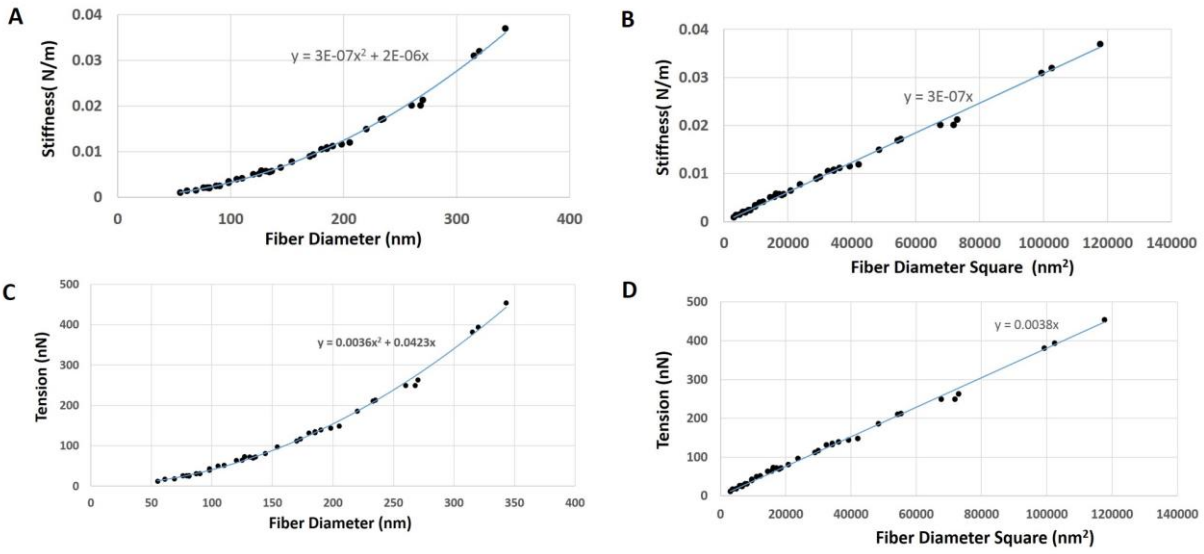

Figure C1 2M PS single fiber stiffness as a function of (A) fiber diameter and (B)fiber diameter square , and fiber tension as a function of (C) fiber diameter and (D) fiber diameter square.

860k PS single fiber stiffness and tension scaling with fiber diameters

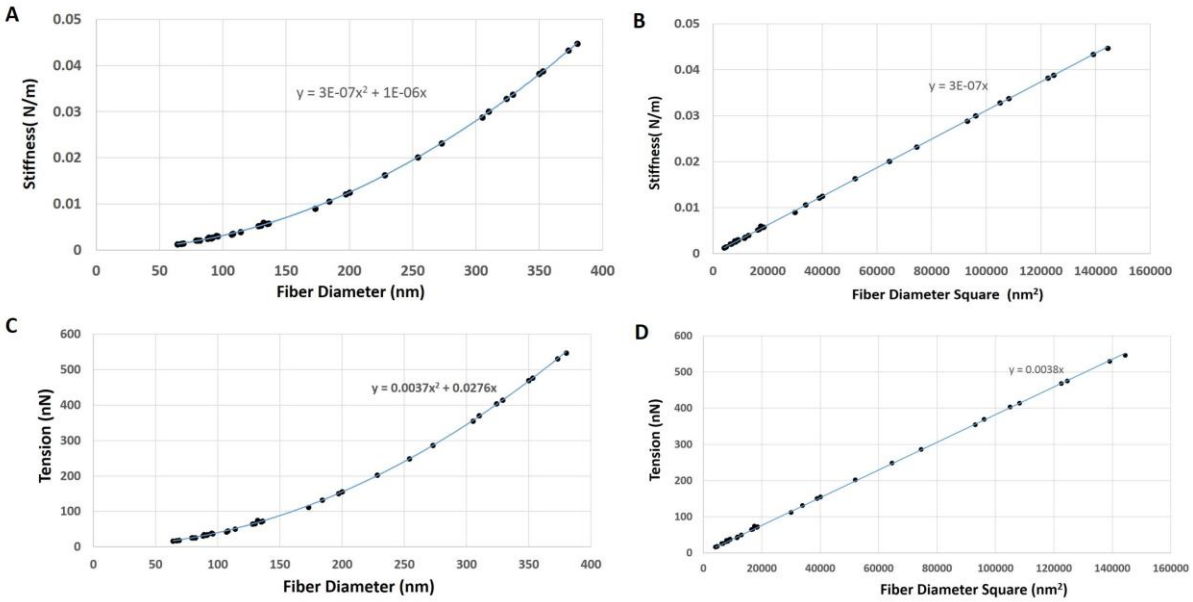

Figure C2 860k PS single fiber stiffness as a function of (A) fiber diameter and (B)fiber diameter square, and fiber tension as a function of (C) fiber diameter and (D) fiber diameter square.

400k PS single fiber stiffness and tension scaling with fiber diameters

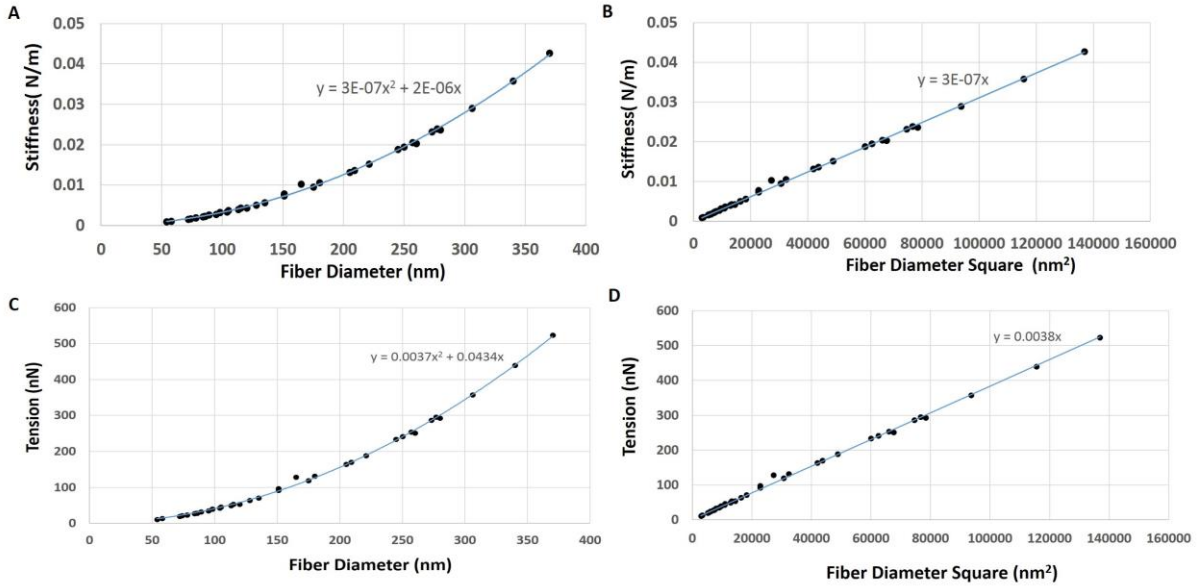

Figure C3 400k PS single fiber stiffness as a function of (A) fiber diameter and (B)fiber diameter square, and fiber tension as a function of (C) fiber diameter and (D) fiber diameter square.

Appendix D Force-displacement Curves and Mechanical Properties Summarization of PS Nanofibers

Table D1 Tensile Stress of PS Nanofibers

Strain Rate	Tensile Stress (MPa)		
	2M	860k	400k
120μm/s	4.35	4.12	4.25
10μm/s	4.51	4.65	4.45
2μm/s	3.95	4.07	4.00

2M PS nanofibers deformed at strain rate 120μm/s

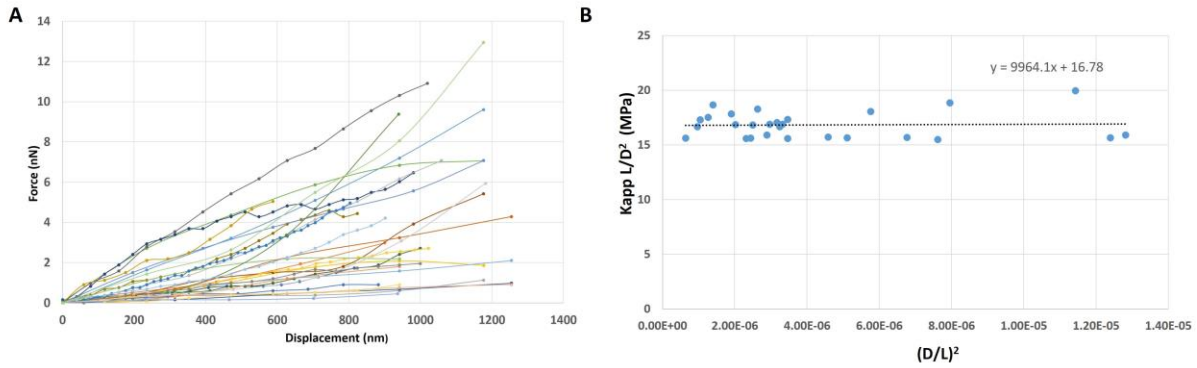

Figure D1 2M PS fiber defelected at strain rate 120μm/s. (A) Force-displacement curves. (B) Product of apparent stiffness k_{app} and L/D^2 of PS nanofibers as a function of $(D/L)^2$.

Slope (GPa)	Modulus(GPa)	Intercept(MPa)	Tensile Stress(MPa)
9.96	1.05	16.78	4.35

860k PS nanofibers deformed at rate 120μm/s

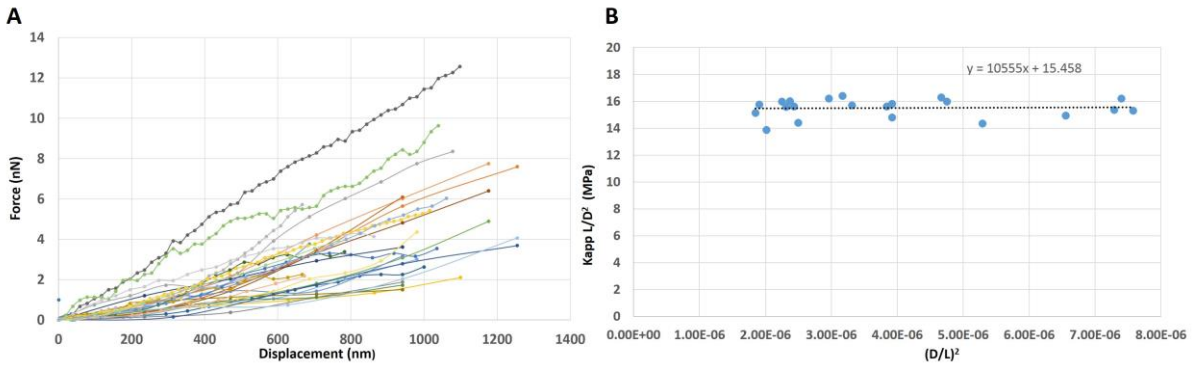

Figure D2 860k PS fiber defelected at strain rate 120μm/s. (A) Force-displacement curves. (B) Product of apparent stiffness k_{app} and L/D^2 of PS nanofibers as a function of $(D/L)^2$.

Slope (GPa)	Modulus(GPa)	Intercept(MPa)	Tensile Stress(MPa)
10.55	1.12	15.46	4.12

400k PS nanofibers deformed at strain rate 120μm/s

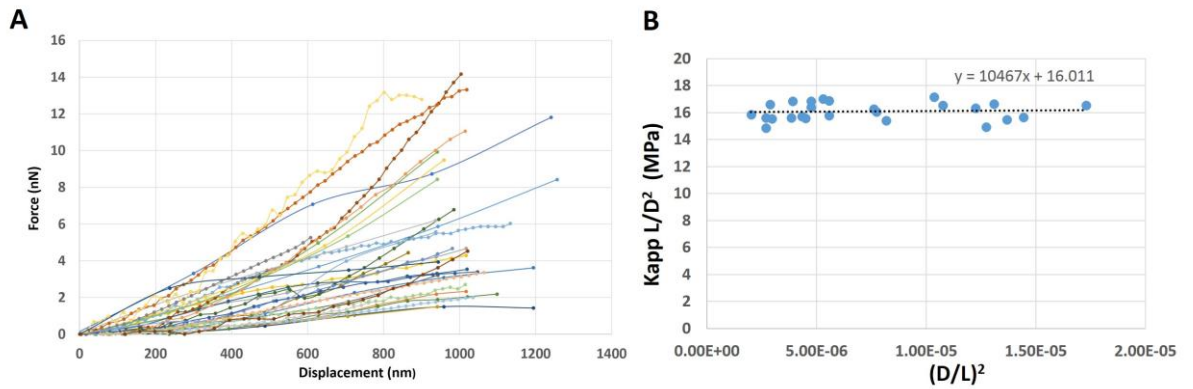

Figure D3 400k PS fiber defelected at strain rate 120μm/s. (A) Force-displacement curves. (B) Product of apparent stiffness k_{app} and L/D^2 of PS nanofibers as a function of $(D/L)^2$.

Slope (GPa)	Modulus(GPa)	Intercept(MPa)	Tensile Stress(MPa)
10.05	1.11	16.01	4.25

2M PS nanofibers deformed at strain rate 10μm/s

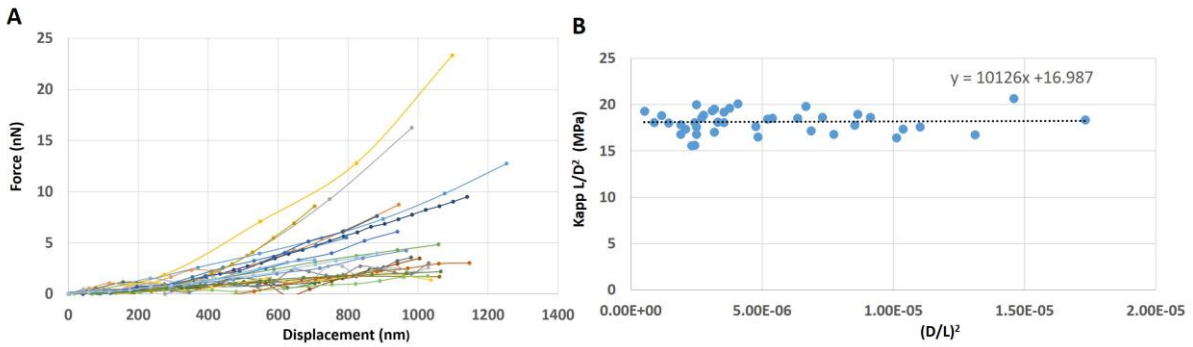

Figure D4 2M PS fiber defelected at strain rate 10μm/s. (A) Force-displacement curves. (B) Product of apparent stiffness k_{app} and L/D^2 of PS nanofibers as a function of $(D/L)^2$.

Slope (GPa)	Modulus(GPa)	Intercept(MPa)	Tensile Stress(MPa)
10.13	1.08	16.99	4.51

860k PS nanofibers deformed at strain rate 10μm/s

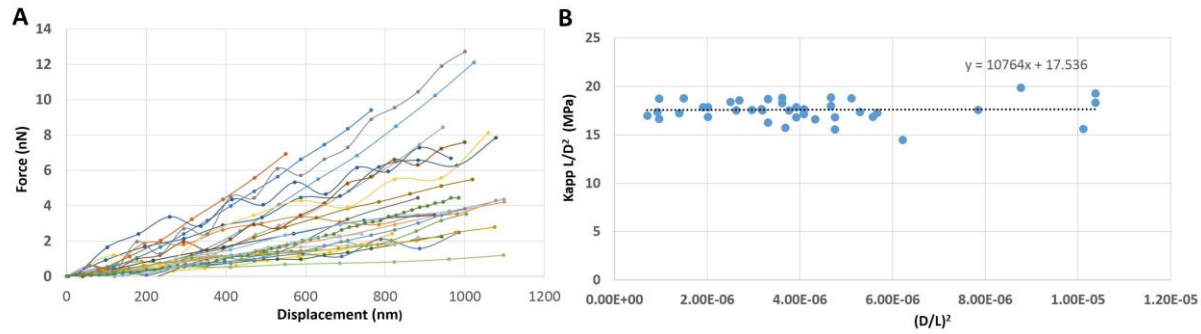

Figure D5 860k PS fiber defelected at strain rate 10μm/s. (A) Force-displacement curves. (B) Product of apparent stiffness k_{app} and L/D^2 of PS nanofibers as a function of $(D/L)^2$.

Slope (GPa)	Modulus(GPa)	Intercept(MPa)	Tensile Stress(MPa)
10.76	1.14	17.53	4.65

400k PS nanofibers deformed at strain rate 10μm/s

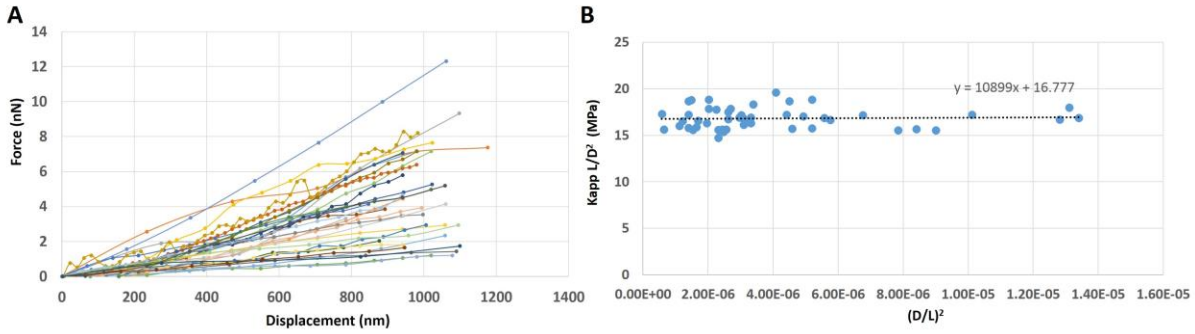

Figure D6 400k PS fiber defelected at strain rate 10μm/s. (A) Force-displacement curves. (B) Product of apparent stiffness k_{app} and L/D^2 of PS nanofibers as a function of $(D/L)^2$.

Slope (GPa)	Modulus(GPa)	Intercept(MPa)	Tensile Stress(MPa)
10.90	1.16	16.78	4.45

2M PS nanofibers deformed at strain rate 2μm/s

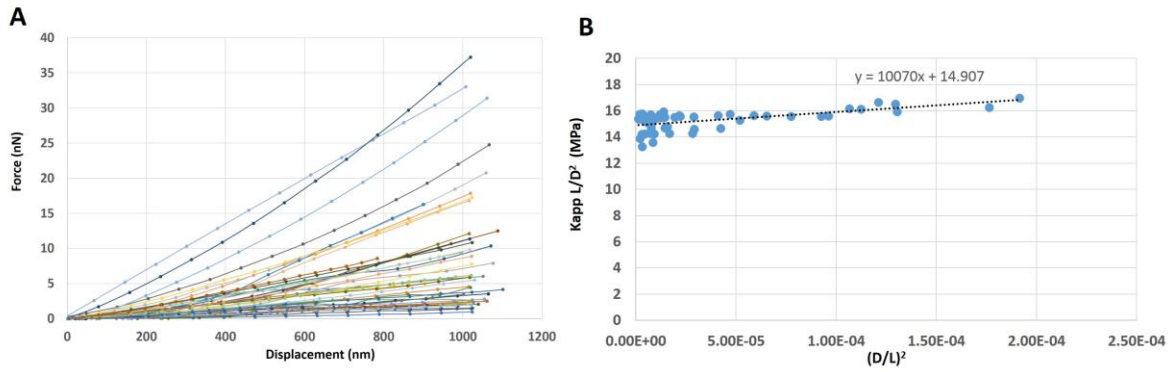

Figure D7 2M PS fiber defelected at strain rate 2μm/s. (A) Force-displacement curves. (B) Product of apparent stiffness k_{app} and L/D^2 of PS nanofibers as a function of $(D/L)^2$.

Slope (GPa)	Modulus(GPa)	Intercept(MPa)	Tensile Stress(MPa)
10.07	1.07	14.91	3.95

860k PS nanofibers deformed at strain rate 2μm/s

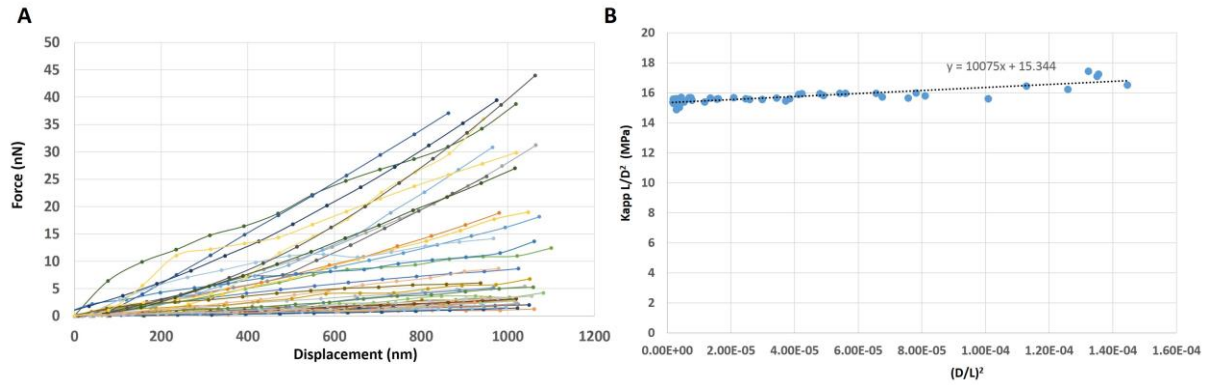

Figure D8 860k PS fiber defelected at strain rate 2μm/s. (A) Force-displacement curves. (B) Product of apparent stiffness k_{app} and L/D^2 of PS nanofibers as a function of $(D/L)^2$.

Slope (GPa)	Modulus(GPa)	Intercept(MPa)	Tensile Stress(MPa)
1.08	1.07	15.34	4.07

400k PS nanofibers deformed at strain rate 2μm/s

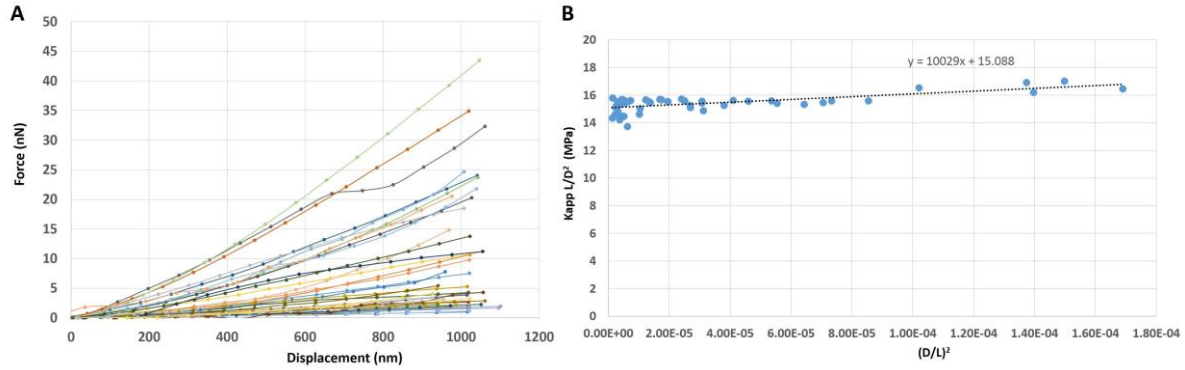

Figure D9 400k PS fiber defelected at strain rate 2μm/s. (A) Force-displacement curves. (B) Product of apparent stiffness k_{app} and L/D^2 of PS nanofibers as a function of $(D/L)^2$.

Slope (GPa)	Modulus(GPa)	Intercept(MPa)	Tensile Stress(MPa)
1.03	1.06	15.08	4.00

Appendix E The TG Curve of Precursor Fibers

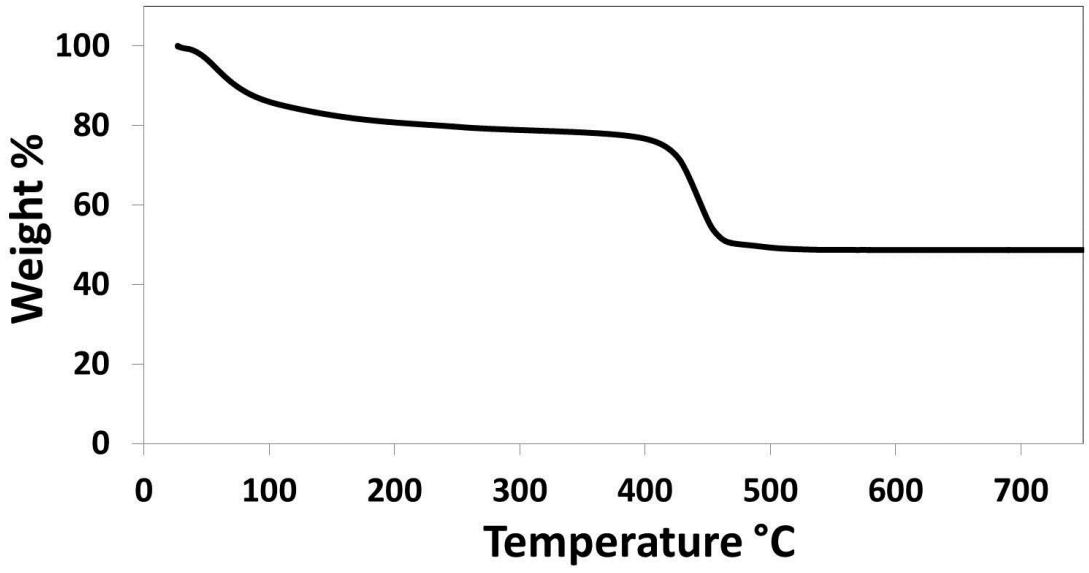

Figure E1 The TG Curve of Precusor Fibers. Wang et al, New Journal of Chemistry, 2013, 37. Used with permission of Royal Society of Chemistry, 2015.

Appendix F Comparison of Photocatalytic Activity of Titania Nanostructures

Table F1 Comparison of the photo degradation rate constants of varied titania nanostructures with the commercial TiO_2 powder P25. Aeroxide® P25 (Evonik Degussa, GmbH). Wang et al, New Journal of Chemistry, 2013, 37. Used with permission of Royal Society of Chemistry, 2015.

TiO2	Catalyst Conc	Initial MB Conc	Reaction condition	Rate constant	Source
Nanofiber	100mg/L	10mg/L	160W Hg Lamp	0.007 min^{-1}	This work
NW@MT	100mg/L	10mg/L	160W Hg Lamp	0.016 min^{-1}	This work
Tubes	100mg/L	10mg/L	160W Hg Lamp	0.024 min^{-1}	This work
Porous Tubes	100mg/L	10mg/L	160W Hg Lamp	0.029 min^{-1}	This work
P25 Degussa	240mg/L	25mg/L	400W Hg Lamp	0.015 min^{-1}	[210]
P25 Degussa	300mg/L	10mg/L	8W UV Lamp	0.008 min^{-1}	[211]
P25 Degussa	100mg/L	32mg/L	75 W Hg Lamp	0.012 min^{-1}	[212]

References:

[1] Nain AS. Polymeric Micro/Nanofibers: Fabrication, Aligned Deposition, Mechanical Characterization, and Biological Applications, PhD Dissertation, Mechanical Engineering, Carnegie Mellon University 2007.

[2] Nain AS, Sitti M, Jacobson A, Kowalewski T, Amon C. Dry Spinning Based Spinneret Based Tunable Engineered Parameters (STEP) Technique for Controlled and Aligned Deposition of Polymeric Nanofibers. Macromol Rapid Commun 2009;30:1406–12. doi:10.1002/marc.200900204.

[3] Nain AS, Phillippi JA, Sitti M, Mackrell J, Campbell PG, Amon C. Control of cell behavior by aligned micro/nanofibrous biomaterial scaffolds fabricated by spinneret-based tunable engineered parameters (STEP) technique. Small 2008;4:1153–9. doi:10.1002/smll.200800101.

[4] Pham QP, Sharma U, Mikos AG. Electrospinning of polymeric nanofibers for tissue engineering applications: a review. Tissue Eng 2006;12:1197–211. doi:10.1089/ten.2006.12.1197.

[5] Greiner A, Wendorff JH. Electrospinning: a fascinating method for the preparation of ultrathin fibers. Angew Chem Int Ed Engl 2007;46:5670–703. doi:10.1002/anie.200604646.

[6] Venugopal J, Ma LL, Yong T, Ramakrishna S. In vitro study of smooth muscle cells on polycaprolactone and collagen nanofibrous matrices. Cell Biol Int 2005;29:861–7. doi:10.1016/j.cellbi.2005.03.026.

[7] Mo X., Xu C., Kotaki M, Ramakrishna S. Electrospun P(LLA-CL) nanofiber: a biomimetic extracellular matrix for smooth muscle cell and endothelial cell proliferation. Biomaterials 2004;25:1883–90. doi:10.1016/j.biomaterials.2003.08.042.

[8] Prabhakaran MP, Venugopal J, Kai D, Ramakrishna S. Biomimetic material strategies for cardiac tissue engineering. Mater Sci Eng C 2011;31:503–13. doi:10.1016/j.msec.2010.12.017.

[9] Yang F, Murugan R, Wang S, Ramakrishna S. Electrospinning of nano / micro scale poly (L -lactic acid) aligned fibers and their potential in neural tissue engineering. Biomaterials 2005;26:2603–10. doi:10.1016/j.biomaterials.2004.06.051.

[10] Yin Z, Chen X, Chen JL, Shen WL, Hieu Nguyen TM, Gao L, et al. The regulation of tendon stem cell differentiation by the alignment of nanofibers. Biomaterials 2010;31:2163–75. doi:10.1016/j.biomaterials.2009.11.083.

[11] Lee CH, Shin HJ, Cho IH, Kang Y-M, Kim IA, Park K-D, et al. Nanofiber alignment and direction of mechanical strain affect the ECM production of human ACL fibroblast. Biomaterials 2005;26:1261–70. doi:10.1016/j.biomaterials.2004.04.037.

[12] Li X, Xie J, Lipner J, Yuan X, Thomopoulos S, Xia Y. Nanofiber scaffolds with gradations in mineral content for mimicking the tendon-to-bone insertion site. Nano Lett 2009;9:2763–8. doi:10.1021/nl901582f.

[13] Nain AS, Phillippi J a, Sitti M, Mackrell J, Campbell PG, Amon C. Control of cell behavior by aligned micro/nanofibrous biomaterial scaffolds fabricated by spinneret-based tunable engineered parameters (STEP) technique. Small 2008;4:1153–9. doi:10.1002/smll.200800101.

[14] Bakhru S, Nain AS, Highley C, Wang J, Campbell P, Amon C, et al. Direct and cell signaling-based, geometry-induced neuronal differentiation of neural stem cells. Integr Biol (Camb) 2011:1207–14. doi:10.1039/c1ib00098e.

[15] Sheets K, Wunsch S, Ng C, Nain AS. Shape-dependent cell migration and focal adhesion organization on suspended and aligned nanofiber scaffolds. Acta Biomater 2013;9:7169–77. doi:10.1016/j.actbio.2013.03.042.

[16] Sharma P, Sheets K, Elankumaran S, Nain AS. The mechanistic influence of aligned nanofibers on cell shape, migration and blebbing dynamics of glioma cells. Integr Biol (Camb) 2013;5:1036–44. doi:10.1039/c3ib40073e.

[17] Meehan S, Nain AS. Role of Suspended Fiber Structural Stiffness and Curvature on Single Cell Migration, Nucleus Shape, and Focal Adhesion Cluster Length. Biophys J 2014;In Press.

[18] Sharma P, Kim A, Gill A, Wang J, Sheets K, Behkam B, et al. Aligned and suspended fiber force probes for drug testing at single cell resolution. Biofabrication 2014;6:045006. doi:10.1088/1758-5082/6/4/045006.

[19] Wang J, Nain AS. Suspended micro/nanofiber hierarchical biological scaffolds fabricated using non-electrospinning STEP technique. Langmuir 2014;30:13641–9. doi:10.1021/la503011u.

[20] Ma M, Gupta M, Li Z, Zhai L, Gleason KK, Cohen RE, et al. Decorated Electrospun Fibers Exhibiting Superhydrophobicity. Adv Mater 2007;19:255–9. doi:10.1002/adma.200601449.

[21] Jiang L, Zhao Y, Zhai J. A Lotus-Leaf-like Superhydrophobic Surface: A Porous Microsphere/Nanofiber Composite Film Prepared by Electrohydrodynamics. Angew Chemie 2004;116:4438–41. doi:10.1002/ange.200460333.

[22] Acatay K, Simsek E, Ow-Yang C, Menceloglu YZ. Tunable, superhydrophobically stable polymeric surfaces by electrospinning. Angew Chem Int Ed Engl 2004;43:5210–3. doi:10.1002/anie.200461092.

[23] Ma M, Hill RM, Lowery JL, Fridrikh S V, Rutledge GC. Electrospun poly(styrene-block-dimethylsiloxane) block copolymer fibers exhibiting superhydrophobicity. Langmuir 2005;21:5549–54. doi:10.1021/la047064y.

[24] Ma M, Mao Y, Gupta M, Gleason KK, Rutledge GC. Superhydrophobic Fabrics Produced by Electrospinning and Chemical Vapor Deposition. Macromolecules 2005;38:9742–8. doi:10.1021/ma0511189.

[25] Wu H, Zhang R, Sun Y, Lin D, Sun Z, Pan W, et al. Biomimetic nanofiber patterns with controlled wettability. Soft Matter 2008;4:2429. doi:10.1039/b805570j.

[26] Nanofibers P, Feng L, Li S, Li H, Zhai J. Super-Hydrophobic Surface of Aligned 2002:1269–71.

[27] Lee W, Jin M-K, Yoo W-C, Lee J-K. Nanostructuring of a polymeric substrate with well-defined nanometer-scale topography and tailored surface wettability. Langmuir 2004;20:7665–9. doi:10.1021/la049411+.

[28] Kargar M, Wang J, Nain AS, Behkam B. Controlling bacterial adhesion to surfaces using topographical cues: a study of the interaction of Pseudomonas aeruginosa with nanofiber-textured surfaces. Soft Matter 2012;8:10254. doi:10.1039/c2sm26368h.

[29] Fennessey SF, Farris RJ. Fabrication of aligned and molecularly oriented electrospun polyacrylonitrile nanofibers and the mechanical behavior of their twisted yarns. Polymer (Guildf) 2004;45:4217–25. doi:10.1016/j.polymer.2004.04.001.

[30] Wang X, Zhang K, Zhu M, Yu H, Zhou Z, Chen Y, et al. Continuous polymer nanofiber yarns prepared by self-bundling electrospinning method. Polymer (Guildf) 2008;49:2755–61. doi:10.1016/j.polymer.2008.04.015.

[31] Li X, Yao C, Sun F, Song T, Li Y, Pu Y. Conjugate electrospinning of continuous nanofiber yarn of poly(L-lactide)/nanotricalcium phosphate nanocomposite. J Appl Polym Sci 2008;107:3756–64. doi:10.1002/app.27524.

[32] Ko F, Gogotsi Y, Ali A, Naguib N, Ye H, Yang GL, et al. Electrospinning of Continuous Carbon Nanotube-Filled Nanofiber Yarns. Adv Mater 2003;15:1161–5. doi:10.1002/adma.200304955.

[33] Li XH, Shao CL, Liu YC. A simple method for controllable preparation of polymer nanotubes via a single capillary electrospinning. Langmuir 2007;23:10920–3. doi:10.1021/la701806f.

[34] Katta P, Alessandro M, Ramsier RD, Chase GG. Continuous Electrospinning of Aligned Polymer Nanofibers onto a Wire Drum Collector. Nano Lett 2004;4:2215–8. doi:10.1021/nl0486158.

[35] Xie J, MacEwan MR, Schwartz AG, Xia Y. Electrospun nanofibers for neural tissue engineering. Nanoscale 2010;2:35–44. doi:10.1039/b9nr00243j.

[36] Kessick R, Tepper G. Electrospun polymer composite fiber arrays for the detection and identification of volatile organic compounds. Sensors Actuators B Chem 2006;117:205–10. doi:10.1016/j.snb.2005.11.045.

[37] Li D, Ouyang G, McCann JT, Xia Y. Collecting Electrospun Nanofibers with Patterned Electrodes. Nano Lett 2005;5:913–6. doi:10.1021/nl0504235.

[38] Li D, Wang Y, Xia Y. Electrospinning of Polymeric and Ceramic Nanofibers as Uniaxially Aligned Arrays. Nano Lett 2003;3:1167–71. doi:10.1021/nl0344256.

[39] Shalumon KT, Sathish D, Nair S V., Chennazhi KP, Tamura H, Jayakumar R. Fabrication of Aligned Poly(Lactic Acid)-Chitosan Nanofibers by Novel Parallel Blade Collector Method for Skin Tissue Engineering. J Biomed Nanotechnol 2012;8:405–16. doi:10.1166/jbn.2012.1395.

[40] Dalton PD, Joergensen NT, Groll J, Moeller M. Patterned melt electrospun substrates for tissue engineering. Biomed Mater 2008;3:034109. doi:10.1088/1748-6041/3/3/034109.

[41] Bisht GS, Canton G, Mirsepassi A, Kulinsky L, Oh S, Dunn-Rankin D, et al. Controlled continuous patterning of polymeric nanofibers on three-dimensional substrates using low-voltage near-field electrospinning. Nano Lett 2011;11:1831–7. doi:10.1021/nl2006164.

[42] Sun D, Chang C, Li S, Lin L. Near-field electrospinning. Nano Lett 2006;6:839–42. doi:10.1021/nl0602701.

[43] Harfenist SA, Cambron SD, Nelson EW, Berry SM, Isham AW, Crain MM, et al. Direct Drawing of Suspended Filamentary Micro- and Nanostructures from Liquid Polymers. Nano Lett 2004;4:1931–7. doi:10.1021/nl048919u.

[44] Nain AS, Wong JC, Amon C, Sitti M. Drawing suspended polymer micro-/nanofibers using glass micropipettes. Appl Phys Lett 2006;89:183105.

[45] Nain AS, Amon C, Sitti M. Proximal Probes Based Nanorobotic Drawing of Polymer Micro/Nanofibers. IEEE Trans Nanotechnol 2006;5:499–510.

[46] Casper CL, Stephens JS, Tassi NG, Chase DB, Rabolt JF. Controlling Surface Morphology of Electrospun Polystyrene Fibers: Effect of Humidity and Molecular Weight in the Electrospinning Process. Macromolecules 2004;37:573–8. doi:10.1021/ma0351975.

[47] Kongkhlang T, Kotaki M, Kousaka Y, Umemura T, Nakaya D, Chirachanchai S. Electrospun Polyoxymethylene: Spinning Conditions and Its Consequent Nanoporous Nanofiber. Macromolecules 2008;41:4746–52. doi:10.1021/ma800731r.

[48] Megelski S, Stephens JS, Chase DB, Rabolt JF. Micro- and Nanostructured Surface Morphology on Electrospun Polymer Fibers. Macromolecules 2002;35:8456–66. doi:10.1021/ma020444a.

[49] Bognitzki M, Czado W, Frese T, Schaper a., Hellwig M, Steinhart M, et al. Nanostructured Fibers via Electrospinning. Adv Mater 2001;13:70–2. doi:10.1002/1521-4095(200101)13:1<70::AID-ADMA70>3.0.CO;2-H.

[50] Dayal P, Liu J, Kumar S, Kyu T. Experimental and Theoretical Investigations of Porous Structure Formation in Electrospun Fibers. Macromolecules 2007;40:7689–94. doi:10.1021/ma071418l.

[51] Evans E, Bowman H, Leung A, Needham D, Tirrell D. Biomembrane Templates for Nanoscale Conduits and Networks. Science (80-) 1996;273:933–5. doi:10.1126/science.273.5277.933.

[52] Niwa Si S, Eswaramoorthy M, Nair J, Raj A, Itoh N, Shoji H, et al. A one-step conversion of benzene to phenol with a palladium membrane. Science 2002;295:105–7. doi:10.1126/science.1066527.

[53] Mayya KS, Gittins DI, Dibaj AM, Caruso F. Nanotubes Prepared by Templating Sacrificial Nickel Nanorods. Nano Lett 2001;1:727–30. doi:10.1021/nl015622c.

[54] Song L, Hobaugh MR, Shustak C, Cheley S, Bayley H, Gouaux JE. Structure of Staphylococcal alpha -Hemolysin, a Heptameric Transmembrane Pore. Science (80-) 1996;274:1859–65. doi:10.1126/science.274.5294.1859.

[55] Ketchem R, Hu W, Cross T. High-resolution conformation of gramicidin A in a lipid bilayer by solid-state NMR. Science (80-) 1993;261:1457–60. doi:10.1126/science.7690158.

[56] Caruso RA, Schattka JH, Greiner A. Titanium Dioxide Tubes from Sol–Gel Coating of Electrospun Polymer Fibers. Adv Mater 2001;13:1577. doi:10.1002/1521-4095(200110)13:20<1577::AID-ADMA1577>3.0.CO;2-S.

[57] Kim G-M, Lee S-M, Michler GH, Roggendorf H, Gösele U, Knez M. Nanostructured Pure Anatase Titania Tubes Replicated from Electrospun Polymer Fiber Templates by Atomic Layer Deposition. Chem Mater 2008;20:3085–91. doi:10.1021/cm703398b.

[58] Dror Y, Salalha W, Avrahami R, Zussman E, Yarin AL, Dersch R, et al. One-step production of polymeric microtubes by co-electrospinning. Small 2007;3:1064–73. doi:10.1002/smll.200600536.

[59] Bazilevsky A V, Yarin AL, Megaridis CM. Co-electrospinning of core-shell fibers using a single-nozzle technique. Langmuir 2007;23:2311–4. doi:10.1021/la063194q.

[60] Li D, Xia Y. Direct Fabrication of Composite and Ceramic Hollow Nanofibers by Electrospinning. Nano Lett 2004;4:933–8. doi:10.1021/nl049590f.

[61] Tan EPS, Lim CT. Physical properties of a single polymeric nanofiber. Appl Phys Lett 2004;84:1603. doi:10.1063/1.1651643.

[62] Lee S-H, Tekmen C, Sigmund WM. Three-point bending of electrospun TiO2 nanofibers. Mater Sci Eng A 2005;398:77–81. doi:10.1016/j.msea.2005.03.014.

[63] Yu M. Strength and Breaking Mechanism of Multiwalled Carbon Nanotubes Under Tensile Load. Science (80-) 2000;287:637–40. doi:10.1126/science.287.5453.637.

[64] Nain AS. Polymeric Micro/Nanofibers: Fabrication, Aligend Deposition, Mechanical Characterization, and Biological Applications. PhD Diss Mech Eng , 2007.

[65] Nanjundappa R, Bhat GS. Effect of processing conditions on the structure and properties of polypropylene spunbond fabrics. J Appl Polym Sci 2005;98:2355–64. doi:10.1002/app.22148.

[66] A.B.Ariawan S. K. Goyal, H.Hay, SGH. No Title. Adv Polym Technol 2001;20.

[67] Zhao R (Rongguo), Wadsworth LC. Study of polypropylene/poly(ethylene terephthalate) bicomponent melt-blowing process: The fiber temperature and elongational viscosity profiles of the spinline. J Appl Polym Sci 2003;89:1145–50. doi:10.1002/app.12321.

[68] Rwei S-P, Jue Z-F, Chen FL. PBT/PET conjugated fibers: Melt spinning, fiber properties, and thermal bonding. Polym Eng Sci 2004;44:331–44. doi:10.1002/pen.20030.

[69] Suzuki A, Kishi M. Preparation of poly(ethylene terephthalate) nonwoven fabric from endless microfibers obtained by CO2 laser-thinning method. Polymer (Guildf) 2007;48:2729–36. doi:10.1016/j.polymer.2007.03.028.

[70] Heo Y, Larson RG. The scaling of zero-shear viscosities of semidilute polymer solutions with concentration. J Rheol (N Y N Y) 2005;49:1117. doi:10.1122/1.1993595.

[71] Dees JR, Spruiell JE. Structure development during melt spinning of linear polyethylene fibers. J Appl Polym Sci 1974;18:1053–78. doi:10.1002/app.1974.070180408.

[72] Viswanathamurthi P, Bhattarai N, Kim HY, Lee DR, Kim SR, Morris MA. Preparation and morphology of niobium oxide fibres by electrospinning. Chem Phys Lett 2003;374:79–84. doi:http://dx.doi.org/10.1016/S0009-2614(03)00702-4.

[73] Cepak VM, Martin CR. Preparation of Polymeric Micro- and Nanostructures Using a Template-Based Deposition Method. Chem Mater 1999;11:1363–7. doi:10.1021/cm9811500.

[74] Hou S, Harrell CC, Trofin L, Kohli P, Martin CR. Layer-by-Layer Nanotube Template Synthesis. J Am Chem Soc 2004;126:5674–5. doi:10.1021/ja049537t.

[75] Steinhart M, Jia Z, Schaper AK, Wehrspohn RB, Gösele U, Wendorff JH. Palladium Nanotubes with Tailored Wall Morphologies. Adv Mater 2003;15:706–9. doi:10.1002/adma.200304502.

[76] Klug A. From Macromolecules to Biological Assemblies(Nobel Lecture). Angew Chemie Int Ed English 1983;22:565–82. doi:10.1002/anie.198305653.

[77] Bognitzki M, Hou H, Ishaque M, Frese T, Hellwig M, Schwarte C, et al. Polymer, Metal, and Hybrid Nano- and Mesotubes by Coating Degradable Polymer Template Fibers (TUFT Process). Adv Mater 2000;12:637–40. doi:10.1002/(SICI)1521-4095(200005)12:9<637::AID-ADMA637>3.0.CO;2-W.

[78] Zussman E, Yarin AL, Bazilevsky AV, Avrahami R, Feldman M. Electrospun Polyaniline/Poly(methyl methacrylate)-Derived Turbostratic Carbon Micro-/Nanotubes. Adv Mater 2006;18:348–53. doi:10.1002/adma.200501153.

[79] Family F, Meakin P. Scaling of the Droplet-Size Distribution in Vapor-Deposited Thin Films. Phys Rev Lett 1988;61:428–31. doi:10.1103/PhysRevLett.61.428.

[80] Paul DR. Diffusion during the coagulation step of wet-spinning. J Appl Polym Sci 1968;12:383–402. doi:10.1002/app.1968.070120301.

[81] Ondarçuhu T, Joachim C. Drawing a single nanofibre over hundreds of microns. Europhys Lett 1998;42:215–20. doi:10.1209/epl/i1998-00233-9.

[82] Timoshenko SP, Gere JM. Theory of Elastic Stability (Google eBook). Courier Dover Publications; 2012.

[83] Guenthner AJ, Khombhongse S, Liu W, Dayal P, Reneker DH, Kyu T. Dynamics of Hollow Nanofiber Formation During Solidification Subjected to Solvent Evaporation. Macromol Theory Simulations 2006;15:87–93. doi:10.1002/mats.200500034.

[84] Koombhongse S, Liu W, Reneker DH. Flat polymer ribbons and other shapes by electrospinning. J Polym Sci Part B Polym Phys 2001;39:2598–606. doi:10.1002/polb.10015.

[85] Wang L, Pai C-L, Boyce MC, Rutledge GC. Wrinkled surface topographies of electrospun polymer fibers. Appl Phys Lett 2009;94:151916. doi:10.1063/1.3118526.

[86] P.Dayal S.Kumar,T.Kyu JL. No Title. Macromolecules 2007;40:7689.

[87] Cheryl L.Casper Nancy G.Tassi, D.Bruce Chase, John F.Rabolt JSS. No Title. Macromolecules 2004;37.

[88] S.Megelski D.B.Chase, J.F.Rabolt JSS. No Title. Macromolecules 2002;35:8456.

[89] Xu H, Melle S, Golemanov K, Fuller G. Shape and buckling transitions in solid-stabilized drops. Langmuir 2005;21:10016–20. doi:10.1021/la0507378.

[90] Tsapis N, Dufresne E, Sinha S, Riera C, Hutchinson J, Mahadevan L, et al. Onset of Buckling in Drying Droplets of Colloidal Suspensions. Phys Rev Lett 2005;94:018302. doi:10.1103/PhysRevLett.94.018302.

[91] Yoshimoto H, Shin YM, Terai H, Vacanti JP. A biodegradable nanofiber scaffold by electrospinning and its potential for bone tissue engineering. Biomaterials 2003;24:2077–82. doi:10.1016/S0142-9612(02)00635-X.

[92] Barnes CP, Sell SA, Boland ED, Simpson DG, Bowlin GL. Nanofiber technology: designing the next generation of tissue engineering scaffolds. Adv Drug Deliv Rev 2007;59:1413–33. doi:10.1016/j.addr.2007.04.022.

[93] Lin J, Ding B, Yang J, Yu J, Sun G. Subtle regulation of the micro- and nanostructures of electrospun polystyrene fibers and their application in oil absorption. Nanoscale 2012;4:176–82. doi:10.1039/c1nr10895f.

[94] Wu J, Wang N, Wang L, Dong H, Zhao Y, Jiang L. Electrospun porous structure fibrous film with high oil adsorption capacity. ACS Appl Mater Interfaces 2012;4:3207–12. doi:10.1021/am300544d.

[95] Wang J, Hou J, Marquez E, Moore RB, Nain AS. Aligned assembly of nano and microscale polystyrene tubes with controlled morphology. Polymer (Guildf) 2014. doi:10.1016/j.polymer.2014.04.046.

[96] Yang D, Liu H, Zheng Z, Yuan Y, Zhao J-C, Waclawik ER, et al. An efficient photocatalyst structure: TiO(2)(B) nanofibers with a shell of anatase nanocrystals. J Am Chem Soc 2009;131:17885–93. doi:10.1021/ja906774k.

[97] Wang J, Hou J, Ellis MW, Nain AS. Organized long titanium dioxide nanofibers/nanotubes with controlled morphology using a sol–gel combined STEP technique. New J Chem 2013;37:571. doi:10.1039/c2nj40886d.

[98] Tan EPS, Lim CT. Novel approach to tensile testing of micro- and nanoscale fibers. Rev Sci Instrum 2004;75:2581–5. doi:10.1063/1.1775309.

[99] Liu L-Q, Tasis D, Prato M, Wagner HD. Tensile Mechanics of Electrospun Multiwalled Nanotube/Poly(methyl methacrylate) Nanofibers. Adv Mater 2007;19:1228–33. doi:10.1002/adma.200602226.

[100] Tan EPS, Goh CN, Sow CH, Lim CT. Tensile test of a single nanofiber using an atomic force microscope tip. Appl Phys Lett 2005;86:073115. doi:10.1063/1.1862337.

[101] Yu M, Dyer MJ, Skidmore GD, Rohrs HW, Lu X, Ausman KD, et al. Three-dimensional manipulation of carbon nanotubes under a scanning electron microscope. Nanotechnology 1999;10:244–52. doi:10.1088/0957-4484/10/3/304.

[102] Wong S-C, Baji A, Leng S. Effect of fiber diameter on tensile properties of electrospun poly(ε-caprolactone). Polymer (Guildf) 2008;49:4713–22. doi:10.1016/j.polymer.2008.08.022.

[103] Tan EPS, Ng SY, Lim CT. Tensile testing of a single ultrafine polymeric fiber. Biomaterials 2005;26:1453–6. doi:10.1016/j.biomaterials.2004.05.021.

[104] Salvetat J-P, Briggs G, Bonard J-M, Bacsa R, Kulik A, Stöckli T, et al. Elastic and Shear Moduli of Single-Walled Carbon Nanotube Ropes. Phys Rev Lett 1999;82:944–7. doi:10.1103/PhysRevLett.82.944.

[105] Tombler T, Zhou C, Alexseyev L, Kong J, Dai H, Liu L, et al. Reversible electromechanical characteristics of carbon nanotubes under local-probe manipulation. Nature 2000;405:769–72. doi:10.1038/35015519.

[106] Cuenot S, Demoustier-Champagne S, Nysten B. Elastic Modulus of Polypyrrole Nanotubes. Phys Rev Lett 2000;85:1690–3. doi:10.1103/PhysRevLett.85.1690.

[107] DUVAIL JL, RETHO P, GODON C, MARHIC C, LOUARN G, CHAUVET O, et al. Physical properties of conducting polymer nanofibers. Synth Met n.d.;135-36:329–30.

[108] Yang L, Fitié CFC, van der Werf KO, Bennink ML, Dijkstra PJ, Feijen J. Mechanical properties of single electrospun collagen type I fibers. Biomaterials 2008;29:955–62. doi:10.1016/j.biomaterials.2007.10.058.

[109] Yang L, Fitié CFC, van der Werf KO, Bennink ML, Dijkstra PJ, Feijen J. Mechanical properties of single electrospun collagen type I fibers. Biomaterials 2008;29:955–62. doi:10.1016/j.biomaterials.2007.10.058.

[110] Ding Y, Zhang P, Jiang Y, Xu F, Yin J, Zuo Y. Mechanical properties of nylon-6/SiO2 nanofibers prepared by electrospinning. Mater Lett 2009;63:34–6. doi:10.1016/j.matlet.2008.08.058.

[111] Namazu T, Isono Y, Tanaka T. Plastic deformation of nanometric single crystal silicon wire in AFM bending test at intermediate temperatures. J Microelectromechanical Syst 2002;11:125–35. doi:10.1109/84.993447.

[112] Namazu T, Isono Y. Quasi-static bending test of nano-scale SiO2 wire at intermediate temperatures using AFM-based technique. Sensors Actuators A Phys 2003;104:78–85. doi:10.1016/S0924-4247(02)00431-4.

[113] Li X, Gao H, Murphy CJ, Caswell KK. Nanoindentation of Silver Nanowires. Nano Lett 2003;3:1495–8. doi:10.1021/nl034525b.

[114] Wang M, Jin H-J, Kaplan DL, Rutledge GC. Mechanical Properties of Electrospun Silk Fibers. Macromolecules 2004;37:6856–64. doi:10.1021/ma048988v.

[115] Chen YQ, Zheng XJ, Mao SX, Li W. Nanoscale mechanical behavior of vanadium doped ZnO piezoelectric nanofiber by nanoindentation technique. J Appl Phys 2010;107:094302. doi:10.1063/1.3402937.

[116] Chen X, Xu Z-H, Li X, Shaibat M a, Ishii Y, Ruoff RS. Structural and mechanical characterization of platelet graphite nanofibers. Carbon N Y 2007;45:416–23. doi:10.1016/j.carbon.2006.08.025.

[117] Domke J, Radmacher M. Measuring the Elastic Properties of Thin Polymer Films with the Atomic Force Microscope. Langmuir 1998;14:3320–5. doi:10.1021/la9713006.

[118] Park JG, Lee SH, Kim B, Park YW. Electrical resistivity of polypyrrole nanotube measured by conductive scanning probe microscope: The role of contact force. Appl Phys Lett 2002;81:4625. doi:10.1063/1.1528281.

[119] Tan EPS, Lim CT. Nanoindentation study of nanofibers. Appl Phys Lett 2005;87:123106. doi:10.1063/1.2051802.

[120] Yuya P a., Wen Y, Turner J a., Dzenis Y a., Li Z. Determination of Young's modulus of individual electrospun nanofibers by microcantilever vibration method. Appl Phys Lett 2007;90:111909. doi:10.1063/1.2713128.

[121] Zussman E, Chen X, Ding W, Calabri L, Dikin DA, Quintana JP, et al. Mechanical and structural characterization of electrospun PAN-derived carbon nanofibers. Carbon N Y 2005;43:2175–85.

[122] Arinstein A, Burman M, Gendelman O, Zussman E. Effect of supramolecular structure on polymer nanofibre elasticity. Nat Nanotechnol 2007;2:59–62. doi:10.1038/nnano.2006.172.

[123] Liu Y, Chen S, Zussman E, Korach CS, Zhao W, Rafailovich M. Diameter-Dependent Modulus and Melting Behavior in Electrospun Semicrystalline Polymer Fibers. Macromolecules 2011;44:4439–44. doi:10.1021/ma200262z.

[124] Zhang X, Nakagawa R, Ho K, Chan K, Kotaki M. Mechanical Property Enhancement of Polylactide Nano fi bers through Optimization of Molecular Weight , Electrospinning Conditions , and Stereocomplexation 2012.

[125] Camposeo A, Greenfeld I, Tantussi F, Pagliara S, Mo M, Fuso F, et al. Local Mechanical Properties of Electrospun Fibers Correlate to Their Internal Nanostructure 2013.

[126] Noy A, Frisbie CD, Rozsnyai LF, Wrighton MS, Lieber CM. Chemical Force Microscopy: Exploiting Chemically-Modified Tips To Quantify Adhesion, Friction, and Functional Group Distributions in Molecular Assemblies. J Am Chem Soc 1995;117:7943–51. doi:10.1021/ja00135a012.

[127] Liu Y, Wu T, Evans DF. Lateral Force Microscopy Study on the Shear Properties of Self-Assembled Monolayers of Dialkylammonium Surfactant on Mica. Langmuir 1994;10:2241–5. doi:10.1021/la00019a035.

[128] Neumeister JM, Ducker W a. Lateral, normal, and longitudinal spring constants of atomic force microscopy cantilevers. Rev Sci Instrum 1994;65:2527. doi:10.1063/1.1144646.

[129] Cuenot S, Frétigny C, Demoustier-Champagne S, Nysten B. Surface tension effect on the mechanical properties of nanomaterials measured by atomic force microscopy. Phys Rev B 2004;69:165410. doi:10.1103/PhysRevB.69.165410.

[130] Schubach HR, Nagy E, Heise B. Short range order of amorphous polymers derived by WAXS. Colloid Polym Sci 1981;259:789–96. doi:10.1007/BF01388082.

[131] Wecker SM, Davidson T, Cohen JB. A structural study of glassy polystyrene. J Mater Sci 1972;7:1249–59. doi:10.1007/BF00550690.

[132] Kongkhlang T, Tashiro K, Kotaki M, Chirachanchai S. Electrospinning as a new technique to control the crystal morphology and molecular orientation of polyoxymethylene nanofibers. J Am Chem Soc 2008;130:15460–6. doi:10.1021/ja804185s.

[133] Kakade M V, Givens S, Gardner K, Lee KH, Chase DB, Rabolt JF. Electric field induced orientation of polymer chains in macroscopically aligned electrospun polymer nanofibers. J Am Chem Soc 2007;129:2777–82. doi:10.1021/ja065043f.

[134] Gu S-Y, Wu Q-L, Ren J, Vancso GJ. Mechanical Properties of a Single Electrospun Fiber and Its Structures. Macromol Rapid Commun 2005;26:716–20. doi:10.1002/marc.200400667.

[135] Lee K-H, Kim K-W, Pesapane A, Kim H-Y, Rabolt JF. Polarized FT-IR Study of Macroscopically Oriented Electrospun Nylon-6 Nanofibers. Macromolecules 2008;41:1494–8. doi:10.1021/ma701927w.

[136] Arruda EM, Boyce MC. Evolution of plastic anisotropy in amorphous polymers during finite straining. Int J Plast 1993;9:697–720. doi:10.1016/0749-6419(93)90034-N.

[137] Northolt MG, van Aartsen JJ. Chain orientation distribution and elastic properties of poly (p-phenylene terephthalamide), a "rigid rod" polymer. J Polym Sci Polym Symp 2007;58:283–96. doi:10.1002/polc.5070580120.

[138] Wu B, Heidelberg A, Boland JJ. Mechanical properties of ultrahigh-strength gold nanowires. Nat Mater 2005;4:525–9. doi:10.1038/nmat1403.

[139] Gall K, Diao J, Dunn ML. The Strength of Gold Nanowires 2004.

[140] Liu L-Q, Eder M, Burgert I, Tasis D, Prato M, Daniel Wagner H. One-step electrospun nanofiber-based composite ropes. Appl Phys Lett 2007;90:083108. doi:10.1063/1.2644379.

[141] Arshad SN, Naraghi M, Chasiotis I. Strong carbon nanofibers from electrospun polyacrylonitrile. Carbon N Y 2011;49:1710–9. doi:10.1016/j.carbon.2010.12.056.

[142] Naito K, Tanaka Y, Yang J-M, Kagawa Y. Tensile properties of ultrahigh strength PAN-based, ultrahigh modulus pitch-based and high ductility pitch-based carbon fibers. Carbon N Y 2008;46:189–95. doi:10.1016/j.carbon.2007.11.001.

[143] Ning Pan. A Modified Analysis of the Microstructural Characteristics of General Fiber Assemblies. Text Res J 1993;63:336–45. doi:10.1177/004051759306300605.

[144] Pan N. Prediction of statistical strengths of twisted fibre structures. J Mater Sci 1993;28:6107–14. doi:10.1007/BF00365030.

[145] Wang N, Ostuni E, Whitesides GM, Ingber DE. Micropatterning tractional forces in living cells. Cell Motil Cytoskeleton 2002;52:97–106. doi:10.1002/cm.10037.

[146] Wang P-Y, Yu H-T, Tsai W-B. Modulation of alignment and differentiation of skeletal myoblasts by submicron ridges/grooves surface structure. Biotechnol Bioeng 2010;106:285–94. doi:10.1002/bit.22697.

[147] Stevens MM, George JH. Exploring and engineering the cell surface interface. Science 2005;310:1135–8. doi:10.1126/science.1106587.

[148] Chen CS. Geometric Control of Cell Life and Death. Science (80-) 1997;276:1425–8. doi:10.1126/science.276.5317.1425.

[149] Chen CS, Mrksich M, Huang S, Whitesides GM, Ingber DE. Micropatterned surfaces for control of cell shape, position, and function. Biotechnol Prog n.d.;14:356–63. doi:10.1021/bp980031m.

[150] Ji Y, Ghosh K, Zheng X, Li B, Sokolov JC, Prestwich GD, et al. Electrospun three-dimensional hyaluronic acid nanofibrous scaffolds. Biomaterials 2006;27:3782–92. doi:10.1016/j.biomaterials.2006.02.037.

[151] Pham QP, Sharma U, Mikos AG. Electrospun poly(epsilon-caprolactone) microfiber and multilayer nanofiber/microfiber scaffolds: characterization of scaffolds and measurement of cellular infiltration. Biomacromolecules 2006;7:2796–805. doi:10.1021/bm060680j.

[152] Erisken C, Zhang X, Moffat KL, Levine WN, Lu HH. Scaffold Fiber Diameter Regulates Human Tendon Fibroblast Growth and Differentiation. Tissue Eng Part A 2012;19. doi:10.1089/ten.tea.2012.0072.

[153] Ker EDF, Nain AS, Weiss LE, Wang J, Suhan J, Amon CH, et al. Bioprinting of growth factors onto aligned sub-micron fibrous scaffolds for simultaneous control of cell differentiation and alignment. Biomaterials 2011;32:8097–107.

[154] Matsuda N, Shimizu T, Yamato M, Okano T. Tissue Engineering Based on Cell Sheet Technology. Adv Mater 2007;19:3089–99. doi:10.1002/adma.200701978.

[155] Wang P-Y, Thissen H, Tsai W-B. The roles of RGD and grooved topography in the adhesion, morphology, and differentiation of C2C12 skeletal myoblasts. Biotechnol Bioeng 2012;109:2104–15. doi:10.1002/bit.24452.

[156] Engler AJ, Sen S, Sweeney HL, Discher DE. Matrix elasticity directs stem cell lineage specification. Cell 2006;126:677–89. doi:10.1016/j.cell.2006.06.044.

[157] Salim A, Giaccia AJ, Longaker MT. Stem cell differentiation. Nat Biotechnol 2004;22:804–5; author reply 805–6. doi:10.1038/nbt0704-804.

[158] Huelsken J, Vogel R, Erdmann B, Cotsarelis G, Birchmeier W. β-Catenin Controls Hair Follicle Morphogenesis and Stem Cell Differentiation in the Skin. Cell 2001;105:533–45. doi:10.1016/S0092-8674(01)00336-1.

[159] Thomson JA. Embryonic Stem Cell Lines Derived from Human Blastocysts. Science (80-) 1998;282:1145–7. doi:10.1126/science.282.5391.1145.

[160] Xu R-H, Chen X, Li DS, Li R, Addicks GC, Glennon C, et al. BMP4 initiates human embryonic stem cell differentiation to trophoblast. Nat Biotechnol 2002;20:1261–4. doi:10.1038/nbt761.

[161] Benoit DSW, Schwartz MP, Durney AR, Anseth KS. Small functional groups for controlled differentiation of hydrogel-encapsulated human mesenchymal stem cells. Nat Mater 2008;7:816–23. doi:10.1038/nmat2269.

[162] De Coppi P, Bartsch G, Siddiqui MM, Xu T, Santos CC, Perin L, et al. Isolation of amniotic stem cell lines with potential for therapy. Nat Biotechnol 2007;25:100–6. doi:10.1038/nbt1274.

[163] Jiang Y, Jahagirdar BN, Reinhardt RL, Schwartz RE, Keene CD, Ortiz-Gonzalez XR, et al. Pluripotency of mesenchymal stem cells derived from adult marrow. Nature 2002;418:41–9. doi:10.1038/nature00870.

[164] Pittenger MF. Multilineage Potential of Adult Human Mesenchymal Stem Cells. Science (80-) 1999;284:143–7. doi:10.1126/science.284.5411.143.

[165] Chowdhury F, Na S, Li D, Poh Y-C, Tanaka TS, Wang F, et al. Material properties of the cell dictate stress-induced spreading and differentiation in embryonic stem cells. Nat Mater 2010;9:82–8. doi:10.1038/nmat2563.

[166] Even-Ram S, Artym V, Yamada KM. Matrix control of stem cell fate. Cell 2006;126:645–7. doi:10.1016/j.cell.2006.08.008.

[167] Kilian KA, Bugarija B, Lahn BT, Mrksich M. Geometric cues for directing the differentiation of mesenchymal stem cells. Proc Natl Acad Sci U S A 2010;107:4872–7. doi:10.1073/pnas.0903269107.

[168] Engler AJ, Sen S, Sweeney HL, Discher DE. Matrix elasticity directs stem cell lineage specification. Cell 2006;126:677–89. doi:10.1016/j.cell.2006.06.044.

[169] Maruthamuthu V, Sabass B, Schwarz US, Gardel ML. Cell-ECM traction force modulates endogenous tension at cell-cell contacts. Proc Natl Acad Sci U S A 2011;108:4708–13. doi:10.1073/pnas.1011123108.

[170] Merkel R, Kirchgessner N, Cesa CM, Hoffmann B. Cell force microscopy on elastic layers of finite thickness. Biophys J 2007;93:3314–23. doi:10.1529/biophysj.107.111328.

[171] Mijailovich SM, Fredberg JJ, Butler JP. On the theory of muscle contraction: filament extensibility and the development of isometric force and stiffness. Biophys J 1996;71:1475–84. doi:10.1016/S0006-3495(96)79348-7.

[172] Trepat X, Wasserman MR, Angelini TE, Millet E, Weitz DA, Butler JP, et al. Physical forces during collective cell migration. Nat Phys 2009;5:426–30. doi:10.1038/nphys1269.

[173] Almqvist N, Bhatia R, Primbs G, Desai N, Banerjee S, Lal R. Elasticity and adhesion force mapping reveals real-time clustering of growth factor receptors and associated

changes in local cellular rheological properties. Biophys J 2004;86:1753–62. doi:10.1016/S0006-3495(04)74243-5.

[174] Cesa CM, Kirchgessner N, Mayer D, Schwarz US, Hoffmann B, Merkel R. Micropatterned silicone elastomer substrates for high resolution analysis of cellular force patterns. Rev Sci Instrum 2007;78:034301. doi:10.1063/1.2712870.

[175] Reinhart-King CA, Dembo M, Hammer DA. Endothelial Cell Traction Forces on RGD-Derivatized Polyacrylamide Substrata †. Langmuir 2003;19:1573–9. doi:10.1021/la026142j.

[176] Shreiber DI, Barocas VH, Tranquillo RT. Temporal variations in cell migration and traction during fibroblast-mediated gel compaction. Biophys J 2003;84:4102–14. doi:10.1016/S0006-3495(03)75135-2.

[177] Velegol D, Lanni F. Cell traction forces on soft biomaterials. I. Microrheology of type I collagen gels. Biophys J 2001;81:1786–92. doi:10.1016/S0006-3495(01)75829-8.

[178] Franck C, Maskarinec SA, Tirrell DA, Ravichandran G. Three-dimensional traction force microscopy: a new tool for quantifying cell-matrix interactions. PLoS One 2011;6:e17833. doi:10.1371/journal.pone.0017833.

[179] Maskarinec SA, Franck C, Tirrell DA, Ravichandran G. Quantifying cellular traction forces in three dimensions. Proc Natl Acad Sci U S A 2009;106:22108–13. doi:10.1073/pnas.0904565106.

[180] Chandra D, Yang S. Capillary-force-induced clustering of micropillar arrays: is it caused by isolated capillary bridges or by the lateral capillary meniscus interaction force? Langmuir 2009;25:10430–4. doi:10.1021/la901722g.

[181] Schoen I, Hu W, Klotzsch E, Vogel V. Probing cellular traction forces by micropillar arrays: contribution of substrate warping to pillar deflection. Nano Lett 2010;10:1823–30. doi:10.1021/nl100533c.

[182] Du Roure O, Saez A, Buguin A, Austin RH, Chavrier P, Silberzan P, et al. Force mapping in epithelial cell migration. Proc Natl Acad Sci U S A 2005;102:2390–5. doi:10.1073/pnas.0408482102.

[183] Timoshenko S. Strength of Materials, Pt. 2: Advanced Theory and Problems, Part 2. vol. 2. R. E. Krieger Publishing Company; 1983.

[184] Ghibaudo M, Saez A, Trichet L, Xayaphoummine A, Browaeys J, Silberzan P, et al. Traction forces and rigidity sensing regulate cell functions. Soft Matter 2008;4:1836. doi:10.1039/b804103b.

[185] Discher DE, Janmey P, Wang YL. Tissue cells feel and respond to the stiffness of their substrate. Science (80-) 2005;310:1139–43. doi:10.1126/science.1116995.

[186] Dembo M, Wang YL. Stresses at the cell-to-substrate interface during locomotion of fibroblasts. Biophys J 1999;76:2307–16. doi:10.1016/S0006-3495(99)77386-8.

[187] Wang H, Dembo M, Wang Y. Substrate flexibility regulates growth and apoptosis of normal but not transformed cells 2000;01605:1345–50.

[188] Zhang Y-H, Zhao C-Q, Jiang L-S, Dai L-Y. Substrate stiffness regulates apoptosis and the mRNA expression of extracellular matrix regulatory genes in the rat annular cells. Matrix Biol 2011;30:135–44. doi:10.1016/j.matbio.2010.10.008.

[189] Winer JP, Sc B, Janmey PA, Ph D, Mccormick ME, Funaki M. Bone Marrow-Derived Human Mesenchymal Stem Cells Become Quiescent on Soft Substrates but Remain Responsive to Chemical or Mechanical Stimuli 2009;15.

[190] Ulrich T a, de Juan Pardo EM, Kumar S, Pardo EM de J. The mechanical rigidity of the extracellular matrix regulates the structure, motility, and proliferation of glioma cells. Cancer Res 2009;69:4167–74. doi:10.1158/0008-5472.CAN-08-4859.

[191] Klein E a, Yin L, Kothapalli D, Castagnino P, Byfield FJ, Xu T, et al. Cell-cycle control by physiological matrix elasticity and in vivo tissue stiffening. Curr Biol 2009;19:1511–8. doi:10.1016/j.cub.2009.07.069.

[192] Stewart MP, Helenius J, Toyoda Y, Ramanathan SP, Muller DJ, Hyman AA. Hydrostatic pressure and the actomyosin cortex drive mitotic cell rounding. Nature 2011;469:226–30. doi:10.1038/nature09642.

[193] Salbreux G, Joanny JF, Prost J, Pullarkat P. Shape oscillations of non-adhering fibroblast cells. Phys Biol 2007;4:268–84. doi:10.1088/1478-3975/4/4/004.

[194] Borau C, Kim T, Bidone T, García-Aznar JM, Kamm RD. Dynamic mechanisms of cell rigidity sensing: insights from a computational model of actomyosin networks. PLoS One 2012;7:e49174. doi:10.1371/journal.pone.0049174.

[195] Wang R, Hashimoto K, Fujishima A, Chikuni M, Kojima E, Kitamura A, et al. Photogeneration of Highly Amphiphilic TiO2 Surfaces. Adv Mater 1998;10:135–8. doi:10.1002/(SICI)1521-4095(199801)10:2<135::AID-ADMA135>3.0.CO;2-M.

[196] Wang R, Hashimoto K, Fujishima A, Chikuni M, Kojima E, Kitamura A, et al. Light-induced amphiphilic surfaces 1997;388:431–2.

[197] Linsebigler AL, Lu G, Yates JT. Photocatalysis on TiO2 Surfaces: Principles, Mechanisms, and Selected Results. Chem Rev 1995;95:735–58. doi:10.1021/cr00035a013.

[198] Richter S, Steinhart M, Hofmeister H, Zacharias M, Gösele U, Gaponik N, et al. Quantum dot emitters in two-dimensional photonic crystals of macroporous silicon. Appl Phys Lett 2005;87:142107. doi:10.1063/1.2081123.

[199] Macak JM, Tsuchiya H, Ghicov A, Yasuda K, Hahn R, Bauer S, et al. TiO2 nanotubes: Self-organized electrochemical formation, properties and applications. Curr Opin Solid State Mater Sci 2007;11:3–18. doi:10.1016/j.cossms.2007.08.004.

[200] Albu SP, Ghicov A, Aldabergenova S, Drechsel P, LeClere D, Thompson GE, et al. Formation of Double-Walled TiO 2 Nanotubes and Robust Anatase Membranes. Adv Mater 2008:NA – NA. doi:10.1002/adma.200801189.

[201] Gong D, Grimes CA, Varghese OK, Hu W, Singh RS, Chen Z, et al. Titanium oxide nanotube arrays prepared by anodic oxidation. J Mater Res 2011;16:3331–4. doi:10.1557/JMR.2001.0457.

[202] Macak JM, Sirotna K, Schmuki P. Self-organized porous titanium oxide prepared in Na2SO4/NaF electrolytes. Electrochim Acta 2005;50:3679–84. doi:10.1016/j.electacta.2005.01.014.

[203] Li D, Xia Y. Fabrication of Titania Nanofibers by Electrospinning. Nano Lett 2003;3:555–60. doi:10.1021/nl034039o.

[204] Zhan S, Chen D, Jiao X, Tao C. Long TiO2 hollow fibers with mesoporous walls: sol-gel combined electrospun fabrication and photocatalytic properties. J Phys Chem B 2006;110:11199–204. doi:10.1021/jp057372k.

[205] Huang Y-C, Chang S-Y, Lin C-F, Tseng WJ. Synthesis of ZnO nanorod grafted TiO2 nanotube 3-D arrayed heterostructure as supporting platform for nanoparticle deposition. J Mater Chem 2011;21:14056. doi:10.1039/c1jm11659b.

[206] Mohapatra SK, Kondamudi N, Banerjee S, Misra M. Functionalization of self-organized TiO2 nanotubes with Pd nanoparticles for photocatalytic decomposition of dyes under solar light illumination. Langmuir 2008;24:11276–81. doi:10.1021/la801253f.

[207] Acosta-Silva YJ, Nava R, Hernández-Morales V, Macías-Sánchez SA, Gómez-Herrera ML, Pawelec B. Methylene blue photodegradation over titania-decorated SBA-15. Appl Catal B Environ 2011;110:108–17. doi:10.1016/j.apcatb.2011.08.032.

[208] Yu S, Li B, Luo Y, Dong L, Fan M, Zhang F. Preparation of Ag-Modified (B,P)-Codoped TiO 2 Hollow Spheres with Enhanced Photocatalytic Activity. Eur J Inorg Chem 2014;2014:1142–9. doi:10.1002/ejic.201301388.

[209] Kojic N, Kojic M, Gudlavalleti S, McKinley G. Solvent removal during synthetic and Nephila fiber spinning. Biomacromolecules 2004;5:1698–707. doi:10.1021/bm034280x.

[210] Farhangi N, Chowdhury RR, Medina-Gonzalez Y, Ray MB, Charpentier PA. Visible light active Fe doped TiO2 nanowires grown on graphene using supercritical CO2. Appl Catal B Environ 2011;110:25–32. doi:10.1016/j.apcatb.2011.08.012.

[211] Height MJ, Pratsinis SE, Mekasuwandumrong O, Praserthdam P. Ag-ZnO catalysts for UV-photodegradation of methylene blue. Appl Catal B Environ 2006;63:305–12. doi:10.1016/j.apcatb.2005.10.018.

[212] Lachheb H, Puzenat E, Houas A, Ksibi M, Elaloui E, Guillard C, et al. Photocatalytic degradation of various types of dyes (Alizarin S, Crocein Orange G, Methyl Red, Congo Red, Methylene Blue) in water by UV-irradiated titania. Appl Catal B Environ 2002;39:75–90. doi:10.1016/S0926-3373(02)00078-4.